UNIVERSITY OF GENOVA

PHD PROGRAM IN BIOENGINEERING AND ROBOTICS

Exploring innovative stimulation protocols to promote neuromodulation in brain-on-a-chip models

by

Marietta Pisano

Thesis submitted for the degree of *Doctor of Philosophy in Bioengineering and Robotics*
33° cycle

Supervisor: Prof. Raiteri R.
Co-Supervisor: Prof. Massobrio P.
The head of the PhD program: Prof. Cannata G.

Dibris

Department of Informatics, Bioengineering, Robotics and Systems Engineering

W*hat I learned from this PhD journey was falling, falling so many times that I wondered why I was even walking. Every time I got up, one idea became simpler and clearer: life is full of disappointments, failures, and losses, but none of those things can permanently stop you. You have the power to overcome everything life throws at you. Nothing is more powerful than a determined mind. Surround yourself with people that will remind you of your worth and who help you in the ways that are most important to you. Nobody, no condition, and no scenario have to determine who you are. Don't give up, break, or lose faith in what's possible. It is not over until you have won.*

- To the smile of my mother
Since my achievements are solely due to your efforts

Declaration

I hereby declare that except where specific reference is made to the work of others, the contents of this dissertation are original and have not been submitted in whole or in part for consideration for any other degree or qualification in this, or any other university. This dissertation is my own work and contains nothing which is the outcome of work done in collaboration with others, except as specified in the text and Acknowledgements. This dissertation contains fewer than 35,338 words including appendices, bibliography, footnotes, tables and equations and has fewer than 35 figures.

April 2021

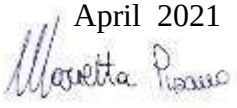

Acknowledgements

This thesis is the result of a long journey that began when I was still a graduate student at this university. It was a journey filled with stormy days, but it was also a journey filled with great surprises and joyous days.

I would like to thank Roberto Raiteri for choosing me; without him, I would not have been able to board the 33rd cycle doctoral train.

Thanks to Professor Paolo Massobrio, in addition to helping and leading me on this journey, taught me to see the light even in the darkest of nights, and most importantly, he continued to believe in me when I first stopped doing it. Thank you, because without your help today, I would not be here.

Thank you, Mariateresa Tedesco, for always being there, not only for working but also for all of your advice and time.

Thank you to Michael Pusch and Paola Gavazzo of the CNR of Genoa for providing me with the ability to expand my experience and for supporting me in all of my experiments.

Finally, thanks to the Dibris PhD students and professors who have been my second family in recent years, and who, like a family, have shown me the best and worst of this journey.

Contents

List of figures

microcapsules. ***(c)*** The EDTA addition dissolved the core (CaCo3) of the microcapsules, obtaining hollow microcapsules.

Figure 2.1: Sketch material and methods. Cortical cells from cortical rat embryos ***(a)*** were plated into 60-channels MEA ***(b)***. The piezoelectric transducer is placed inside the MEA and guided by a home-made set up ***(c)***. The ultrasound were emitted as a pulsed wave ***(d)***. Description of the experimental protocol performed at 20 and 21 days in vitro ***(e)***.

Figure 2.2: ***(a)*** Calculated sound pressure field as a function of US driving signal (DS). ***(b)*** Temperature increase of the solution in function of DS. (Blue line indicates the initial temperature of the solution T_0)

Figure 2.3: ***(a)*** Neuronal network image of mature cortical culture (21DIV) without (W/O BTNPs, top) and with (BTNPs, bottom) BTNPs: the fluorescent image (green: MAP2, red: NeuN) is superimposed on the DIC image of the same area (dark dust: BTNPs, dark circle: MEA electrode. ***(b)*** Representative raster plots of the spontaneous activity of a neuronal network before (W/O BTNPs) and after (BTNPs) the piezonanoparticles addition. Spiking and bursting activity characterization of culture before (W/O BTNPs) and after (BTNPs) the piezonanoparticles delivery: ***(c)*** mean firing rate (MFR); ***(d)*** mean burst rate (MBR); ***(e)*** inter bursts interval (IBI); ***(f)*** bursts duration (BD)

Figure 2.4: ***(a)*** Spiking and ***(b-d)*** bursting activity of cortical cultures with BTNPs as a function of ultrasound DS amplitude.

Figure 2.5: ***a)*** Percentage of active channels (%Ch) as a function of different DS during the three protocol phases: pre-stimulus (Pre-Stim, black dots), stimulus (Stim, green dots) and post stimulus (Post-Stim, gray dots*).* ***(b)*** The trends of the probability of the active channels of a representative experiment in the 45 stimuli for the on (green line) and off period (red line) for the US stimulation amplitude of: 20V, 40V, 50V, 60V and 70V***;*** ***(c)*** probability that the electrodes are active during on and off stimulation phases divided into three stimuli groups (1-15, 16-30 and 31-45).

Figure 2.6: Representative Post stimulus time histogram (PSTH) of the probability of channels activation after the delivery of: ***(a)*** US stimulation and ***(b)*** electrical stimulation (bin 5ms). Cumulative PSTH after the delivery of: ***(c)*** US stimulation and ***(d)*** electrical stimulation (bin 5ms) ***(e)*** PSTH area of the US and electrical stimulation.

Figure 2.7: ***(a)*** Spiking and ***(b)*** bursting activity of cortical cultures with BTNPs as a function of ultrasound DS amplitude.

Figure 3.1: Optical images of HEK 293 cells plated on different substrates: glass (left), 4

kPa PMMA hydrogel (middle) and 40 kPa PMMA hydrogel (right).

Figure 3.2: Sequence of successive calcium images for a representative experiment showing the increase in intensity emitted by the calcium dye after US stimulation. The red mark indicates when the US stimulation is started; time interval between images: 0.33 s.

Figure 3.3 Results of calcium imaging of control experiments: (a) Photobleaching pattern of transfected HEK cells in absence of US stimulus. (b) HEK 293 non transfected and subjected to US stimulation (red rectangle) at different intensities: 0.21 W / cm^2, 2.56W / cm^2 and 6.78 W / cm^2. (c) HEK 293 transfected to express CD8 protein US stimulated (red rectangle) at different intensities and plated on different substrates: glass (blue), 4 kPa hydrogel (red) and 40 kPa hydrogel (green)

Figure 3.4: ***(a)*** Time difference (ΔT) between the start of US stimulation and the inflection of the fluorescence intensity of the cells (related to the calcium transients) as a function of US intensities. Measured on n = 5 cells. ***(b)*** Fluorescence intensity trends of a representative cell for each US intensities. The red square indicates the US stimulation, while the blue line indicates the inflection point.

Figure 3.5: (***a)*** Time difference (ΔT) between the start of US stimulation and the inflection of the fluorescence intensity of the cells (related to the calcium transients) as a function of US intensities. Measured on n = 5 cells. ***(b)*** Fluorescence intensity trends of a representative cell for each US intensities. The red square indicates the US stimulation, while the blue line indicates the inflection point.

Figure 3.6: ***(a)*** Time difference (ΔT) between the start of US stimulation and the inflection of the fluorescence intensity of the cells (related to the calcium transients) as a function of US intensities. Measured on n = 5 cells. ***(b)*** Fluorescence intensity trends of a representative cell for each US intensity. The red square indicates the US stimulation, while the blue line indicates the inflection point.

Figure 3.7: Percentage of the activated cells on the different substrate: glass (blue squares), 40 kPa hydrogel (red squares) and 4 kPa hydrogel (green squares). The percentage was calculated on about n= 200 cells for each experimental configuration. US intensities were reported on a logarithmic scale.

Figure 4.1: ***(a)*** Ultrasound stimulation induces capsules breakage promoting the release of the encapsulated drug. ***(b)*** Phase contrast microscopy image of polyelectrolyte microcapsules in solution/adsorbed on glass. ***(c)*** Fluorescence image of polyelectrolyte microcapsules stained with FITC-dextran ***(d-e)*** confocal image: polyelectrolyte microcapsules with a FITC-dextran layer (green) and filled with DOX (red).

Figure 4.2: ***(a)*** Measured mechanical index (MI) as a function of the source power density. **(b)** Temperature increase of the solution over time by the US stimulation at 1.5W/cm^2 power density

Figure 4.3: ***(a)*** confocal images of empty PCs after US exposure; (b) graphical representation of the significative difference between the areas of not sonicated (No US) and sonicated empty PCs (US) ($p = 0.01$); (c) confocal images of FluoSpheres™ filled microcapsules after US exposure; (d) DOX concentrations of control and sonicated samples to calculate the DOX released by the PCs with and without the US stimulation

Figure 4.4: Results from cell viability MTT assays after 24h from plating ***(a)*** Boxplot of MCF7 cell viability without any treatment (control), incubated with empty capsules (EC), with exposed to US empty capsules (EC+US) and exposed to US Dox-filled capsules (DC). ***(b)*** Phase contrast microscopy images of the samples tested for cell viability; scale bar: 100 μm.

Figure 4.5: ***(a)*** Confocal images of PCs before and after US exposure (red, DOX and green, layer) ***(b)*** Percentage of broken DOX-loaded PCs as a function of US intensity. Values are calculated over three different samples, considering for each sample 70 PCs.

Figure 4.6: Results from cell viability MTT assays after 24h from plating ***(a)*** Box-plot of MCF7 cell viability without any treatment (control), incubated with empty capsules (EC), and exposed to US protocol at max intensity (US HG). ***(b)*** MCF7 cell viability after 24h in culture dishes without any treatment (control), incubated with capsules loaded with Doxorubicin (DC), and exposed to US at 0.25w/cm2 intensity (DC + LW US) and 1W/cm2 intensity (DC + HG US). ***(c)*** MCF7 cell viability after 24h in culture dishes without any treatment (control), incubated with 2.5 μg or 5.6 μg of free Dox , and exposed to US at 0.25w/cm2 or 1W/cm2 intensity (DOX + LW US and DOX + HG US, respectively). ***(d)*** Phase contrast microscopy images of the samples tested for cell viability; scale bar: 50 μm.

Figure 5.1: Neuronal network images. ***(A)*** Mature 2D culture (21 DIV) on a planar substrate (green: MAP2 and blue: NeuN). ***(B)*** 2D interconnected cortical-hippocampal culture at 21 DIV stained in order to visualize neuronal nuclear protein (NeuN, red) and GABA neurotransmitter (green: Anti-GABA); where the two markers overlap the cellular soma looks yellow-orange. ***(C)*** Mature 3D culture (21 DIV) on glass microbeads (green: MAP2). ***(D)*** 3D interconnected cortical-hippocampal culture at 21 DIV on MEA. In the middle: the neurites across the microchannels. On the sides: neurons coupled to the glass microbeads. ***(E)*** Different layers of 3D heterogeneous culture: each stack is relative to one layer.

Figure 5.2: Spiking and bursting activity characterization of 2D homogeneous cortical (Cx-Cx2D , red) and hippocampal (Hp-Hp2D, blue) cultures. ***(A)*** mean firing rate (MFR), p =

0.6; ***(B)*** mean bursting rate (MBR), p = 0.009; ***(C)*** burst duration (BD); ***(D)*** inter burst intervals (IBI), p = 0.3; ***(E)*** percentage random spikes (%RandomSpikes), p = 0.009; ***(F)*** spikes per burst (SpikesXBurst), p = 0.009;

Figure 5.3: Spiking and bursting activity characterization of 3D homogeneous cortical (Cx-Cx_{3D} , red) and hippocampal (Hp-Hp_{3D} , blue) cultures. ***(A)*** mean firing rate (MFR), p = 0.9; ***(B)*** mean bursting rate (MBR), p = 0.01; ***(C)*** burst duration (BD), p=0.009; ***(D)*** inter burst intervals (IBI), p = 0.07; ***(E)*** percentage random spikes (%RandomSpikes), p = 0.009; ***(F)*** spikes per burst (SpikesXBurst), p = 0.009;

Figure 5.4: Comparison of the spiking and bursting features of the different experimental configurations: 2D homogeneous cortical (Cx-Cx_{2D} , red), 2D heterogeneous (Cx-Hp_{2D} black), and 3D cortical (Cx-Cx_{3D} , green) cultures. ***(A)*** Mean Firing Rate (Cx-Cx_{2D} vs. Cx-Hp_{2D} : p = 0.009; Cx-Cx_{2D} vs. Cx-Cx_{3D} : p = 0.04). ***(B)*** Mean Bursting Rate (Cx-Cx_{2D} vs. Cx-Hp_{2D} : p = 0.01). ***(C)*** Percentage of random spikes (Cx-Cx_{2D} vs. Cx-Cx_{3D} : p = 0.02). ***(D)*** Spikes per burst (Cx-Cx_{2D} vs. Cx-Cx_{3D} : p = 0.009). ***(E)*** Burst Duration (Cx-Cx_{2D} vs. Cx-Cx_{3D} : p = 0.04). (F) Inter Burst Intervals (Cx-Cx_{2D} vs. Cx-Hp_{2D} : p = 0.009).

Figure 5.5: Spontaneous electrophysiological activity of 3D heterogeneous cultures (Cx-Hp_{3D}) compared with 3D homogeneous cultures (Cx-Cx_{3D}) and 2D heterogeneous cultures (Cx-Hp_{2D}). ***(A)*** Radar plot showing the variations of the mean firing rate (MFR), mean bursting rate (MBR), burst duration (BD), inter burst interval (IBI), spikes per burst, and percentage random spikes induced by the different experimental configurations. Red line indicates no variations, gray shadow indicates the comparison heterogeneous 2D and 3D cultures, purple shadow indicates the comparison between 3D homogeneous and heterogeneous culture. Spontaneous activity and the relative trace of the instantaneous firing rate of a representative (10 s): ***(B)*** 3D heterogeneous culture (Cx-Hp_{3D}, cortical-red and hippocampal-green). ***(C)*** 2D heterogeneous culture (Cx-Hp_{2D}). ***(D)*** 3D cortical culture (Cx-Cx_{3D}).

Figure 5.6: Network bursting activity characterization of 2D homogeneous cortical (Cx-Cx_{2D} , red), 2D heterogeneous (Cx-Hp_{2D} black), 3D homogeneous cortical (Cx-Cx_{3D} , green) and 3D heterogeneous (Cx-Hp_{3D}, purple) cultures. ***(A)*** Mean network bursting rate (MNBR, Cx-Cx_{2D} vs. Cx-Hp_{2D} : p = 0.01; Cx-Cx_{3D} vs. Cx-Hp_{3D} : p = 0.03). ***(B)*** Network burst duration (NBD, Cx-Cx_{2D} vs. Cx-Hp_{2D} : p = 0.01; Cx-Cx_{3D} vs. Cx-Hp_{3D} : p = 0.02). ***(C)*** Propagation maps of one network burst in the different experimental configuration. The big black dot represents the initiation site of the considered network burst. The color-coded shows the propagation delays of the event. ***(D)*** Percentage of the network burst origin evaluated over all the detected network. bursts.

Figure 5.7: Network bursting activity dynamics of 3D heterogeneous (Cx-Hp_{3D} , purple—square) compared with 2D heterogeneous (Cx-Hp_{2D} black—diamond) and 3D homogeneous cortical (Cx-Cx_{3D} , green—dots) cultures. ***(A)*** Average Spike Times Histogram (STH). Inset: NBs normalized distances between Cx-Hp_{3D} (reference) and Cx-Hp_{2D} (black diamond) and Cx-Cx_{3D} (green dot). ***(B)*** STH rise phase of three representative experiments (one per each configuration) and relative fitting (solid line), left. The inset shows the exponents of the best-fit rising phase (five values per each dataset). Right, time constants of the rise phase (Cx-Hp_{3D} vs. Cx-Cx_{3D} , $p = 0.67$, Cx-Hp_{3D} vs. Cx-Hp_{2D} , $p = 1$). ***(C)*** STH decay phase of three representative experiments (one per each configuration) and relative fitting (solid line), left. The inset shows the exponent of the best-fit decaying phase (five values per each dataset). Right, time constant of decay dynamics (Cx-Hp_{3D} vs. Cx-Cx_{3D} , $p = 0.008$, Cx-Hp_{3D} vs. Cx-Hp_{2D} , $p = 0.05$).

Introduction

Nowadays, many neurological diseases affect millions of people (*World Health Organization*). These diseases are extremely difficult to cure, and very often they induce debilitating outcomes. Among the causes that make difficult to find valid treatments to increase the quality of the life of people affected by brain impairments, the principal is due to the extreme complexity of the brain at every scale of investigation (i.e., from single transmembrane channel up to the synaptically-mediated interactions among neurons). The brain is made up of about 100 billions cells (Herculano-Houzel, 2012) on which we depend for proper functioning every second of every day. Neurons are connected with one another so that we can speak, think, move, learn, and do everything else. Because of the complexity of the brain, neurological disorders may occur from very minor miscommunications among cells (Bassett & Bullmore, 2009). Scientists are still working to understand brain impairments and to elucidate how the brain develops strategies to either arrest gradual degradation or to repair damage in neuronal circuits. Due to its structural complexity, studying the brain represents a big challenge that has evolved towards a truly multidisciplinary endeavor in the last decades (Bullmore & Sporns, 2009).
One of the basic, yet informative, approaches to study the brain makes use of *in vitro* cell cultures. This bottom-up approach allows to simplify the complexity of the system (brain) and advance with intermediate solutions before the final problem is solved. This simplified experimental model is crucial when attempting to identify treatments for disorders that affect complex organs such as the brain, where the first step is to try to explain the dynamics behind such a complexity.

In the case of neuronal systems, *in vitro* neuronal networks (dissociated cultures and slices) are a well-accepted experimental model to explore different electrophysiological properties of *in vivo* systems. When such networks are coupled to Micro-Electrodes Arrays (MEAs), the global behavior emerging from the interactions of neurons synaptically connected can be explored and statistically characterized (Taketani and Baudry, 2006). By exploiting the technological features of MEAs, it has been possible to investigate the neuronal dynamics of different cerebral mammalian areas such as cortex (Pasquale et al., 2008) and hippocampus (Brewer et al., 2009), study their development (Napoli et al., 2014; Wagenaar et al., 2006), modulate their response by delivering electrical (Poli & Massobrio, 2018; Wagenaar et al., 2005) or chemical stimulation (Gross et al., 1992, 1995), induce synaptic plasticity (Chiappalone et al., 2008), and understand their topological properties as well as the interplay with emergent dynamics (Massobrio et al., 2015; Poli et al., 2016).
For these reasons, *in vitro* models are ideal candidates for designing and testing treatments for diseases that cause disorders in brain pathways. Among them, neuronal stimulation is a

valid strategy to restore lost neural functions and correct disordered neural circuits in neurological diseases. Some of the most commonly employed neuromodulation approaches require invasive procedures, e.g. electrical signals applied directly to the brain (Hassler et al., 2011). This type of stimulation has the capability to recover different symptoms in several diseases (e.g. depression, Alzheimer's disease, and schizophrenia) but require invasive and potentially dangerous surgery (Bronstein et al., 2011) and problems occur in biocompatibility (Marin & Fernández, 2010) and surgery (Bronstein et al., 2011). Over the past decades, less invasive neuromodulation techniques based on electromagnetic fields have been proposed (e.g. transcranial magnetic stimulation, transcranial direct current stimulation), but an intrinsic limit of these methods is the poor spatial resolution (in the order of centimeters) (Thielscher et al., 2011) (Thielscher & Kammer, 2004). Despite the limits, wireless and non-invasive stimulation of the central nervous system seems promising not only for the treatment of a variety of pathological conditions, such as, epilepsy, chronic pain, and obsessive-compulsive disorders, but also for reducing the debilitating motor symptoms of movement disorders such as Parkinson's disease, dystonia, and essential tremor (Grossman et al., 2017; Sanches et al., 2021; Vucic & Kiernan, 2017).

Ultrasound (US) offers the attractive combination of non-invasiveness (it can be exploited for trans-cranial stimulation without the requirement of surgical processes), and relatively high spatial resolution (Marino et al., 2015) (it can be focused virtually anywhere within the brain with a spatial resolution of few millimeters). US is a mechanical non-ionizing radiation with frequencies above 20 kHz. The apparent harmlessness, combined with the wide range of versatility, has greatly encouraged its use in the medical field, particularly in diagnostics and therapy. US radiation was initially used to modulate the spontaneous activity patterns of neurons by reversibly stimulating (Gavrilov et al., 1976) and suppressing (Fry et al., 1958) their activity. From those pioneering works, several studies tried to replicate and extend these findings, demonstrating that the electrophysiological activity can be effectively controlled/modulated by the US, as recently reviewed in (Blackmore et al., 2019). However, despite the experimental evidences, the mechanisms underlying this modulation have not been fully established. The great advantage of US stimulation compared to other modulating techniques is linked to the fact that it can be selective, targeted, reversible and, as stated above, non-invasive with precision on a millimeter scale (Lee et al., 2016). In addition, US does not require the genetic modifications of neurons by means of virus that limits the *in vivo* applications like optogenetics (Spangler & Bruchas, 2017). Although many studies have focused on US stimulation as a non-invasive neuromodulation technique, the results achieved are different and often in disagreement with each other. Some studies argue that pulsed US is more effective to generate responses (H. Kim et al., 2014), while other suggests to use a continuous US (King et al., 2013); still, although most studies have shown that US is capable to increase neuronal electrophysiological activity, others have proved that US leads to the suppression of the same activity (H.-B. Kim et al., 2017; Koroleva et al., 1986; Rinaldi et al., 1991; Tyler et

al., 2008). Furthermore, the relationship between US intensity and the response amplitude or the response existence was found to be positive (Kamimura et al., 2015), flat with all or no responses (King et al., 2013), or negative (Tufail et al., 2010). A possible explanation of such a high degree of variability is linked to the different experimental configurations like the cellular preparations, and the complex interactions between inhibition and activation in the inhibitory and excitatory networks (Salih et al., 2005).

The spatial resolution achievable with US stimulation is related with the US frequency (Clement et al 2005). Thus, stimulation of a specific brain region, which requires a low frequency (< 1 MHz) for deep tissue penetration, will lead to a low spatial resolution (Menz et al., 2013).

US can be used in conjunction with nanomaterials to achieve a minimally invasive neuronal stimulation technique but with a good spatial resolution. The properties of nanomaterials allow them to be used as mediators to translate a remotely transmitted primary stimulus into a localized secondary stimulus on the cell-nanomaterial interface (Marino et al., 2020). In particular, piezoelectric nanomaterials can convert US to electrical fields, allowing neural stimulation through low-intensity US (Marino et al., 2015)(Qiu et al., 2019). In addition, nanomaterials, such as nanoparticles, could be used as a localized transducer remotely driven by either an electromagnetic or acoustic control signal and transformed into an appropriate neuronal stimulus, allowing both subcellular spatial resolution and response time within the millisecond range.

Another possible application of US stimulation is through its action on mechano-responsive components of the cells, which sense physical forces and initiate cellular signaling. Practically, the mechanosensitive channels respond to the cell's internal pressure by opening as it reaches harmful thresholds (Cox et al., 2019). They detect pressure by sensing variations in the membrane's properties. When the membrane is strained by the high internal pressure, it undergoes a conformational transition, which allows the channel to open. Different channels in the cell open at various pressure ranges. Such mechano-responsive channels are implicated in sensing a wide variety of physical stimuli, including sound, membrane stretch, and shear forces (Martinac, 2012). Some mechanosensitive ion channels have been shown to be activated by US, but they are not expressed in neuronal cells (Ibsen et al., 2015; Kubanek et al., 2018; Ye et al., 2018) (Kubanek et al., 2016). Among the possible ultrasound-responsive mechanosensitive ion channels, Piezo family is a prominent candidate (Coste et al., 2010). Piezos are very large, evolutionarily conserved transmembrane proteins, and in particular Piezo1 is the most sensitive channel to physical force (Cox et al., 2017). Although it allows cations to permeate cells in general, it is reported to exhibit a preference for calcium ions (Coste et al., 2010). Several studies are currently devoted to understand whether endogenous Piezo1 in neurons can be activated by US and what role this interaction may play in ultrasound-induced neuro-stimulation.

Pharmacological treatment of neuronal diseases is a more consolidated approach than

physical brain stimulation. The development of a drug is a complex and time consuming process that involves multiple rounds of assays and tests. The consideration of drug efficacy and safety are present throughout its entire development process, from screening of potential molecules to the last stage of pre-clinical trials (before human testing). Also in this case, *in vitro* models are one of the primary approaches used by researchers to produce high-quality data on the safety and efficacy of drug candidates. In particular , the development of increasingly advanced micro- and nano-scale systems for drug delivery has received enormous attention (Patra et al., 2018). The need for drug delivery systems stems from the fact that drug efficacy is often impaired by cell and tissue non-specific bioavailability. Moreover, some drugs are rapidly metabolized or expelled from the body. The possibility to control the release of the drug can minimize the side effects associated with its systemic administration, which affects both healthy and diseased tissues. Overall, the controlled release results in an increase of the efficacy and safety of the drug itself compared to traditional administration methods (Ahmed et al., 2015). Main carrier-mediated drug delivery techniques include liposomes, polymer nanoparticles, micelles, and dendrimers (Chamundeeswari et al., 2019; Tiwari et al., 2012). To control drug release and its dynamics, carriers can be engineered in order to respond to specific endogenous or exogenous stimuli (i.e. control signals from outside the body). Following this approach, it is possible to obtain a specific spatial and temporal distribution of the drug (Vipul & Moinuddin, 2012), which is sometime called *pulsatile drug delivery*.

Thanks to their features, US is widely used in drug delivery applications: US can be used as an effective method to achieve spatiotemporal regulation of drug release at the desired site, preventing harmful side effects on healthy tissues. Most of the times however, US is applied using ultrasonic baths or ultrasonic cell destroyers (De Geest et al., 2007; Husseini et al., 2000; Vannozzi et al., 2015). These systems, although effective for the purpose of *in vitro* drug release, are difficult to translate *in vivo*, as the characteristics of the ultrasound are not biocompatible and the geometry of the sound source is not suitable for in vivo operation. For the drug delivery, US technique was combined with biocompatible and biodegradable nano-engineered polymeric capsules (NPCs) as a micro-carrier, fabricated by means of the electrostatic layer-by-layer self-assembly technique (LbL). LbL multilayers were first reported by (Decher et al. in 1992), who deposited alternating layers of anionic and cationic polyelectrolytes from solution onto a charged planar substrate (Decher et al., 1992). NPCs are fabricated through the LbL self-assembly of a multi-layered shell onto a sacrificial micro-core (Donath et al., 1998; Sukhorukov et al., 1998). The main advantages of LbL-manufactured NPCs are their load capacity and the possibility of precisely adapting their properties by choosing the shell components. In addition, in response to external physical stimuli such as magnetic field, light or US, encapsulated materials may be released

(Lu et al., 2005; Manju & Sreenivasan, 2011; Wohl & Engbersen, 2012).

Up to here, I have stressed the importance of *in vitro* experiments in order to successfully establish systems for drug delivery, neuronal modulation, neuronal stimulation, and genetic modification that can then be later implicated *in vivo*. However most of the *in vitro* studies present two weak spots, namely the lack of a spatial segregation (modularity) and the lack of a three dimensional (3D) topology. Indeed, *in vivo* brain areas (characterized by well-defined neuronal families with their own identity) are neither completely connected with each other nor randomly linked: their interconnections show an intricate modular organization (Newman, 2006). Brain is truly 3D, and such a spatial organization deeply influences the emergent patterns of electrophysiological activity (Fonseca et al., 2018). For these reasons, new classes of *in vitro* models should meet two requirements: i) micro-fabricated substrates or chemically functionalized surfaces that segregate (compartmentalize) neuronal populations in order to ensure a modular topological organization; ii) biocompatible scaffolds to allow a 3D growth of neuronal processes.

The engineering of neuronal networks over the active area of MEAs is a possible solution to locate neuronal assemblies spatially: to "build" a modular organization of the in vitro brain, different strategies have been proposed by involving the use of Poly-dimethyl-siloxane (PDMS) mask to the surface of a MEA (Kanagasabapathi et al., 2011; Majumdar et al., 2011). In the years, many researchers realized several simple models of brain on a chip by plating different types of neurons (i.e., cortex, hippocampus, thalamus, etc) to study the reciprocal interactions in terms of dynamics and connectivity (Dauth et al., 2017; Kanagasabapathi et al., 2012). Thus, it was demonstrated the importance to have a model where different neuronal types co-exist and interact by observing more complex dynamics when compared to the homogeneous controls (i.e., only one kind of neuronal family). Co-culturing different neuronal types also offers the possibility to investigate pathological condition (Takayama et al., 2012).

In parallel, to mimic the actual *in vivo* structure of the brain, different attempts have been performed to organize neuronal ensembles in 3D. Most of the published works investigated the relevance of the scaffold material to emulate the biochemical and mechanical features of the extracellular matrix (Cukierman et al., 2001), which result in a realistic neuronal density and connectivity. Synthetic and natural hydrogels have been used to develop 3D models, by exploiting their hydrophilicity, biocompatibility, and tunable micro-porosity (Lantoine et al., 2016). Although several studies explored the mechanical and biocompatibility properties of these materials, only few of these correlate the results with recordings showing the differences in terms of functional and dynamical properties with respect to 2D networks: with glass microbeads (Frega et al., 2014), and with bio-polymer (Bosi et al., 2015).

In this thesis, after a description of the materials and methods involved in my study, the work I have done in the four aforementioned topics is described. The thesis is organized in 5 chapters and one appendix reporting the description of the algorithms used to characterize the electrophysiological recordings. In particular,

- Chapter 2 describes the work regarding US stimulation coupled to barium titanate nanoparticles on *in vitro* primary cultures of cortical neurons to study the induced effects on the electrophysiological activity

- Chapter 3 describes a technique based on US stimulation of a model cell line (HEK293) that over expresses mechanosensitive ion channels (Piezo1). This part of the work was performed in collaboration with the group of Dr. Michael Pusch at the Institute for biophysics of the Consiglio Nazionale delle Ricerca (CNR) in Genova, Italy.

- Chapter 4 describes a US-mediated drug delivery protocol developed for carrier disruption under conditions compatible with cells and tissues. I used biocompatible and biodegradable nano-engineered polymeric capsules (NPCs) as a micro-carrier, fabricated by means of the electrostatic layer-by-layer self-assembly technique (LbL)

- Chapter 5 describes the work regarding a 3D *in vitro* model of the cortical-hippocampal circuit coupled to MEAs. I evaluated how the cortical dynamics can be shaped when external biological input (hippocampal afferents) and realistic connectivity conditions (modularity and three-dimensionality) are introduced.

References

Ahmed, S. E., Martins, A. M., & Husseini, G. A. (2015). The use of ultrasound to release chemotherapeutic drugs from micelles and liposomes. In *Journal of Drug Targeting* (Vol. 23, Issue 1, pp. 16–42). Informa Healthcare. https://doi.org/10.3109/1061186X.2014.954119

Bassett, D. S., & Bullmore, E. T. (2009). Human brain networks in health and disease. In *Current Opinion in Neurology* (Vol. 22, Issue 4, pp. 340–347). https://doi.org/10.1097/WCO.0b013e32832d93dd

Blackmore, J., Shrivastava, S., Sallet, J., Butler, C. R., & Cleveland, R. O. (2019). Ultrasound Neuromodulation: A Review of Results, Mechanisms and Safety. In *Ultrasound in Medicine and Biology* (Vol. 45, Issue 7, pp. 1509–1536). Elsevier USA. https://doi.org/10.1016/j.ultrasmedbio.2018.12.015

Bosi, S., Rauti, R., Laishram, J., Turco, A., Lonardoni, D., Nieus, T., Prato, M., Scaini, D., & Ballerini, L. (2015). From 2D to 3D: Novel nanostructured scaffolds to investigate signalling in reconstructed neuronal networks. *Scientific Reports*, *5*, 1–11. https://doi.org/10.1038/srep09562

Brewer, G. J., Boehler, M. D., Ide, A. N., & Wheeler, B. C. (2009). Chronic electrical stimulation of cultured hippocampal networks increases spontaneous spike rates. *Journal of Neuroscience Methods*, *184*(1), 104–109. https://doi.org/10.1016/j.jneumeth.2009.07.031

Bronstein, J. M., Tagliati, M., Alterman, R. L., Lozano, A. M., Volkmann, J., Stefani, A., Horak, F. B., Okun, M. S., Foote, K. D., Krack, P., Pahwa, R., Henderson, J. M., Hariz, M. I., Bakay, R. A., Rezai, A., Marks, W. J., Moro, E., Vitek, J. L., Weaver, F. M., … DeLong, M. R. (2011). Deep brain stimulation for Parkinson disease an expert consensus and review of key issues. In *Archives of Neurology* (Vol. 68, Issue 2, pp. 165–171). https://doi.org/10.1001/archneurol.2010.260

Bullmore, E., & Sporns, O. (2009). Complex brain networks: Graph theoretical analysis of structural and functional systems. In *Nature Reviews Neuroscience* (Vol. 10, Issue 3, pp. 186–198). Nat Rev Neurosci. https://doi.org/10.1038/nrn2575

Chamundeeswari, M., Jeslin, J., & Verma, M. L. (2019). Nanocarriers for drug delivery applications. In *Environmental Chemistry Letters* (Vol. 17, Issue 2, pp. 849–865). Springer. https://doi.org/10.1007/s10311-018-00841-1

Chiappalone, M., Massobrio, P., & Martinoia, S. (2008). Network plasticity in cultured cortical assemblies. *European Journal of Neuroscince*, *28*, 221–237. https://doi.org/https://doi.org/10.1111/j.1460-9568.2008.06259.x

Coste, B., Mathur, J., Schmidt, M., Earley, T. J., Ranade, S., Petrus, M. J., Dubin, A. E., & Patapoutian, A. (2010). Piezo1 and Piezo2 are essential components of distinct mechanically activated cation channels. *Science*, *330*(6000), 55–60. https://doi.org/10.1126/science.1193270

Cox, C. D., Bavi, N., & Martinac, B. (2017). Origin of the Force: The Force-From-Lipids Principle Applied to Piezo Channels. *Current Topics in Membranes*, *79*, 59–96. https://doi.org/10.1016/bs.ctm.2016.09.001

Cox, Charles D., Bavi, N., & Martinac, B. (2019). Biophysical Principles of Ion-Channel-Mediated Mechanosensory Transduction. In *Cell Reports* (Vol. 29, Issue 1, pp. 1–12). Elsevier B.V. https://doi.org/10.1016/j.celrep.2019.08.075

Cukierman, E., Pankov, R., Stevens, D. R., & Yamada, K. M. (2001). Taking cell-matrix adhesions to the third dimension. *Science*, *294*(5547), 1708–1712. https://doi.org/10.1126/science.1064829

Dauth, S., Maoz, B. M., Sheehy, S. P., Hemphill, M. A., Murty, T., Macedonia, M. K., Greer, A. M., Budnik, B., & Parker, K. K. (2017). Neurons derived from different brain regions are inherently different in vitro: A novel multiregional brain-on-a-chip. *Journal of Neurophysiology*, *117*(3), 1320–1341. https://doi.org/10.1152/jn.00575.2016

De Geest, B. G., Skirtach, A. G., Mamedov, A. A., Antipov, A. A., Kotov, N. A., De Smedt, S. C., & Sukhorukov, G. B. (2007). Ultrasound-triggered release from multilayered capsules. *Small*, *3*(5), 804–808. https://doi.org/10.1002/smll.200600441

Decher, G., Hong, J. D., & Schmitt, J. (1992). Buildup of ultrathin multilayer films by a self-assembly process: III. Consecutively alternating adsorption of anionic and cationic polyelectrolytes on charged surfaces. *Thin Solid Films*, *210–211*(PART 2), 831–835. https://doi.org/10.1016/0040-6090(92)90417-A

Donath, E., Sukhorukov, G. B., Caruso, F., Davis, S. A., & Möhwald, H. (1998). Novel Hollow Polymer Shells by Colloid-Templated Assembly of Polyelectrolytes. *Angewandte Chemie International Edition*, *37*(16), 2201–2205. https://doi.org/10.1002/(sici)1521-3773(19980904)37:16<2201::aid-anie2201>3.0.co;2-e

Fonseca, M. de C., Araujo, B. H. S., Dias, C. S. B., Archilha, N. L., Neto, D. P. A., Cavalheiro, E., Westfahl, H., da Silva, A. J. R., & Franchini, K. G. (2018). High-resolution synchrotron-based X-ray microtomography as a tool to unveil the three-dimensional neuronal architecture of the brain. *Scientific Reports*, *8*(1), 1–13. https://doi.org/10.1038/s41598-018-30501-x

Frega, M., Tedesco, M., Massobrio, P., Pesce, M., & Martinoia, S. (2014). Network dynamics of 3D engineered neuronal cultures: A new experimental model for in-vitro electrophysiology. *Scientific Reports*, *4*(May). https://doi.org/10.1038/srep05489

Fry, F. J., Ades, H. W., & Fry, W. J. (1958). Production of reversible changes in the central nervous system by ultrasound. *Science*, *127*(3289), 83–84. https://doi.org/10.1126/science.127.3289.83

Gavrilov, L. R., Gersuni, G. V., Ilyinsky, O. B., Sirotyuk, M. G., Tsirulnikov, E. M., & Shchekanov, E. E. (1976). The Effect of Focused Ultrasound on the Skin and Deep Nerve Structures of Man and Animal. *Progress in Brain Research*, *43*(C), 279–292. https://doi.org/10.1016/S0079-6123(08)64360-5

Gross, G. W., Rhoades, B. K., Azzazy, H. M. E., & Ming-Chi Wu. (1995). The use of neuronal networks on multielectrode arrays as biosensors. *Biosensors and Bioelectronics*, *10*(6–7), 553–567. https://doi.org/10.1016/0956-5663(95)96931-N

Gross, G. W., Rhoades, B. K., & Jordan, R. J. (1992). Neuronal networks for biochemical sensing. *Sensors and Actuators B-Chemical*, *6*, 1–8. https://doi.org/10.1016/0925-4005(92)80022-P

Grossman, N., Bono, D., Dedic, N., Kodandaramaiah, S. B., Rudenko, A., Suk, H. J., Cassara, A. M., Neufeld, E., Kuster, N., Tsai, L. H., Pascual-Leone, A., & Boyden, E. S. (2017). Noninvasive Deep Brain Stimulation via Temporally Interfering Electric Fields. *Cell*, *169*(6), 1029-1041.e16. https://doi.org/10.1016/j.cell.2017.05.024

Hassler, C., Boretius, T., & Stieglitz, T. (2011). Polymers for neural implants. *Journal of Polymer Science Part B: Polymer Physics*, *49*(1), 18–33. https://doi.org/10.1002/polb.22169

Herculano-Houzel, S. (2012). The remarkable, yet not extraordinary, human brain as a scaled-up primate brain and its associated cost. In *Proceedings of the National Academy of Sciences of the United States of America* (Vol. 109, Issue SUPPL.1, pp. 10661–10668). National Academy of Sciences. https://doi.org/10.1073/pnas.1201895109

Husseini, G. A., El-Fayoumi, R. I., O'Neill, K. L., Rapoport, N. Y., & Pitt, W. G. (2000). DNA damage induced by micellar-delivered doxorubicin and ultrasound: Comet assay study. *Cancer Letters*, *154*(2), 211–216. https://doi.org/10.1016/S0304-3835(00)00399-2

Ibsen, S., Tong, A., Schutt, C., Esener, S., & Chalasani, S. H. (2015). Sonogenetics is a non-invasive approach to activating neurons in Caenorhabditis elegans. *Nature Communications*, *6*(1), 1–12. https://doi.org/10.1038/ncomms9264

Kamimura, H., Wang, S., Chen, H., Wang, Q., Aurup, C., Acosta, C., Carneiro, A., & Konofagou, E. (2015). *Pupil dilation and motor response elicitation by ultrasound neuromodulation*. https://doi.org/10.1109/ULTSYM.2015.0070

Kanagasabapathi, T. T., Ciliberti, D., Martinoia, S., Wadman, W. J., & Decré, M. M. J. (2011). Dual-compartment neurofluidic system for electrophysiological measurements in physically segregated and functionally connected neuronal cell culture. *Frontiers in Neuroengineering*, *4*(OCTOBER), 2. https://doi.org/10.3389/fneng.2011.00013

Kanagasabapathi, T. T., Massobrio, P., Barone, R. A., Tedesco, M., Martinoia, S., Wadman, W. J., & Decré, M. M. J. (2012). Functional connectivity and dynamics of cortical-thalamic networks co-cultured in a dual compartment device. *Journal of Neural Engineering*, *9*(3). https://doi.org/10.1088/1741-2560/9/3/036010

Kim, H.-B., Swanberg, K. M., Han, H.-S., Kim, J.-C., Kim, J.-W., Lee, S., Lee, C. J., Maeng, S., Kim, T.-S., & Park, J.-H. (2017). Prolonged stimulation with low-intensity ultrasound induces delayed increases in spontaneous hippocampal culture spiking activity. *Journal of Neuroscience Research*, *95*(3), 885–896. https://doi.org/10.1002/jnr.23845

Kim, H., Chiu, A., Lee, S. D., Fischer, K., & Yoo, S. S. (2014). Focused ultrasound-mediated non-invasive brain stimulation:

Examination of sonication parameters. *Brain Stimulation*, *7*(5), 748–756. https://doi.org/10.1016/j.brs.2014.06.011

King, R. L., Brown, J. R., Newsome, W. T., & Pauly, K. B. (2013). Effective parameters for ultrasound-induced in vivo neurostimulation. *Ultrasound in Medicine and Biology*, *39*(2), 312–331. https://doi.org/10.1016/j.ultrasmedbio.2012.09.009

Koroleva, V. I., Vykhodtseva, N. I., & Elagin, V. A. (1986). Cortical and subcortical spreading depression in rats produced by focused ultrasound. *Neurophysiology*, *18*(1), 43–48. https://doi.org/10.1007/BF01052490

Kubanek, J., Shi, J., Marsh, J., Chen, D., Deng, C., & Cui, J. (2016). Ultrasound modulates ion channel currents. *Scientific Reports*, *6*. https://doi.org/10.1038/srep24170

Kubanek, J., Shukla, P., Das, A., Baccus, S. A., & Goodman, M. B. (2018). Ultrasound elicits behavioral responses through mechanical effects on neurons and ion channels in a simple nervous system. *Journal of Neuroscience*, *38*(12), 3081–3091. https://doi.org/10.1523/JNEUROSCI.1458-17.2018

Lantoine, J., Grevesse, T., Villers, A., Delhaye, G., Mestdagh, C., Versaevel, M., Mohammed, D., Bruyère, C., Alaimo, L., Lacour, S. P., Ris, L., & Gabriele, S. (2016). Matrix stiffness modulates formation and activity of neuronal networks of controlled architectures. *Biomaterials*, *89*, 14–24. https://doi.org/10.1016/j.biomaterials.2016.02.041

Lee, W., Lee, S. D., Park, M. Y., Foley, L., Purcell-Estabrook, E., Kim, H., Fischer, K., Maeng, L. S., & Yoo, S. S. (2016). Image-Guided Focused Ultrasound-Mediated Regional Brain Stimulation in Sheep. *Ultrasound in Medicine and Biology*, *42*(2), 459–470. https://doi.org/10.1016/j.ultrasmedbio.2015.10.001

Lu, Z., Prouty, M. D., Quo, Z., Golub, V. O., Kumar, C. S. S. R., & Lvov, Y. M. (2005). Magnetic switch of permeability for polyelectrolyte microcapsules embedded with Co@Aunanoparticles. *Langmuir*, *21*(5), 2042–2050. https://doi.org/10.1021/la047629q

Majumdar, D., Gao, Y., Li, D., & Webb, D. J. (2011). Co-culture of neurons and glia in a novel microfluidic platform. *Journal of Neuroscience Methods*, *196*(1), 38–44. https://doi.org/10.1016/j.jneumeth.2010.12.024

Manju, S., & Sreenivasan, K. (2011). Enhanced drug loading on magnetic nanoparticles by layer-by-layer assembly using drug conjugates: Blood compatibility evaluation and targeted drug delivery in cancer cells. *Langmuir*, *27*(23), 14489–14496. https://doi.org/10.1021/la202470k

Marin, C., & Fernández, E. (2010). Biocompatibility of intracortical microelectrodes: Current status and future prospects. *Frontiers in Neuroengineering*, *3*(MAY). https://doi.org/10.3389/fneng.2010.00008

Marino, A., Arai, S., Hou, Y., Sinibaldi, E., Pellegrino, M., Chang, Y. T., Mazzolai, B., Mattoli, V., Suzuki, M., & Ciofani, G. (2015). Piezoelectric Nanoparticle-Assisted Wireless Neuronal Stimulation. *ACS Nano*, *9*(7), 7678–7689. https://doi.org/10.1021/acsnano.5b03162

Marino, A., Genchi, G. G., Pisano, M., Massobrio, P., Tedesco, M., Martinoia, S., Raiteri, R., & Ciofani, G. (2020). Nanomaterial-Assisted Acoustic Neural Stimulation. In *Neural Interface Engineering* (pp. 347–363). Springer International Publishing. https://doi.org/10.1007/978-3-030-41854-0_15

Massobrio, P., Pasquale, V., & Martinoia, S. (2015). Self-organized criticality in cortical assemblies occurs in concurrent scale-free and small-world networks. *Scientific Reports*, *5*(April), 1–16. https://doi.org/10.1038/srep10578

Menz, M. D., Oralkan, Ö., Khuri-Yakub, P. T., & Baccus, S. A. (2013). Precise neural stimulation in the retina using focused ultrasound. *Journal of Neuroscience*, *33*(10), 4550–4560. https://doi.org/10.1523/JNEUROSCI.3521-12.2013

Napoli, A., Xie, J., & Obeid, I. (2014). Understanding the temporal evolution of neuronal connectivity in cultured networks using statistical analysis. *BMC Neuroscience*, *15*(January). https://doi.org/10.1186/1471-2202-15-17

Newman, M. E. J. (2006). Modularity and community structure in networks. *Proceedings of the National Academy of Sciences of the United States of America*, *103*(23), 8577–8582. https://doi.org/10.1073/pnas.0601602103

Pasquale, V., Massobrio, P., Bologna, L. L., Chiappalone, M., & Martinoia, S. (2008). Self-organization and neuronal avalanches in networks of dissociated cortical neurons. *Neuroscience*, *153*(4), 1354–1369. https://doi.org/10.1016/j.neuroscience.2008.03.050

Patra, J. K., Das, G., Fraceto, L. F., Campos, E. V. R., Rodriguez-Torres, M. D. P., Acosta-Torres, L. S., Diaz-Torres, L. A., Grillo, R., Swamy, M. K., Sharma, S., Habtemariam, S., & Shin, H. S. (2018). Nano based drug delivery systems: Recent developments and future prospects. In *Journal of Nanobiotechnology* (Vol. 16, Issue 1, p. 71). BioMed Central Ltd. https://doi.org/10.1186/s12951-018-0392-8

Poli, D., & Massobrio, P. (2018). High-frequency electrical stimulation promotes reshaping of the functional connections and synaptic plasticity in in vitro cortical networks. *Physical Biology*, *15*(6). https://doi.org/10.1088/1478-3975/aae43e

Poli, D., Pastore, V. P., Martinoia, S., & Massobrio, P. (2016). From functional to structural connectivity using partial correlation in neuronal assemblies. *Journal of Neural Engineering*, *13*(2), 26023. https://doi.org/10.1088/1741-2560/13/2/026023

Qiu, Z., Guo, J., Kala, S., Zhu, J., Xian, Q., Qiu, W., Li, G., Zhu, T., Meng, L., Zhang, R., Chan, H. C., Zheng, H., & Sun, L. (2019). The Mechanosensitive Ion Channel Piezo1 Significantly Mediates In Vitro Ultrasonic Stimulation of Neurons. *IScience*, *21*, 448–457. https://doi.org/10.1016/j.isci.2019.10.037

Rinaldi, P. C., Jones, J. P., Reines, F., & Price, L. R. R. (1991). Modification by focused ultrasound pulses of electrically evoked responses from an in vitro hippocampal preparation. *Brain Research*, *558*(1), 36–42. https://doi.org/10.1016/0006-8993(91)90711-4

Salih, F., Khatami, R., Steinheimer, S., Hummel, O., Kühn, A., & Grosse, P. (2005). Inhibitory and excitatory intracortical circuits across the human sleep-wake cycle using paired-pulse transcranial magnetic stimulation. *The Journal of Physiology*, *565*(2), 695–701. https://doi.org/10.1113/jphysiol.2004.082040

Sanches, C., Stengel, C., Godard, J., Mertz, J., Teichmann, M., Migliaccio, R., & Valero-Cabré, A. (2021). Past, Present, and Future of Non-invasive Brain Stimulation Approaches to Treat Cognitive Impairment in Neurodegenerative Diseases: Time for a Comprehensive Critical Review. In *Frontiers in Aging Neuroscience* (Vol. 12). Frontiers Media S.A. https://doi.org/10.3389/fnagi.2020.578339

Spangler, S. M., & Bruchas, M. R. (2017). Optogenetic approaches for dissecting neuromodulation and GPCR signaling in neural circuits. In *Current Opinion in Pharmacology* (Vol. 32, pp. 56–70). Elsevier Ltd. https://doi.org/10.1016/j.coph.2016.11.001

Sukhorukov, G. B., Donath, E., Lichtenfeld, H., Knippel, E., Knippel, M., Budde, A., & Möhwald, H. (1998). Layer-by-layer self assembly of polyelectrolytes on colloidal particles. *Colloids and Surfaces A: Physicochemical and Engineering Aspects*, *137*(1–3), 253–266. https://doi.org/10.1016/S0927-7757(98)00213-1

Takayama, Y., Moriguchi, H., Kotani, K., Suzuki, T., Mabuchi, K., & Jimbo, Y. (2012). Network-wide integration of stem cell-derived neurons and mouse cortical neurons using microfabricated co-culture devices. *BioSystems*, *107*(1), 1–8. https://doi.org/10.1016/j.biosystems.2011.08.001

Taketani, M., & Baudry, M. (2006). *Advances in network electrophysiology: using Multi-Electrode Array* (S. New York (Ed.)).

Thielscher, A., & Kammer, T. (2004). Electric field properties of two commercial figure-8 coils in TMS: Calculation of focality and efficiency. *Clinical Neurophysiology*, *115*(7), 1697–1708. https://doi.org/10.1016/j.clinph.2004.02.019

Thielscher, A., Opitz, A., & Windhoff, M. (2011). Impact of the gyral geometry on the electric field induced by transcranial magnetic stimulation. *NeuroImage*, *54*(1), 234–243. https://doi.org/10.1016/j.neuroimage.2010.07.061

Tiwari, G., Tiwari, R., Bannerjee, S., Bhati, L., Pandey, S., Pandey, P., & Sriwastawa, B. (2012). Drug delivery systems: An updated review. *International Journal of Pharmaceutical Investigation*, *2*(1), 2. https://doi.org/10.4103/2230-973x.96920

Tufail, Y., Matyushov, A., Baldwin, N., Tauchmann, M. L., Georges, J., Yoshihiro, A., Tillery, S. I. H., & Tyler, W. J. (2010). Transcranial Pulsed Ultrasound Stimulates Intact Brain Circuits. *Neuron*, *66*(5), 681–694. https://doi.org/10.1016/j.neuron.2010.05.008

Tyler, W. J., Tufail, Y., Finsterwald, M., Tauchmann, M. L., Olson, E. J., & Majestic, C. (2008). Remote excitation of neuronal circuits using low-intensity, low-frequency ultrasound. *PLoS ONE*, *3*(10). https://doi.org/10.1371/journal.pone.0003511

Vannozzi, L., Ricotti, L., Filippeschi, C., Sartini, S., Coviello, V., Piazza, V., Pingue, P., La Motta, C., Dario, P., & Menciassi, A. (2015). Nanostructured ultra-thin patches for ultrasound-modulated delivery of anti-restenotic drug. *International Journal of Nanomedicine*, *11*, 69–92. https://doi.org/10.2147/IJN.S92031

Vipul, P., & Moinuddin, S. (2012). *Pulsatile drug delivery system for treatment of various Inflammatory Disorders: A Review*.

Vucic, S., & Kiernan, M. C. (2017). Transcranial Magnetic Stimulation for the Assessment of Neurodegenerative Disease. In *Neurotherapeutics* (Vol. 14, Issue 1, pp. 91–106). Springer New York LLC. https://doi.org/10.1007/s13311-016-0487-6

Wagenaar, D. A., Madhavan, R., Pine, J., & Potter, S. M. (2005). Controlling bursting in cortical cultures with closed-loop multi-electrode stimulation. *Journal of Neuroscience*, *25*(3), 680–688. https://doi.org/10.1523/JNEUROSCI.4209-04.2005

Wagenaar, D. A., Pine, J., & Potter, S. M. (2006). An extremely rich repertoire of bursting patterns during the development of cortical cultures. *BMC Neuroscience*, *7*, 1–18. https://doi.org/10.1186/1471-2202-7-11

WHO | World Health Organization. (n.d.). Retrieved April 5, 2021, from https://www.who.int/

Wohl, B. M., & Engbersen, J. F. J. (2012). Responsive layer-by-layer materials for drug delivery. In *Journal of Controlled Release* (Vol. 158, Issue 1, pp. 2–14). Elsevier. https://doi.org/10.1016/j.jconrel.2011.08.035

Ye, J., Tang, S., Meng, L., Li, X., Wen, X., Chen, S., Niu, L., Li, X., Qiu, W., Hu, H., Jiang, M., Shang, S., Shu, Q., Zheng, H., Duan, S., & Li, Y. (2018). Ultrasonic Control of Neural Activity through Activation of the Mechanosensitive Channel MscL. *Nano Letters*, *18*(7), 4148–4155. https://doi.org/10.1021/acs.nanolett.8b00935

Chapter 1

Materials & Methods

1.1 Ultrasound

1.1.1. Ultrasound biophysics and dosimetry

The *ultrasound biophysics* studies the interaction mechanisms between ultrasound and biological materials. The *ultrasound dosimetry*, on the other hand, is the quantitative determination of the interaction between the ultrasound energy and the biological materials. To better understand this interaction, it is necessary to introduce the physical characteristics of sound. Sound is a mechanical vibration which propagates as a wave of pressure through a medium (Humphrey, 2007), inducing material particles displacement. Particles are periodically compressed and rarefied into the medium, and the distance between two subsequent compression or rarefaction peaks in the propagation direction at a given instant is the wavelength λ, while the time interval between two subsequent maxima or minima in a given point in the space is the wave period T and is reciprocal value is the wave frequency f. Wavelength and frequency of a sound wave are related by the speed of propagation into the medium c:

$$f = \frac{c}{\lambda} \tag{1.1}$$

The values of c in the human body is often considered constant and equals to 1540 m/s (Shin et al., 2010). Sound waves are characterized by the wave frequency and amplitude measured in Hz and Pa, respectively. When the pressure wave contains *frequencies* all above the human audible limit (20 kHz) it is defined as an *ultrasound* (US). In this thesis

I employed US waves as a stimulation signal to elicit either an electrophysiological response or a mechanical one. An US stimulus can be applied continuously, for a certain amount of time, or in a pulsed mode. The experiments that will be discussed in this thesis were performed using US in a "pulse mode" which can be defined by four parameters: the total duration (TD), i.e., the entire time of stimulation, the period (T) corresponding to the time between two successive pulses onset, and the duty cycle (DC) representing the fraction of time that the stimulus is on relative to the T. Another fundamental parameter is the acoustic intensity (I), which is the product of particle velocity vector ($v = \frac{p(t)}{\rho_0 c}$) multiplied by acoustic pressure (p). Both I and v are vectors, which means that both have a direction as well as a magnitude. The direction of sound intensity is the average direction in which energy is flowing. As definition, the instantaneous intensity can be approximated as:

$$I(t) = \frac{p(t)^2}{\rho_0 c} \tag{1.2}$$

Where the intensity *I(t)* is commonly expressed in W/cm^2 and ρ_o is the medium density. The acoustic intensity is, however, more commonly reported in terms of spatial and temporal averaging. In particular, the spatial peak pulse average intensity (Isppa) is the ratio of the pulse intensity integral to the pulse duration, at the point of the maximal intensity. The Isppa is computed as function of the root mean square focal peak pressure (P_{RMS}) using the following expression:

$$I_{sppa} = \frac{P_{RMS}^2}{\rho_0 c} \tag{1.3}$$

In pulse mode, however, a more appropriate parameter is the spatial peak temporal average intensity (Ispta), given by:

$$I_{spta} = I_{sppa} * DC \tag{1.4}$$

All these parameters allow studying how an US beam interacts with the matter. Since 1920, several studies have focused on the search for optimal parameters to generate an ultrasound wave that crosses biological tissues (Harvey et al., 1928). Since then, due to the physical characteristics of the US, including the ability to transmit over long distances with minimal energy loss, ultrasound with frequencies between 1 and 15 MHz has been widely used in the medical applications (O'Brien, 2007). Their application span from imaging (Ahmad et al., 2009; Dalecki, 2004; Wang et al., 2003) to neuromodulation (Khraiche et al., 2008; Tufail et al., 2010; Tyler et al., 2008), passing through ablation techniques (Franzini et al., 2020). In detail, the tissue exposure to ultrasound is associated with two biophysical mechanisms to produce biological effects: thermal and non-thermal (Miller et al., 1996). Both interaction mechanisms depend on the configuration of the

device, and determine the safety of ultrasound exposure. In the first case, the acoustic energy is converted into heating, due to the absorption of the wave by the tissues. The heating is proportional to the ultrasound frequency and the time-average intensity. The second case is an indirect mechanism and involves the conversion of acoustic energy into mechanical energy of the microbubbles movement, which may include the translation of bubbles in response to radiation forces and radial oscillations in response to variable acoustic times. This phenomenon is often known as acoustic cavitation and depends on the frequency and intensity of the US, but it is more strongly correlated to the intensity of the temporal peak than to the time-average intensity. The two effects are not completely distinguishable (Haar, 1988), so it is good to assume that the non-thermal effects are always accompanied by a minimum development of heat.

Thermal and no-thermal, or mechanical, bioeffects associated to US stimulation can cause irreversible damages on tissues, depending on the properties of the exposed area and the stimulation parameters. Thus, in the past, the main goal has been to define procedures for using ultrasound to maximize the positive effects and minimize unwanted or harmful ones. To date, the US parameters used are subject to the limitations of guidelines established by the Food and Drugs Administration that introduced two indices: the mechanical index (MI) and the thermal index (TI). They were derived from an evaluation of the effects related to the potential bioeffects manifestation and were also related to the evaluation of the sound intensity.

The MI was first calculated in 1980 by Apfel and Holland (Apfel & Holland, 1991) and then it was subject of several studies (Abbott, 1999). It is a function of the peak negative pressure (PNP in MHz) derated by 0.3 $dBcm^{-1}MHz^{-1}$ and frequency f of US wave (*FDA*, 1992); it is defined as:

$$MI = \frac{PNP}{\sqrt{f}} \tag{1.5}$$

On the other hand, the TI is the ratio of the acoustic power measured at the depth of interest (W_p) to the power required to increase the temperature by 1°C (W_{deg}) given a specific tissue model (*FDA*, 1992). In its simplest forms, is defined by:

$$TI = \frac{W_p}{W_{deg}} \tag{1.6}$$

The FDA guidelines for US devices are as follow: the I_{spta} must not exceed 720 mW/cm^2, the Isppa must not exceed 190 mW/cm^2 , the MI must not exceed 1.9 and the TI must not exceed 6 (*IEC 62359*)(Duck, 2007).

1.1.2. Ultrasound set-up

In the works described in Chapters 2, 3 and 4, two different types of set up have been used

for the US emission. The first setup (henceforth called *PA setup*) is composed by a 1 MHz piezoelectric transducer (Precision Acoustics Ltd, UK) and a homemade driving unit (Fig. 1.1a). Briefly, the 1 MHz driving signal (*DS*) is generated by a commercial function generator and amplified by a home-made high voltage amplifier. All the signals are monitored by an oscilloscope. The 1 MHz transducer was a custom-built device and is mounted in a redesigned support with a micromanipulator to reproducibly reposition it with respect to the target (e.g. neuronal network) during different experiments.

The second setup (henceforth called *Sonidel setup*) was composed by a commercial transducer with its own controller: Sonidel SP100 sonoporator, operating at 1 MHz (Fig. 1.1b). It can accommodate two interchangeable different applicator heads:

- 0.8 cm^2, max output power: 5 W/cm^2
- 5.0 cm^2, max output power: 5 W/cm^2

In this case the pulse frequency can be set between 0 and 100 Hz. Both continuous and pulsed wave can be generated. US amplitude, expressed in W/cm^2, is the quotient of US power and effective radiation area, which is defined by the size of the US applier.

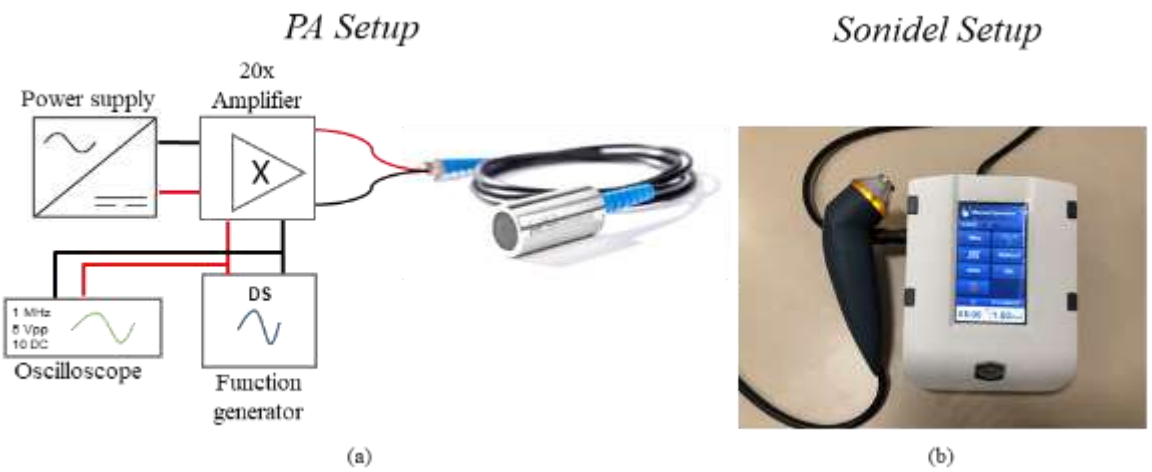

Figure 1.1: *Ultrasound setup* **(a)** *schematic representation of the homemade setup which drive the precision acoustic transducer (PA setup);* **(b)** *Sonidel SP1000 transducer (Sonidel setup)*

1.1.3. Ultrasound field mapping

Both the transducers used in the works presented in this thesis were calibrated in terms of sound pressure field (SPF) and culture medium temperature variation using a miniaturized hydrophone (Precision Acoustics, UK) and a dummy chip with a hole. In order to measure the pressure field emitted by US transducers, the shaft of the needle hydrophone was placed along the acoustic axis of the transducer, in order to obtain the maximum hydrophone signal. A hydrophone produces an electrical output signal in response to the acoustic pressure received over its active element. Clearly, the relationship between the acoustic

pressure and the voltage pressure is frequency dependent, thus, a conversion is required to obtain the acoustic pressure signal. When the source of the US only works at one frequency, as in our case, the instantaneous pressure signal (p(t)), can be calculated from the measured hydrophone voltage according to:

$$p(t) = \frac{V(t)}{M(f_{awf})} \tag{1.7}$$

Where $M(f_{awf})$ is the sensitivity of the hydrophone at the acoustic working frequency of the source given by the producer through the calibration.

In order to characterize the *PA transducer*, the *p(t)* were measured into a MEA filled with the same solution (Neurobasal medium) used in the experimental recordings. The transducer was controlled with a high voltage driving signal (C.f., Section 1.1.2.) and partially immersed into the solution. The hydrophone was placed on the bottom of the dummy MEA through a hole drilled in the active area. The US pressure field was evaluated according to three factors:

- Vertical transducer/hydrophone distance (Y-Distance)

- Lateral acoustic axis/hydrophone distance (X-Distance)

- DS amplitude

I used the micromanipulator for distance calculations in the x-y plane to shift the transducer relative to the hydrophone. In the case of the Y-Distance the transducer was aligned to the hydrophone and then shifted from 1mm to 20 mm in height with respect to the hydrophone.

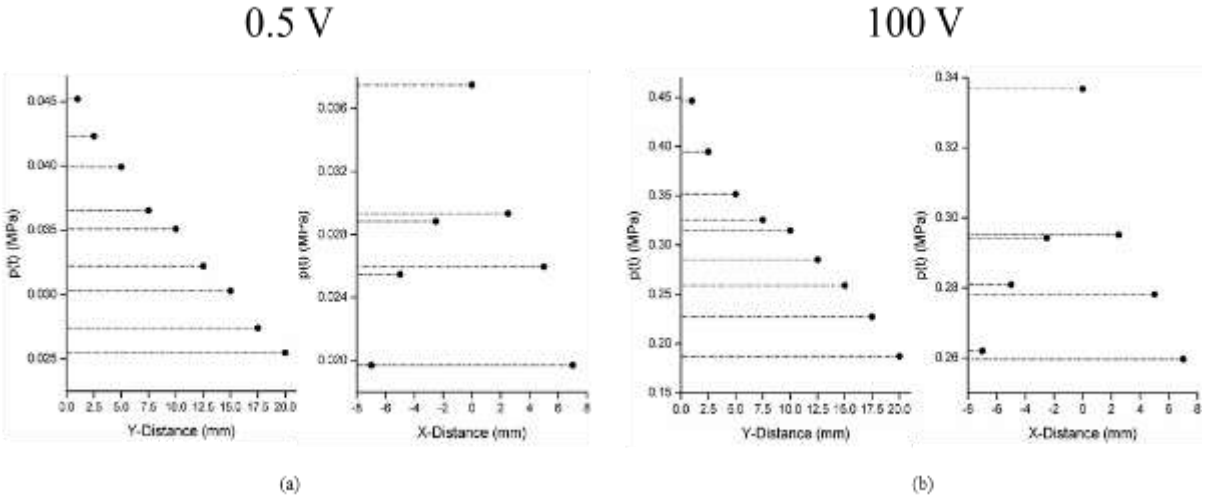

Figure 1.2: *The sound pressure field of the PA transducer estimated at* **(a)** *the lowest driving signal amplitude (0.5V) and* **(b)** *the highest driving signal amplitude (100V) as a function of the x-y distance between the transducer and the hydrophone.*

Conversely, for x-axis displacements, the transducer was located at a height of 5 mm and moved horizontally to the right and left for an overall displacement of 7 mm in both directions. Results are shown in figures 1.2a and 1.2b and were obtained for the lowest (0.5 V) and highest (100V) DS amplitude. It is noted that this SPF characterization indicates the significance of the perfect centering of the transducer (0 on x axis) over the desired field: in all cases, the SPF values are strongly reduced by 2 mm in both directions relative to the central location. Values decrease substantially as offset from the center grows. I also evaluated how the SPF changes with a function of the amplitude of DS. In this case, the transducer was positioned at 5 mm Y-Distance and 0 mm X-distance (perfectly centered). Results are reported in figure 1.3a.

A Petri dish, filled with the same Neurobasal solution, was used as a chip for the *Sonidel transducer*. In this case, the much larger transducer head does not allow significant displacements in the x-y plane, so I proceeded only with the characterization as a function of the amplitude of the signal emitted, as shown in figure 1.3b.

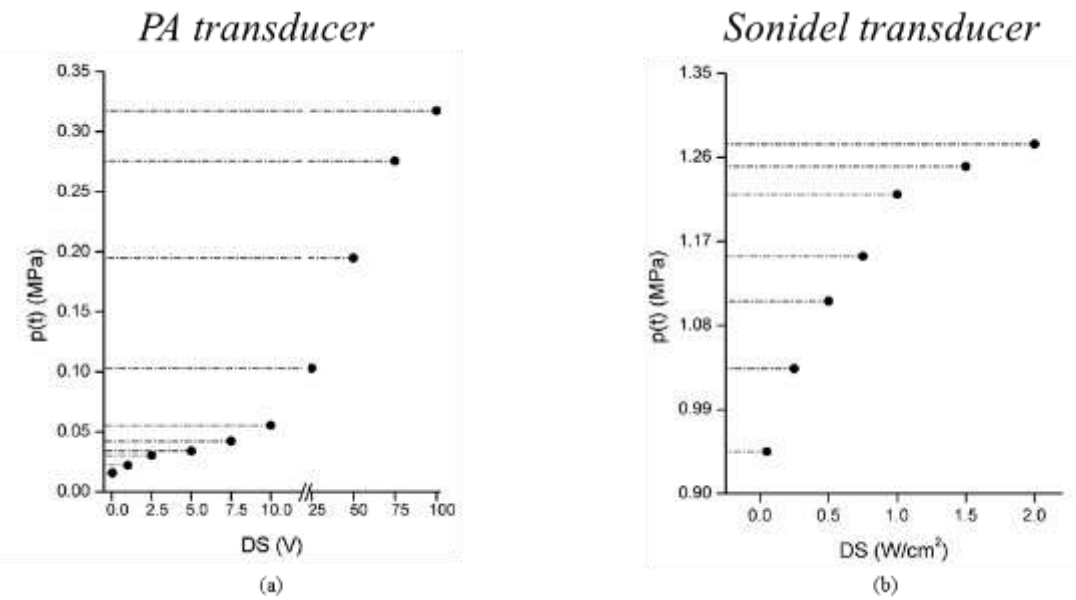

Figure 1.3 *the sound pressure level estimated as a function of DS amplitude for* **(a)** *PA transducer and* **(b)** *Sonidel transducer.*

1.2 Piezoelectric Materials

1.2.1. Barium Titanate Nanoparticles (BTNPs)

Due to its high dielectric constant (values as high as 7,000), barium titanate ($BaTiO_3$) is undoubtedly one of the most studied compounds of the perovskite-like oxides family. It is widely used for the semiconductor industry to make thermistors and piezoelectric devices. It is also employed in ferroelectric ceramics (Vijatović et al., 2008). BTNPs are synthetized to reach nanoparticle size and a crystalline phase that can be cubic, tetragonal, orthorhombic, etc.

Applications of BTNPs for biomedical purposes are relatively recent (Park et al., 1981). The good biocompatibility of the BTNPs in different cellular and animal models motivated researchers to propose several new biomedical applications for this nanomaterial (Bagchi et al., 2014; Dubey et al., 2015; Pantazis et al., n.d.). In general, for a piezoelectric material, the piezoelectric charge constant (d) is the ratio between the electric charge generated per unit area and the applied force. This means that a higher piezoelectric charge constant corresponds to higher voltage generated by the material in response to the same applied deformation. The BTNPs present a high piezoelectric charge constant when on tetragonal phase (Berlincourt & Jaffe, 1958; Wada & Tsurumi, 2004). This allows using BTNPs as a mechano-electrical transducer (Ciofani et al., 2010) to be applied locally for cell electrical stimulation (Marino et al., 2015; Rojas et al., 2018). In details, the purpose was to use the BTNPs as a localized transducer remotely driven by an ultrasound control signal which is transformed into an appropriate neuronal stimulus, allowing both subcellular spatial resolution and response time in the millisecond range.

For my experiments, BTNPs were purchased by Nanostructured & Amorphous Materials, Inc. Houston, TX (1144DY). Details of sample purity and composition, as provided by the supplier, include the following: BaO/ TiO_2 0.999-1.001, purity 99.9%; APS 300 nm; SSA 3.5-3.7m^2/g. X-ray diffraction (XRD) patterns were recorded using an X-ray powder diffractometer (Kristalloflex 810, Siemens) using Cu KR radiation (λ = 1.5406 A) at a scanning rate of 0.016° s-1 with 2θ ranging in 10°-80° at a temperature of 25 °C. For use in biological experiments, BTNPs were dispersed in aqueous environment through a noncovalent wrapping with gum Arabic (G9752 from Sigma-Aldrich). Briefly, 10 mg of nanoparticles and 10 mg of gum Arabic were mixed in 10 mL of phosphate buffered saline (PBS) solution. The samples were sonicated for 12 h with a Bransonic sonicator 2510, by using an output power of 20 W. The final product is a stable 1 mg/mL nanoparticle dispersion that was appropriately diluted in cell culture (C.f., Section 1.4.2.) medium for biological experiments. Analogous nanoparticles but with cubic crystal structure (1143DY, from Nanostructured & Amorphous Materials) were used following the same preparation procedures.

1.2.2. Piezo1 channels

A family of mechanically activated channels that counts only two members in human, piezo1 and 2, has emerged recently. Piezo proteins are detected in many mechanosensitive tissues (Coste et al., 2010). Piezos are large proteins of over 2,000 residues that are predicted to span the membrane between 30 and 40 times. They represent gigantic channels with 120 to 160 transmembrane segments, which makes them structurally different from other known ion channels. In my studies I worked with Piezo1. Piezo1 is present in non-sensory tissues and helps cells to detect local variations in fluid pressure. Beside mechanical stimuli also transmembrane voltage can modulate or even gate Piezo1 channel (Moroni et al., 2018). When Piezo1 channel opens, positive ions, such as calcium, enter the cell, activating cell's sensory response. Some structures of Piezo1 have recently been determined using cryo-electron microscopy: a low-resolution structure was developed in 2015 (Ge et al., 2015) and three more detailed structures have recently been obtained (Guo & MacKinnon, 2017; Zhao et al., 2018). These configurations showed a complex molecular machine made up of three identical subunits. The subunits come together in the center to form an ion channel that crosses the membrane, and three curved blades that stretch out of the channel, which should have the role of controlling the surrounding membrane by opening the channel in response to a distortion. The Piezo1 structures have many functional domains in their long chains. As can be seen in the figure 1.4, the blades are not flat, rather they bend the membrane, causing a cup form. A series of amino acids (magenta) allows calcium ions to reach the central channel, which is surrounded by three helices (red). A straight section (beam, green) joins each blade to the channel and hence ties the shape variations of the blades to the opening of the channel.

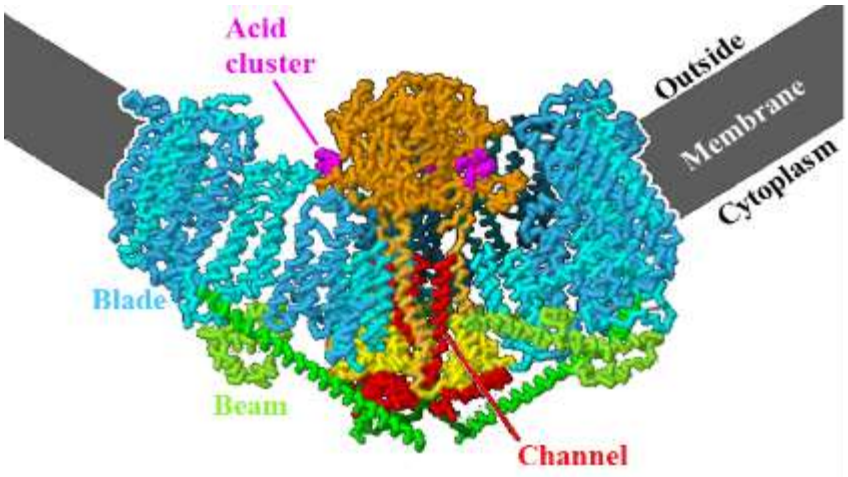

Figure 1.4: *representation of the piezo1 channel located in the cell membrane, with evidence of all subunits*

In my work reported in chapter 3, I performed the experiments using a fluorescently labelled Piezo1 fusion construct, including Piezo1 protein and GFP (Cox et al., 2016), expressed in HEK-293 cells (Cf. Section 1.4.4.).

1.3 Micro-electrode Systems and PDMS mask

For works presented in the chapters 2 and 5, the cells were plated onto commercially MEAs (Fig. 1.5a). In general, MEAs are composed by a two-dimensional arrangement of voltage probes (electrodes) designed to record electrical activity of electrogenic cells; they are also able to generate electrical stimulation. Nowadays, MEA systems represent an essential tool in any electrophysiological lab, thanks to the increase of computational power, which can now handle the amount of data recorded from the electrodes: it is possible to record for hours and perform on line data analysis, or store the data for post experiment analysis. The Micro-electrode arrays from Multi Channel Systems (Reutlingen, Germany) provide microelectrode arrays used in this work. The devices are based on a glass slide, measuring 49x49x1 mm onto which electrodes and tracks are fabricated by surface micromachining techniques. Titanium (Ti), or indium tin oxide (ITO), are selectively deposited via chemical vapor deposition to obtain tracks, electrodes and electrode pads. A subsequent layer of titanium nitrate (TiN) is deposited in the same fashion only on the electrode area to increase the area of contact with the electrolyte. Such coating increasing electrode stability against possible redox reactions, while bettering impedance properties. To provide insulation on all the device, except for the electrode area, a final layer of transparent silicon nitrate (Si3N4) is deposited (approximate thickness 500nm declared from producer). A reference electrode is fabricated outside the array of microelectrode to provide bath reference for extracellular field potentials stable sensing. All the materials are biocompatible, chemically stable in electrolytic environment, and easily coated with ECM proteins to promote cell adhesion. I used two different types of MEA: MEA – 60 chips (Fig. 1.5b) made up of sixty TiN/SiN microelectrodes arranged in an 8x8 square grid (without the four electrodes in the corners) and MEA-4Q (Fig. 1.5c) chips made up of sixty TiN/SiN microelectrodes arranged in a grid 4x13 with a center line 1x7. In both cases, electrodes are 30 μm diameter and 200 μm pitch distance (Fig. 1.5b – 1.5c).

For some experiments (C.f., Chapter 5) a Poly-dimethyl-siloxane (PDMS) mask was used to define two rectangular compartments over the MEA (Fig. 1.5d), interconnected by an array of microchannels (Fig 1.5e). Each compartment has an area of 8 mm^2 (4 mm x 2 mm) and height of about 1 mm. Twenty-five microchannels (5 μm in height, 10 μm in width, 150 μm in length and 50 μm spaced) connect the two compartments. The PDMS mask was obtained using a mixture of PDMS base (Syligard 184) and curing agent at a 10:1 ratio, which was polymerized in an oven at 80°C for 15 min.

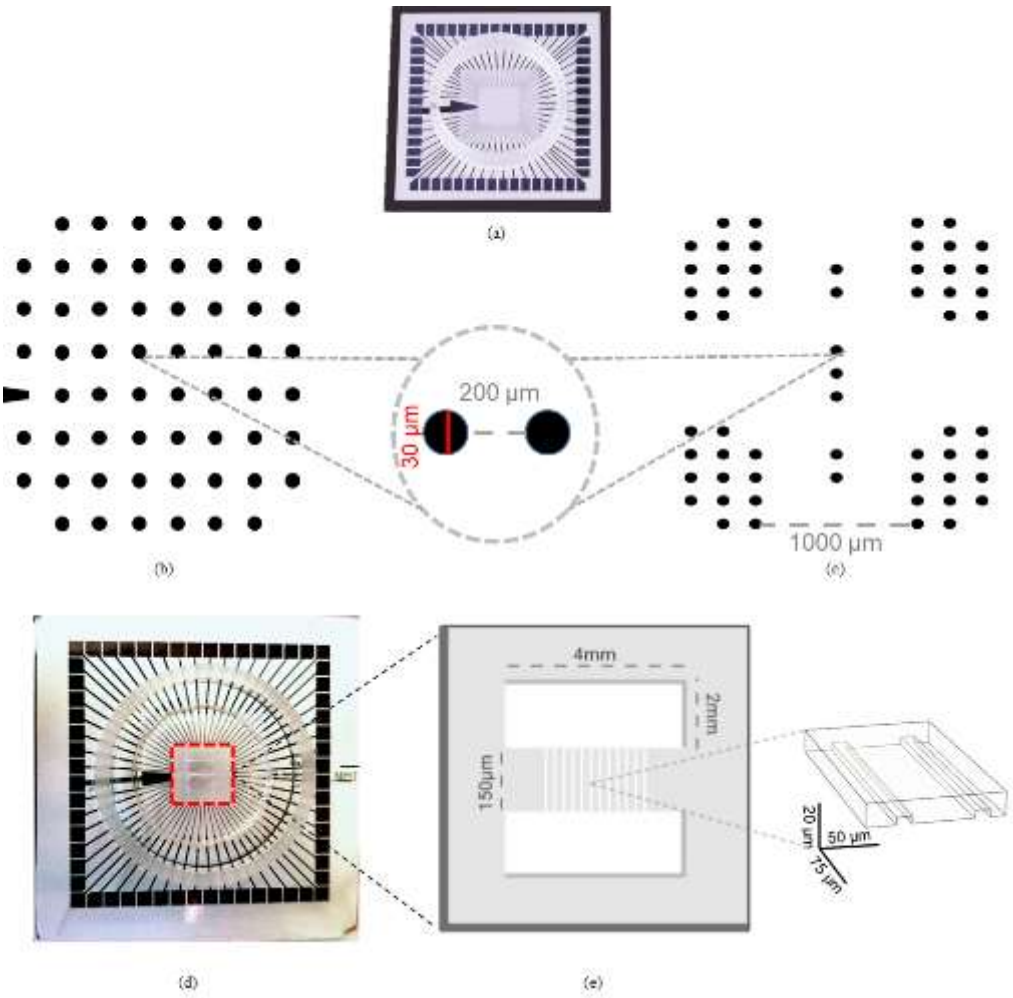

Figure 1.5: *Devices used for the experiments.* **(a)** *MEA chip and sketch of:* **(b)** *layout MEA-60 and* **(c)** *layout MEA-4Q.* **(d)** *PDMS mask (highlighted in red dash-dot) coupled to 60-channels MEA.* **(e)** *Schematic layout of the PDMS mask and cross-section of two representative microchannels: it consists of two compartments interconnected by n = 25 parallel microchannels which allow the communication by means of bundles of neurites.*

The extracellular measurements were recorded using a commercial MEA2100 system (MCS) and acquired with the proprietary software MC_Rack (MCS). Electrophysiological signals were sampled at 10 kHz after 1200x amplification. During the experiments, MEAs were maintained at 37 °C by controlled thermostat (MCS) to reduce the thermal stress of the cells and to reduce evaporation and variations of the pH medium, a constant flow of humidified gas (5% CO_2, 20% O_2, 75% N_2) was provided to the device.

1.4 Cell Cultures

1.4.1. MEA and Petri dish preparation

Cell cultures have been plated according to the work on different devices. In the case of MEA plating, the chips are cleaned carefully the day before dissection and sterilized in the oven (120 °C) for 3 hours. Under aseptic conditions, the active surface of the MEAs is treated with an adhesion polymer: poly-L-Ornithine (PolyO). Precisely, 60 µl of PolyO which is then left to act overnight in the incubator. The next day, just before dissection, I proceed with the removal of the PolyO and with three surface washes of sterile water. At this stage, the MEAs are ready for cell plating.
The technique undergoes adjustments with the application of the PDMS mask to the MEA. The day before the dissection, the mask was positioned and let adhere to the MEA surface. Then, the device (mask + MEA) was sterilized in an oven (120°C for 3 hours) to guarantee the aseptic condition. In order to hydrophilize the microchannels and maintain a hydrophobic contact surface (to prevent possible leakages), an oxygen-plasma treatment (50 s at 120 W) was performed. Therefore, the device was ready for the electrodes surface coating preparation. PolyO (18 µl) was placed inside the delimited area, being careful to keep separate the solutions of the two compartments. Then the procedure is the same described above.
In the case of plating on Petri dishes or glass-bottomed Petri dishes, the process is the same as for plating on a plain MEA, with the only exception that sterilization did not take place in the oven but in 70% ethanol for 3 hours.

1.4.2. 2D neuronal cell cultures

Hippocampal and cortical tissues were removed from rat embryos at gestational day 18 (E18) under sterile conditions (Fig. 1.6A). All procedures were carried out to reduce the number of animals and to minimize their suffering. The experimental protocol was approved by the European Animal Care Legislation (2010/63/EU), by the Italian Ministry of Health in accordance with the D.L. 116/1992 and by the guidelines of the University of Genova (Prot. 75F11.N.6JI, 08/08/18). Firstly, hippocampal and cortical fetal tissues were enzymatically digested in 0.125% Trypsin/Hank's solution containing 0.05% DNAse (Sigma-Aldrich) for 20 min a 37°C. This process was quenched by adding culture medium supplemented with 10% of FBS. Then the tissue was mechanically dissociated with a fire-polished Pasteur pipette. Neurons were suspended in a solution containing Neurobasal Medium (Sigma-Aldrich) with 1% Glutamax (Sigma-Aldrich), 2% B-27 supplemented (Sigma-Aldrich), 1% penicillin-streptomycin (Sigma-Aldrich).
Then cells are plated in tight contact with the MEA (Fig. 1.6B). The plating was performed either onto the area defined by a PDMS mask or without any confinement (Fig. 1.6C). In all cases, cortical and hippocampal cells had a final density of 1500 cells/mm2 and 1300

cells/mm2, respectively. The PDMS mask allow me to perform both homogeneous and heterogeneous cultures. In the first case, both chambers were plated either with cortical or hippocampal cells, while in the heterogeneous configuration one chamber was plated with cortical and the other one with hippocampal neurons. Then, Neurobasal medium was added and the culture was incubated. Cultures were maintained in incubator at 37°C in a 5% CO_2, 95% humidity atmosphere for about 3 weeks by replacing half medium every week. Such a replacement was done using BrainPhysTM (Stemcell Technologies) neuronal medium which better reproduces the central nervous system extracellular environment and increases the proportion of synaptically active neurons (Bardy et al., 2015). This type of medium was supplemented with NeuroCultTM SM1 Neuronal Supplement (Stemcell Technologies).

1.4.3. 3D neuronal cell cultures

To obtain 3D cell cultures, cell dissection is the same as described above. The process is repeated until the first layer has been deposited in contact with the surface of the MEA (Fig. 1.6B – 1.6C). PDMS masks were always used for 3D structures. The 3D assembly was built on top of the first layer using glass microbeads (Thermo Fisher) with 40 µm diameter (certified mean diameter of 42.3 ± 1.1 µm) that were self-assembled onto a Transwell® with a porous membrane (Costar Sigma) to form a monolayer (Fig. 1.6D). In detail, the day before plating, glass microbeads were sterilized by exposure to 70% ethanol for 3 hours, then they were washed with sterile water three times. Sterile microbeads were treated with polyO and left in the incubator overnight at 37°C. The day of the dissection, the adhesion factor solution was removed and the glass microbeads were subjected again to three washes with sterile water. Then, microbeads were suspended in culture medium and were ready to be moved inside Transwell®. For the experiments presented in this work, 33 mm^2 section Transwell® were used. Microbeads were settled on a single layer, where they self-assembled in a hexagonal geometrical structure (Fig. 1.6E), allowing to determine the necessary number of microbeads to cover the Transwell® porous membrane. About 20'000 microbeads were placed onto the Transwell® porous membrane defining a uniform layer. To make the microbead positioning into the Transwell® easier, each membrane was submerged in Neurobasal medium. We placed 100 µl of cells suspension on the microbeads at final concentration about 1'500 cell/µl and 1'300 cell/µl for cortex and hippocampus, respectively. The two main reasons to use a cellular concentration higher than the one used for the first layer (i.e., directly coupled to the electrodes) were: i) about 25% cells were lost when the microbeads were transferred to the MEA; ii) a fraction of cells will never come into contact with the microbeads, falling on the bottom of the Transwell®. The so achieved mixture of cells and microbeads was then incubated for about 6 hours, to ensure proper adhesion among them. The final cortical and hippocampal cell density was about 2'500 and 2'200 cells/mm^2, respectively. Then, several layers of microbeads with cells were placed above the cell monolayer previously plated over the MEA (Fig. 1.6F). Each chamber of the

device contained about 20’000 microbeads coupled to neurons arranged in 4/5 layers of about 4’300 microbeads each. The deposition of the different layers occurred through the removal of the microbeads and cells from the Transwell® and the deposition within the area to be covered, using a pipette (Fig. 1.6G). The layers were created repeating this operation several times and therefore a 3D structure was obtained (Fig. 1.6H). Finally, a large drop of Neurobasal medium was added to guarantee cell survival and the MEA with microbeads coupling with cells were incubated. The protocol for the next few days is the same as defined for 2D cell cultures.

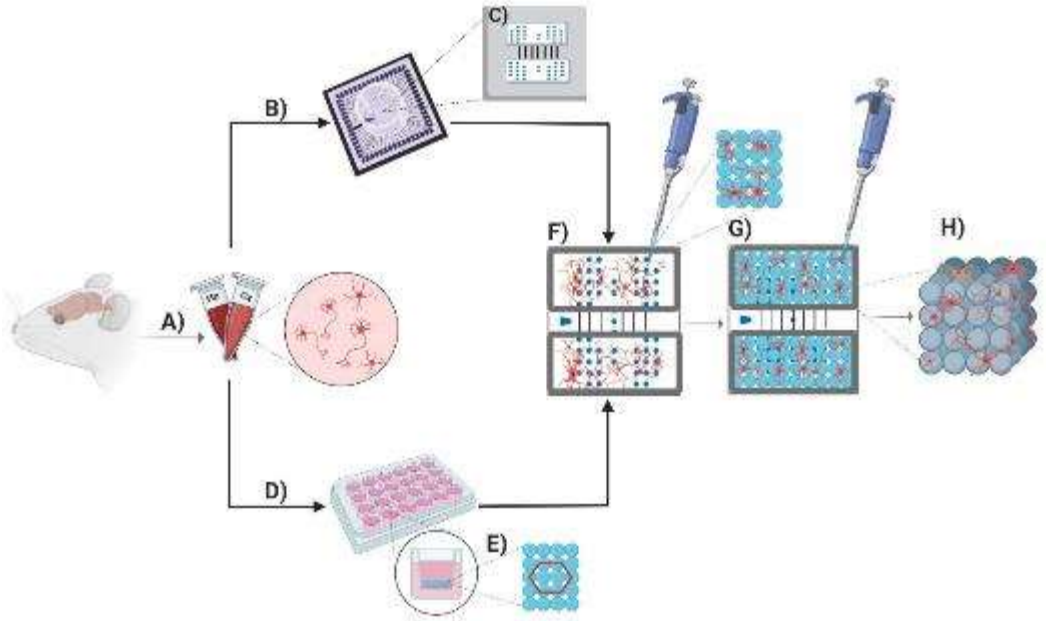

Figure 1.6. *Sketch of the 3D cell culture protocol.* **A)** *Hippocampal and cortical cells are extracted from rat embryos.* **B)** *Once the tissue is dissociated, cells are plated either on the MEA, where the PDMS mask has been previously placed to define the two regions on the recording site area* **(C)**, *or* **(D)** *into the Transwell, where glass microbeads have been previously deposited* **(E).** *To obtain a 3D structure, the suspension of neurons and microbeads is moved from the membrane to the MEA surface to make several layers, using a pipette* **(F-G)**. *As the result of the procedure,* **(H)** *in both compartments of the device, a 3D mixture of microbeads and neurons is created*

1.4.4. HEK-293

The Human Embryonic Kidney 293 (HEK 293) cells were purchased from the American Type Cells Culture (UK). Cells were grown in T-25Flask (Thermo Fisher) with DMEM medium (Sigma-Aldrich), supplemented with 10% fetal calf serum (Sigma-Aldrich), 2 mM L-glutamine (Sigma-Aldrich), 100 U/ml penicillin (Sigma-Aldrich), 100 µg/ml streptomycin and maintained at 37 °C in a 5% CO2 / 95% air atmosphere. Two days before the experiment, the culture medium was removed from the flasks and 5 ml of phosphate buffer saline (PBS, Sigma-Aldrich) were added. After one minute, 1 ml Trypsin was added, and the flask was incubated for two minutes to enable the cells to detach from the flask's bottom. The Trypsin is then blocked adding the culture medium containing the FBS. At this point, the cell suspension was transferred in 15 ml falcon tube and centrifuged (1000 rpm for 3 min.). The supernatant was aspirated, the cells were resuspended in 3 ml of culture medium, counted with the Thoma chamber and plated in Petri Dishes at the final density of

10x103 cell/petri. The day after cells were transfected with 400 ng of c PIEZO1-GFP plasmid construct (C.f., Section 1.2.2.), using the Effectene Kit from Qiagen and according to manufacturer instructions.
Next day cells were transferred following the procedure above described into glass-bottomed Petri dishes (35 mm diameter Petri, 10 mm diameter glass previously treated with the protocol described in section 1.4.1) to improve cell adhesion. Transfected cells expressing fluorescent PIEZO1 channels on their plasma membranes were used for calcium imaging experiments.

1.4.5. MCF-7

The human breast adenocarcinoma MCF-7 cells were purchased from the Interlab Cell Line Collection (ICLC) cell bank (San Martino Polyclinic Hospital Genova, Italy). MCF-7 cells were cultured in in Dulbecco's Modified Eagle's Medium (ThermoFischer) supplemented with 10% (v/v) fetal bovine serum (ThermoFischer), 1% antibiotics (diluted from a stock solution containing 5000 U/ml Penicillin, 5000 mg/ml Streptomycin) and 2 mM glutamine (ThermoFischer). They are maintained in incubator with a humidified atmosphere, 5% (v/v) CO2, and at 37 °C. When reaching more than 80% confluence, the cells were detached by using 0.25% Trypsin (ThermoFischer), plated onto Petri dishes (35 mm diameter) with a cell density of $1.6x10^6$ cells/petri and incubated for 24h.

1.4.6. Cell viability test

To estimate the cell viability, the MCF-7 cells line were subjected to the MTT assay. The MTT assay is a colorimetric assay for measuring cell metabolic activity and proliferation which relies on the reduction of MTT, a yellow water-soluble tetrazolium dye, to purple-colored formazan crystals, mainly by mitochondrial dehydrogenases. The formazan product is dissolved in isopropyl-alcohol, producing a colored solution and giving an estimation of the level of cytotoxicity, which was then quantified using spectrophotometry (565 nm wavelength). According to a linear relationship between cell activity and absorbance, the amount of color emitted is directly proportional to the number of viable cells. To be specific, 5 mg di MTT was dissolved in 1 ml of PBS. The solution was diluted (1:10) in a FBS and culture medium without phenol red, forming the *MTT solution*. At this stage, the cells were taken from the incubator and their culture medium was removed in order to add 2 ml of the *MTT solution* for each culture. Such, the cultures were incubated for 3.5 h. Following that, the *MTT solution* was removed, and 2ml of isopropyl-alcohol were added to each Petri dish and allowed to work for 20 min in the incubator. Finally, the isopropyl-alcohol in the Petri dish was measured using the Agilent technologies Cary 60 UV-Vis spectrophotometer. The following formula is then used to measure cell viability (%CV):

$$CV\% = \frac{abs_{sample}}{abs_{control}} * 100 \quad (1.8)$$

Where abs_{sample} was the absorbance of the sample culture, and $abs_{control}$ was the absorbance of the control cultures, i.e. a cultures which was not handled.

1.5. Calcium Imaging

1.5.1. Calcium imaging setup

The inverted microscope iMIC (Till Photonics. GmbH) was used for the calcium imaging experiments. The manufacturer's software program controls all of the microscope's motorized components. The acquisitions were done on a single channel, with a fluorescence exposure time of 50ms and an LED exposure time of 5ms, and frames obtained at a period of 150ms. The calcium imaging experiments were performed in combination with sound stimulation, as described in Chapter 3, so the microscope was combined with the *PA* transducer setup (C.f., Section 1.1.2.). The two setups are interconnected via a LabView acquisition board NI-USB-6259 (National Instruments, Austin, TX), as seen in fig 1.7, which allows for simultaneous control of the US stimulus and the camera shutter via a designed specifically LabView program. In this way, the temporal information of the sound stimulus was preserved with respect to the click of the frame.

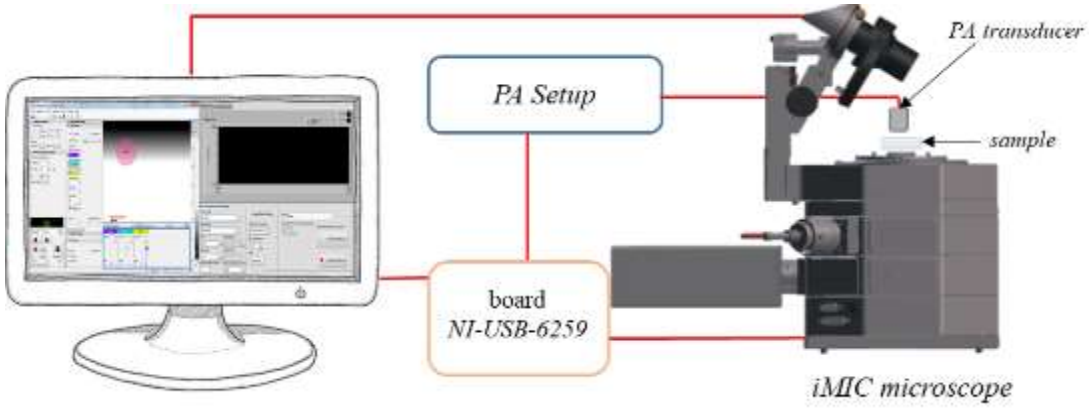

Figure 1.7: *Sketch of the calcium imaging set up, from left to right: computer for interface image acquisition program and LabView program, LabView NI-USB-6259 board for US signal control and synchronization with the camera frame acquisition signal, PA setup for the emission of ultrasound, and iMIC microscope for image acquisition.*

1.5.2. Fluo-4

Fluo-4 AM (Thermo Fisher) was used to measure the calcium concentration during the calcium imaging experiments. This labeled calcium indicators is excited by the 488 nm line of the laser and emitted at 520 nm wavelength. The Fluo-4 stock solution was mixed with 9 µl of DMSO (1-5µM) and then with an equal volume of 20% (w/v) Pluronic in DMSO, making the final Pluronic concentration about 0.02%. The addition of the non-ionic detergent, Pluronic, can assist in the dispersion of the nonpolar AM ester in aqueous media. On the experiments day, the cells were incubated with 1 µl of AM ester for 20 minutes at 37°C. In details, the Fluo-4 was added directly into the cell medium. It is worth notice that time and temperature were determined empirically; I decided to use the minimum dye concentration required to yield fluorescence signals with an adequate signal to noise. Before fluorescence measurements, cells were washed in an indicator-free medium to remove any dye that is nonspecifically associated with the cell surface.

1.6. Drug Delivery

1.6.1. Layer by layer technique

The Layer by Layer (LbL) method allows the fabrication of multilayer thin film assembled on solid supports by the spontaneous sequential adsorption of oppositely charged species from aqueous solutions onto charged substrates (Sukhorukov et al., 1998). Nowadays one of its main application is the creation of hollow capsules or vesicles, using colloidal micro and nanoparticles as a template with a wide range of substances to construct multilayers (Hammond, 2012). This application allows encapsulation or incorporation into the layers of different substances, like medicines as a means of drug delivery. When the desired thickness is obtained, the particles can be used in the core-shell state, or the core can be dissolved to leave hollow polymeric capsules (Becker et al., 2010).

To asses an innovative drug delivery technique (C.f., Chapter 4), I used the LbL polymeric capsules obtained with a template of calcium carbonate ($CaCo_3$) and both synthetic and bio-polymers for the layer (Fig. 1.8a). The process of preparation of CaCO3 microparticles, with a diameter of about 4-5 µm, started introducing rapidly sodium carbonate (Na_2CO_3, Sigma-Aldrich) 0.33 M solution (1 ml) to calcium chloride dehydrate ($CaCl_2$, Sigma-Aldrich) 0.33M solution (1 ml) (Fig. 1.8a), using a 10 ml becker and a magnetic bar (1 cm long, 0.5 cm wide). The solution was immediately stir for 20 seconds at 900 rpm, then was divided into two 1 ml Eppendorf tubes which were centrifuged at 200 *rcf* for 2 minutes. Second, the supernatant was removed, being careful not to remove the pellet, by adding 1 ml of Milli-Q water, vortexed for a few seconds, and still centrifuged. Three washes were done (Fig. 1.8a). Until starting with the polymers, an optical microscope was used to ensure that the CaCO3 cores were circular, with the proper diameter, and particle matter free. Then, 1 ml of a polymer has to be added, starting from the negative one. The solution was suspended with the vortex for 10-15 minutes and then was centrifuged at 200 rcf for 2 minutes (Fig. 1.8a). Such as for the cores, it is necessary to repeat the washing process with Milli-Q water for three times. Later, the positive polymer was added, repeating the same procedure. The positive and negative polyelectrolyte were altered to obtain 8 layers. In detail for synthetic microcapsules I used sodium polystyrene sulfonate (PSS, Sigma-Aldrich) as negative polymer, and poly-allylamine hydrochloride (PAH, Sigma-Aldrich) as a positive polymer (Fig. 1.8b). Indeed, as a bio-polymers I used dextran sulfate sodium salt (DEX, Sigma-Aldrich) and poly-L-arginine hydrochloride (PLA, Sigma-Aldrich) (Fig. 1.8b). Once finished all eight layers, 1 ml of ethylenediaminetetraacetic acid (EDTA, Sigma-Aldrich) 0.2 M at pH 5 was added, to decompose the internal CaCO3 core (Fig. 1.8c), used as templates, and to obtain the final microcapsules. The solutions was suspended for 5 min, and was centrifuged at 1350 *rcf* for 2 minutes alternating it with Milli-Q water wash for three times.

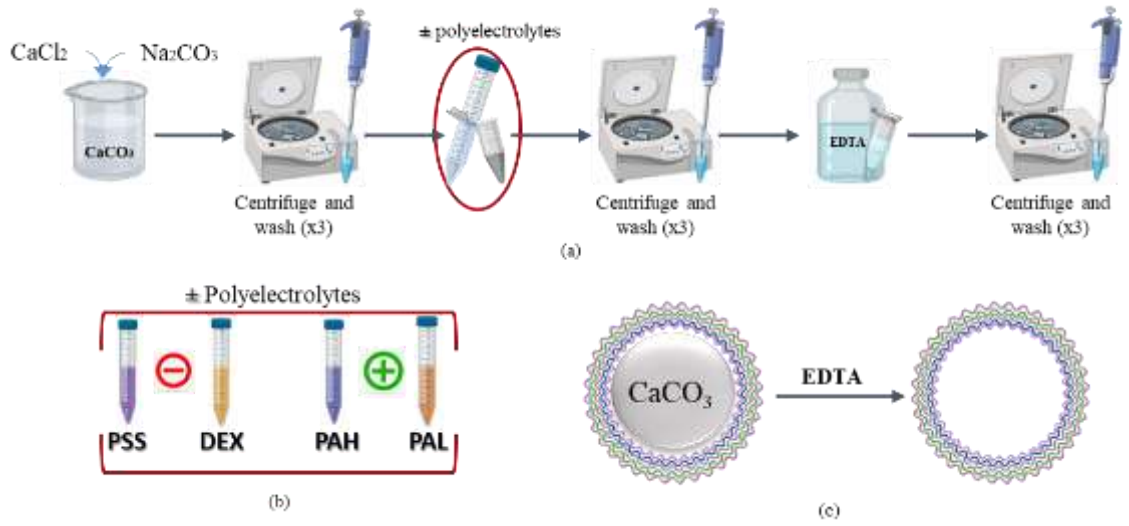

Figure 1.8: **(a)** *Schematic of the polyelectrolyte microcapsules fabrication by the layer-by-layer assembly (LbL).* **(b)** *Polyelectrolytes used in the manufacturing of microcapsules: PSS as a negative polyelectrolyte and PAH as a positive polyelectrolyte for synthetic microcapsules, while DEX and PAL as negative and positive polyelectrolytes for bio-microcapsules.* **(c)** *The EDTA addition dissolved the core (CaCo3) of the microcapsules, obtaining hollow microcapsules.*

For visualization, the shell of the microcapsules was labeled by depositing as seventh layer Dextran – Fitch (DEX, Sigma-Aldrich), while the core was labeled with a FluoSpheres™. These nanoparticles (20 µl) were co-precipitated with $CaCl_2$ 0.33 M solution (1ml), and then Na_2CO_3 0.33 M solution (1 ml) was added. In this way, I obtained $CaCO_3$ core visible in red fluorescence. The microcapsules were then produced as described above.

1.6.2. Drugs encapsulations strategies

To study drug delivery strategies, doxorubicin hydrochloride (DOX) was used as model drug. DOX was added to Na_2CO_3 0.66M solution at the final concentration of 0.25 mg/ml. Then it was rapidly co-precipitated with the same quantity of $CaCl_2$ 0.33M and the microcapsules were created with the technique described in section 1.6.1. To evaluate the quantity of doxorubicin encapsulated inside the microcapsules, the supernatants derived from all washes both of cores, polymeric layers and EDTA were kept apart. All these solutions were centrifuged at 4500 rpm for 2 minutes, to avoid having some remaining solid particles. Secondly, the solutions were analyzed using the Agilent technologies Cary 60 UV-Vis spectrophotometer at the wavelength of 481 nm with a DOX calibration curve in Milli-Q water. The calibration curve is a general method for determining the concentration of a substance in an unknown sample by comparing to a set of standard samples of known concentration. Its principle is based on the Beer-Lambert law, which states that there is a linear relationship between the concentration and the absorbance of the solution, and this enables the concentration of a solution to be calculated by measuring its absorbance (Abs). The calibration curve of DOX was:

$$Abs = 23.44279x + 0.01093 \quad (1.9)$$

Where *Abs* denotes absorbance and *x* denotes the concentration of DOX. As a result, the absorbance of the solvent produced by washes can be used to calculate its DOX concentration of the DOX. Since this DOX concentration was the amount of DOX released during the LbL steps (DOX_{free}), the efficiency of encapsulation was calculated as follows:

$$EE\% = \frac{DOX\_tot - DOX_{free}}{DOX\_tot} * 100 \quad (1.10)$$

where DOX_{tot} was the amount of initial doxorubicin. Also, the percentage of DOX released from the microcapsules was also evaluated from a control sample, as follows:

$$RD\% = \frac{DOX_{released}}{DOX_{encapsulated}} * 100 \quad (1.11)$$

References

Abbott, J. G. (1999). Rationale and derivation of Mi and Ti - A review. *Ultrasound in Medicine and Biology*, *25*(3), 431–441. https://doi.org/10.1016/S0301-5629(98)00172-0

Ahmad, N., Bygrave, M., Chhem, R., Hoffman, L., Welch, I., Grange, R., Fenster, A., Hill, D., & Lee, T. Y. (2009). High-frequency ultrasound to grade disease progression in murine models of Duchenne muscular dystrophy. *Journal of Ultrasound in Medicine*, *28*(6), 707–716. https://doi.org/10.7863/jum.2009.28.6.707

American Institute of Ultrasound in Medicine/National Electrical Manufacturers Association. Standard for Real-Time Display of Thermal and Mechanical Acoustic Output Indicies on Diagnostic Ultrasound Equipment. Washington, DC: National Electrical Manufactu. (1992).

Apfel, R. E., & Holland, C. K. (1991). Gauging the likelihood of cavitation from short-pulse, low-duty cycle diagnostic ultrasound. *Ultrasound in Medicine and Biology*, *17*(2), 179–185. https://doi.org/10.1016/0301-5629(91)90125-G

Bagchi, A., Meka, S. R. K., Rao, B. N., & Chatterjee, K. (2014). Perovskite ceramic nanoparticles in polymer composites for augmenting bone tissue regeneration. *Nanotechnology*, *25*(48), 485101. https://doi.org/10.1088/0957-4484/25/48/485101

Bardy, C., Van Den Hurk, M., Eames, T., Marchand, C., Hernandez, R. V., Kellogg, M., Gorris, M., Galet, B., Palomares, V., Brown, J., Bang, A. G., Mertens, J., Böhnke, L., Boyer, L., Simon, S., & Gage, F. H. (2015). Neuronal medium that supports basic synaptic functions and activity of human neurons in vitro. *Proceedings of the National Academy of Sciences of the United States of America*, *112*(20), E2725–E2734. https://doi.org/10.1073/pnas.1504393112

Becker, A. L., Johnston, A. P. R., & Caruso, F. (2010). Layer-By-Layer-Assembled Capsules and Films for Therapeutic Delivery. *Small*, *6*(17), n/a-n/a. https://doi.org/10.1002/smll.201000379

Berlincourt, D., & Jaffe, H. (1958). Elastic and Piezoelectric Coefficients of Single-Crystal Barium Titanate. *Physical Review*, *111*(1), 143–148. https://doi.org/10.1103/PhysRev.111.143

Ciofani, G., Danti, S., D'Alessandro, D., Ricotti, L., Moscato, S., Bertoni, G., Falqui, A., Berrettini, S., Petrini, M., Mattoli, V., & Menciassi, A. (2010). Enhancement of neurite outgrowth in neuronal-like cells following boron nitride nanotube-mediated stimulation. *ACS Nano*, *4*(10), 6267–6277. https://doi.org/10.1021/nn101985a

Coste, B., Mathur, J., Schmidt, M., Earley, T. J., Ranade, S., Petrus, M. J., Dubin, A. E., & Patapoutian, A. (2010). Piezo1 and Piezo2 are essential components of distinct mechanically activated cation channels. *Science*, *330*(6000), 55–60. https://doi.org/10.1126/science.1193270

Cox, C. D., Bae, C., Ziegler, L., Hartley, S., Nikolova-Krstevski, V., Rohde, P. R., Ng, C. A., Sachs, F., Gottlieb, P. A., & Martinac, B. (2016). Removal of the mechanoprotective influence of the cytoskeleton reveals PIEZO1 is gated by bilayer tension. *Nature Communications*, *7*(1), 1–13. https://doi.org/10.1038/ncomms10366

Dalecki, D. (2004). Mechanical bioeffects of ultrasound. In *Annual Review of Biomedical Engineering* (Vol. 6, pp. 229–248). Annu Rev Biomed Eng. https://doi.org/10.1146/annurev.bioeng.6.040803.140126

Dubey, A. K., Thrivikraman, G., & Basu, B. (2015). Absence of systemic toxicity in mouse model towards BaTiO3 nanoparticulate based eluate treatment. *Journal of Materials Science: Materials in Medicine*, *26*(2), 1–11. https://doi.org/10.1007/s10856-015-5414-6

Duck, F. A. (2007). Medical and non-medical protection standards for ultrasound and infrasound. In *Progress in Biophysics and Molecular Biology* (Vol. 93, Issues 1–3, pp. 176–191). Pergamon. https://doi.org/10.1016/j.pbiomolbio.2006.07.008

Franzini, A., Moosa, S., Prada, F., & Elias, W. J. (2020). Ultrasound Ablation in Neurosurgery: Current Clinical Applications and Future Perspectives. In *Neurosurgery* (Vol. 87, Issue 1, pp. 1–10). Oxford University Press. https://doi.org/10.1093/neuros/nyz407

Ge, J., Li, W., Zhao, Q., Li, N., Chen, M., Zhi, P., Li, R., Gao, N., Xiao, B., & Yang, M. (2015). Architecture of the mammalian mechanosensitive Piezo1 channel. *Nature*, *527*(7576), 64–69. https://doi.org/10.1038/nature15247

Guo, Y. R., & MacKinnon, R. (2017). Structure-based membrane dome mechanism for piezo mechanosensitivity. *ELife*, *6*. https://doi.org/10.7554/eLife.33660

Haar, T. (1988). Biological effects of ultrasound in clinical applications. *Ultrasound : Its Chemical, Physical, and Biological Effects*, 305–320. https://ci.nii.ac.jp/naid/10029286645

Hammond, P. T. (2012). Building biomedical materials layer-by-layer. In *Materials Today* (Vol. 15, Issue 5, pp. 196–206). Elsevier. https://doi.org/10.1016/S1369-7021(12)70090-1

HARVEY, E. N., HARVEY, E. B., & LOOMIS, A. L. (1928). FURTHER OBSERVATIONS ON THE EFFECT OF HIGH FREQUENCY SOUND WAVES ON LIVING MATTER. *The Biological Bulletin*, *55*(6), 459–469. https://doi.org/10.2307/1536801

Humphrey, V. F. (2007). Ultrasound and matter-Physical interactions. In *Progress in Biophysics and Molecular Biology* (Vol. 93, Issues 1–3, pp. 195–211). Pergamon. https://doi.org/10.1016/j.pbiomolbio.2006.07.024

IEC 62359: Ultrasonics – Field characterization – Test methods for the determination of thermal and mechanical indices related to medical diagnostic ultrasonic fields; International Standard IEC 62359 Ed.2.0, Geneva 2010-10. (n.d.).

Khraiche, M. L., Phillips, W. B., Jackson, N., & Muthuswamy, J. (2008). Ultrasound induced increase in excitability of single neurons. *Proceedings of the 30th Annual International Conference of the IEEE Engineering in Medicine and Biology Society, EMBS'08 - "Personalized Healthcare through Technology,"* 4246–4249. https://doi.org/10.1109/iembs.2008.4650147

Marino, A., Arai, S., Hou, Y., Sinibaldi, E., Pellegrino, M., Chang, Y. T., Mazzolai, B., Mattoli, V., Suzuki, M., & Ciofani, G. (2015). Piezoelectric Nanoparticle-Assisted Wireless Neuronal Stimulation. *ACS Nano*, *9*(7), 7678–7689. https://doi.org/10.1021/acsnano.5b03162

Miller, M. W., Miller, D. L., & Brayman, A. A. (1996). A review of in vitro bioeffects of inertial ultrasonic cavitation from a mechanistic perspective. In *Ultrasound in Medicine and Biology* (Vol. 22, Issue 9, pp. 1131–1154). Elsevier Science Ltd. https://doi.org/10.1016/S0301-5629(96)00089-0

Moroni, M., Servin-Vences, M. R., Fleischer, R., Sánchez-Carranza, O., & Lewin, G. R. (2018). Voltage gating of mechanosensitive PIEZO channels. *Nature Communications*, *9*(1), 1–15. https://doi.org/10.1038/s41467-018-03502-7

O'Brien, W. D. (2007). Ultrasound-biophysics mechanisms. In *Progress in Biophysics and Molecular Biology* (Vol. 93, Issues 1–3, pp. 212–255). NIH Public Access. https://doi.org/10.1016/j.pbiomolbio.2006.07.010

Pantazis, P., Maloney, J., Wu, D., & Fraser, S. E. (n.d.). *Second harmonic generating (SHG) nanoprobes for in vivo imaging*. https://doi.org/10.1073/pnas.1004748107/-/DCSupplemental

Park, J. B., Kelly, B. J., Kenner, G. H., von Recum, A. F., Grether, M. F., & Coffeen, W. W. (1981). Piezoelectric ceramic implants: in vivo results. *Journal of Biomedical Materials Research*, *15*(1), 103–110. https://doi.org/10.1002/jbm.820150114

Rojas, C., Tedesco, M., Massobrio, P., Marino, A., Ciofani, G., Martinoia, S., & Raiteri, R. (2018). Acoustic stimulation can induce a selective neural network response mediated by piezoelectric nanoparticles. *Journal of Neural Engineering*, *15*(3), 036016. https://doi.org/10.1088/1741-2552/aaa140

Shin, H. C., Prager, R., Gomersall, H., Kingsbury, N., Treece, G., & Gee, A. (2010). Estimation of Average Speed of Sound Using Deconvolution of Medical Ultrasound Data. *Ultrasound in Medicine and Biology*, *36*(4), 623–636. https://doi.org/10.1016/j.ultrasmedbio.2010.01.011

Sukhorukov, G. B., Donath, E., Lichtenfeld, H., Knippel, E., Knippel, M., Budde, A., & Möhwald, H. (1998). Layer-by-layer self assembly of polyelectrolytes on colloidal particles. *Colloids and Surfaces A: Physicochemical and Engineering Aspects*, *137*(1–3), 253–266. https://doi.org/10.1016/S0927-7757(98)00213-1

Tufail, Y., Matyushov, A., Baldwin, N., Tauchmann, M. L., Georges, J., Yoshihiro, A., Tillery, S. I. H., & Tyler, W. J. (2010). Transcranial Pulsed Ultrasound Stimulates Intact Brain Circuits. *Neuron*, *66*(5), 681–694. https://doi.org/10.1016/j.neuron.2010.05.008

Tyler, W. J., Tufail, Y., Finsterwald, M., Tauchmann, M. L., Olson, E. J., & Majestic, C. (2008). Remote excitation of neuronal circuits using low-intensity, low-frequency ultrasound. *PLoS ONE*, *3*(10). https://doi.org/10.1371/journal.pone.0003511

Vijatović, M. M., Bobić, J. D., & Stojanović, B. D. (2008). History and Challenges of Barium Titanate: Part I. *Science of Sintering*, *40*, 155–165. https://doi.org/10.2298/SOS0802155V

Wada, S., & Tsurumi, T. (2004). Enhanced piezoelectricity of barium titanate single crystals with engineered domain configuration. *British Ceramic Transactions*, *103*(2), 93–96. https://doi.org/10.1179/096797804225012747

Wang, X., Pang, Y., Ku, G., Xie, X., Stoica, G., & Wang, L. V. (2003). Noninvasive laser-induced photoacoustic tomography for structural and functional in vivo imaging of the brain. *Nature Biotechnology*, *21*(7), 803–806. https://doi.org/10.1038/nbt839

Zhao, Q., Zhou, H., Chi, S., Wang, Y., Wang, J., Geng, J., Wu, K., Liu, W., Zhang, T., Dong, M. Q., Wang, J., Li, X., & Xiao, B. (2018). Structure and mechanogating mechanism of the Piezo1 channel. *Nature*, *554*(7693), 487–492. https://doi.org/10.1038/nature25743

Chapter 2

Ultrasound neuromodulation mediated by BTNPs

2.1 Abstract

Nowadays, the most commonly employed neuromodulation approaches either require invasive procedures (such as surgical implantation of electrodes or photon-emitting devices), or lack sensitivity and selectivity being based on electromagnetic fields. One of the challenges in the field of neuroscience is to identify new stimulation strategies, which balance efficacy with invasiveness. A promising family of non-invasive neuromodulation approaches exploits ultrasound (US), which can be focused to reach deep brain regions through the skull. In this work, we investigate the in vitro electrophysiological response of cortical networks, treated with piezoelectric barium titanate nanoparticles (BTNPs), to US pulses. We observed that US causes a reproducible and reversible inhibition of the network activity. Without BTNPs, the US stimulus does not affect the spontaneous electrical activity of the network.

2.2 Experimental Protocol and details

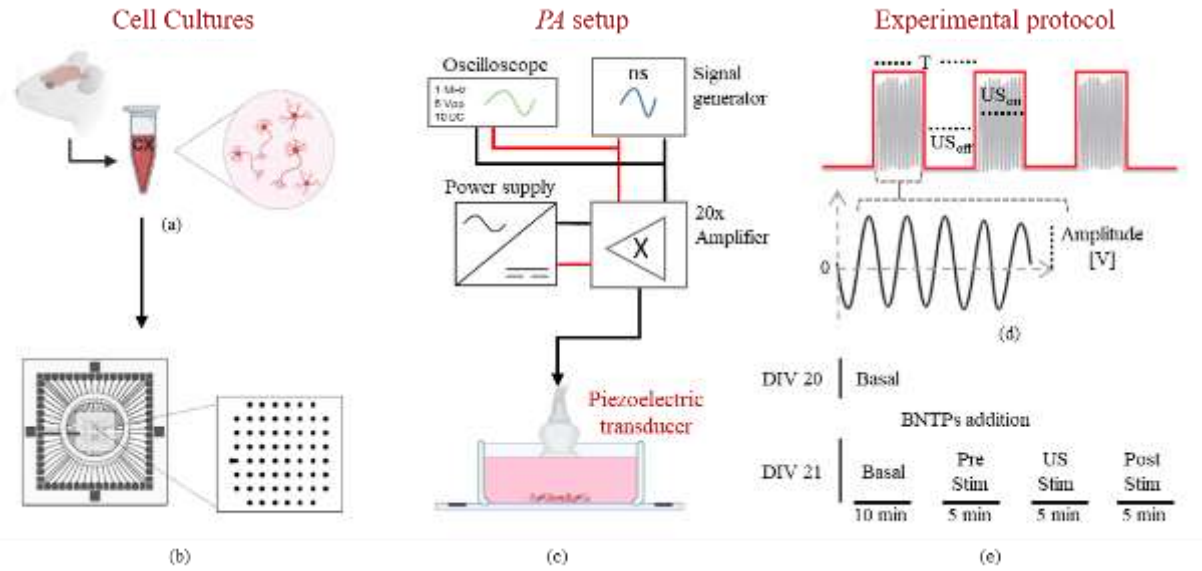

Figure 2.1: *Sketch material and methods. Cortical cells from cortical rat embryos* **(a)** *were plated into 60-channels MEA* **(b)**. *The piezoelectric transducer is placed inside the MEA and guided by a home-made set up* **(c)**. *The ultrasound were emitted as a pulsed wave* **(d)**. *Description of the experimental protocol performed at 20 and 21 days in vitro* **(e)**.

2.2.1 Ultrasound stimulation

Pulsed-wave ultrasound at 1MHz and variable intensity (from 0.7 W/cm^2 to 5 W/cm^2) was applied to cortical cultures using *PA transducer* (fig.2.1c, C.f., Chapter 1 | 1.1.2). Ultrasound was applied as a train of pulses (Fig 2.1d) with a period T=4s and 10% of duty cycle (DC, fraction of active signal). The wave amplitude of driving signal (*DS*) spanned from 20V to 70V, which correspond to the pressure field range from 0.1 MPa to 0.28MPa, respectively. Moreover, digital signal that identified the on and the off phases of US stimulation was recorder.

2.2.2 Experimental protocol

Cortical cells were plated into commercial MEA-60 hips (Fig. 2.1a-b, C.f., Chapter 1 | 1.3 and 1.4.2). In this work, piezoelectric non-centrosymmetric barium titanate nanoparticles, whose details are reported in Chapter 1 | 1.2.1, were employed. The evening before the experiment (DIV 20), the nanoparticle was dispersed in cell cultures at a final concentration of 50 μg/ml. Finally, cultures were incubated overnight to allow the deposition of the nanoparticles. To evaluate whether the interaction cell-BTNPs affected the spontaneous activity of the network, 10 min of spontaneous cortical activity was recorded before the BTNPs addition (fig. 2.1e). After overnight deposition of BTNPs, 15 min of spontaneous electrophysiological activity was recorded (10 min as a basal control for the BTNPs effects and 5 min as a pre-stimulus). Then US stimulation began and 45 US pulses were delivered in a 3 min time window. After the stimulation, 5 min of spontaneous activity was recorded as post-stimulus (fig. 2.1e). To check whether the networks were responsive to external stimuli, electrical pulses were delivered by randomly chosen MEA electrodes at the end of

each experiment. Bi-phasic (positive first) electrical stimulation was delivered for three minutes at an amplitude of ±1500 mV at the same frequency as US stimulation. This experimental protocol was used for n = 40 cortical cultures derived from five preparations. For each US amplitude, I recorded n = 4 cultures with and without BTNPs (negative controls).

2.2.3 Analysis

The analysis were performed in Matlab (The Mathworks, Natik, US) and all the details were reported in Appendix A. Statistical analysis was performed using Origin (Origin Lab Northampton, Ma). I performed a non-parametric Kruskall-Wallis test and significance levels were set at $p < 0.05$. The box plots representation indicates the *percentile 25-75* (box), the *standard deviation* (whiskers), the mean (*square*), and the median (*line*) values. Asterisks above the plots indicate statistically significant differences ($0.01 < p < 0.05$: *; $0.001 < p < 0.009$: **; $p < 0.001$: ***).

2.2.4 Immunocytochemistry images

Cultures were fixed using 4% paraformaldehyde in phosphate buffer (PBS) for 20 min at room temperature. Repeated washings with PBS to remove the fixative was done as post-fixation step, followed by a permeabilization step with Triton X-100 0.2% (8 min); finally, the cultures were exposed to a blocking buffer solution (PBS with 2% BSA bovine serum albumin, 0.5% FBS). Antibodies raised against the specific markers NeuN and Map-2 were used and visualized by the Alexa Fluor 549- Gam (goat anti-mouse IgG) and Alexa Fluor 488-Gar (goat anti-rabbit IgG) secondary antibodies (Thermo Fisher Scientific, Waltham, MA) in order to locate neuronal soma and dendrites, respectively.

2.3 Results

I measured the effects of ultrasound on cortical cells using the setup described in Material and methods. Throughout the performed experiments, US were applied at 1MHz as a pulsed wave with 4s T at 10% DC. I first tested different US intensities to permit quantitative investigation of the effect-intensity dependence. Moreover, I worked with pulsed wave to avoid unwanted thermal effects due to the US stimulation (Tyler, 2011). With these US parameters and the experimental protocol depicted in Fig. 2.1e, I found that US stimulation induced a robust, reproducible and reliable inhibition of cortical spontaneous electrophysiological activity. In addition, I also established that the response to US is highly reversible. In the next sections, after a brief description of the US characterization results, I presented the effect of the stimulation via the acoustic-electric transduction provided by the BTNPs on the cortical cells, using two groups of experiments. First, cultures of cortical neurons treated with BTNPs (50 μg/ml); second, control cultures of cortical neurons without nanoparticles.

2.3.1 Ultrasound characterization

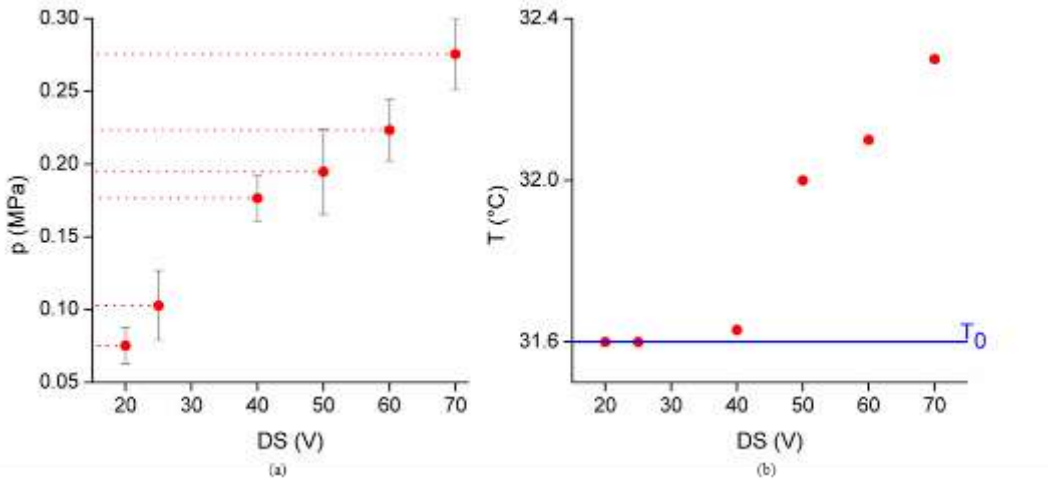

Figure 2.2: **(a)** *Calculated sound pressure field as a function of US driving signal (DS).* **(b)** *Temperature increase of the solution in function of DS. (Blue line indicates the initial temperature of the solution* T_0*)*

In order to assess that the US complied with the limits of the mechanical index (MI) and thermal index (TI) and could therefore be defined as safe for cells (IEC 62359), the pressure field emitted by US transducer has been characterized using a miniaturized hydrophone, temperature sensor and a MEA filled with Neurobasal medium (C.f., Chapter 1 | 1.1.3). The transducer was controlled by a high voltage driving signal (DS) from 20V to 70V. The resulting sound pressure field spans from 0.1 MPa to 0.28 MPa (Fig. 2.a); due to the properties of the sound wave, the MI assumes the same values as the sound pressure field. In all cases, MI stays below 0.3, which is the widely and accepted threshold value to fully prevent cavitation effects (C.f., Chapter 1 | 1.1.1.). To assess temperature changes, MEA filled with Neurobasal medium was exposed by 3min of US stimulation with 10% of the

duty cycle. To replicate the experimental temperature conditions, the MEA was placed on the Multi-Channel Systems MEA2100 headstage, keeping the temperature at 37°C with a thermostat. I observed that the increase of temperature was about 0.6 °C up to 70V (Fig. 2.2b). The temperature rise is less than one; so, keeping in mind that TI is implied by the ratio of ultrasound power to those that induce a temperature rise of one degree in the tissue (Cf., Chapter 1 | 1.1.1.), and that the FDA set the safe threshold at 6, I may assume that my system is a safe system.

2.3.2 Ultrasound with BTNPs

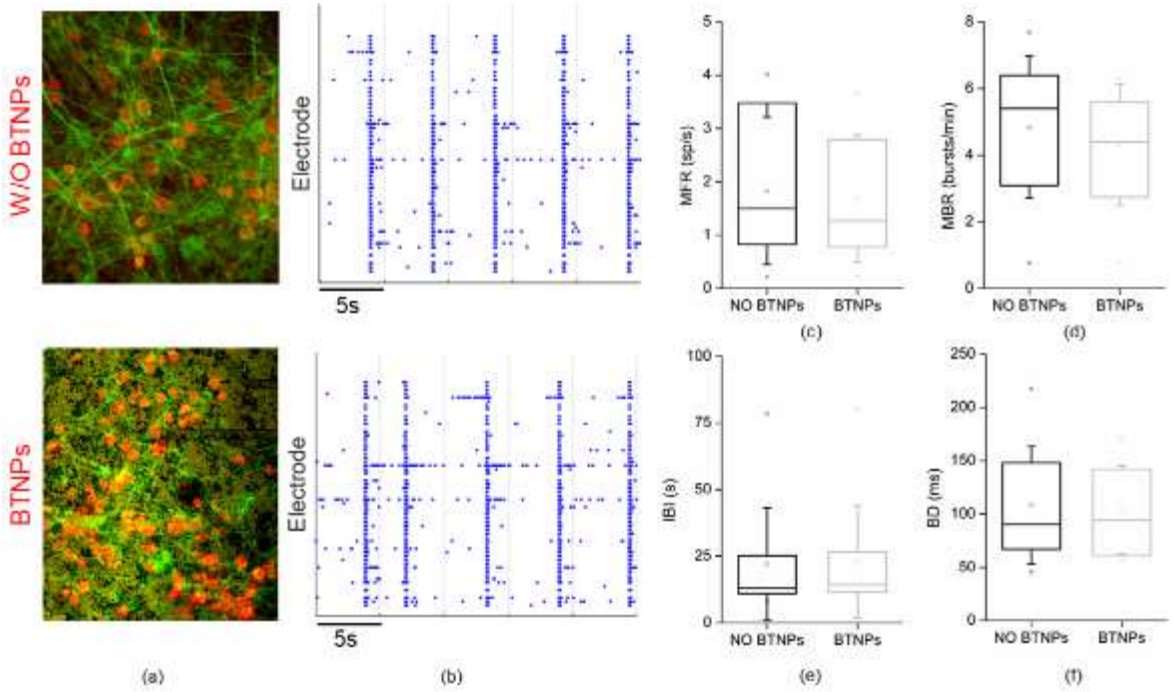

Figure 2.3: **(a)** *Neuronal network image of mature cortical culture (21DIV) without (W/O BTNPs, top) and with (BTNPs, bottom) BTNPs: the fluorescent image (green: MAP2, red: NeuN) is superimposed on the DIC image of the same area (dark dust: BTNPs, dark circle: MEA electrode.* **(b)** *Representative raster plots of the spontaneous activity of a neuronal network before (W/O BTNPs) and after (BTNPs) the piezonanoparticles addition. Spiking and bursting activity characterization of culture before (W/O BTNPs) and after (BTNPs) the piezonanoparticles delivery:* **(c)** *mean firing rate (MFR);* **(d)** *mean burst rate (MBR);* **(e)** *inter bursts interval (IBI);* **(f)** *bursts duration (BD)*

The BTNPs were added to the culture medium, in order to be in direct contact with the cells bodies (fig. 2.3a *bottom*). To determine whether the only presence of nanoparticles can affect the spontaneous activity of the cells, the firing rate before and after the BTNPs addition were compared. By qualitatively analyzing the behavior of cell cultures before (Fig. 2.3b *top*) and after the delivery of nanoparticles (Fig. 2.3b *bottom*), it was observed that there was no macroscopic differences in the spontaneous patterns of electrophysiological activity. The more accurate analysis showed that all parameters defining electrophysiological firing and bursting features of the networks did not reveal significant variations between the two conditions (Fig. 2.3c-f). With respect to the median values, it can be noted that the $MFR_{NOBTNPs}$ has a value of 1.54 sp/s which shift to 1.51 sp/s ($p = 0.76$) after the inclusion of nanoparticles, whereas for the MBR the median value moves from 5.49 bursts/min to 4.98 bursts/min ($p = 0.45$), therefore the frequency of firing

and bursting has not been affected by the BTNPs presence. Similarly, also the bursting features evaluated in terms of burst duration and inter burst interval do not show significant variations. Figures 2.3e and 2.3f reveal that the median of $BD_{NOBTNPs}$ settles at 94.10 ms while the BD_{BTNPs} at 95.89 ms ($p = 0.94$), in the same fashion the median value of the $IBI_{NOBTNPs}$ settles at 13.64 s and reaches 14.56 s ($p = 0.5$) with the nanoparticles.

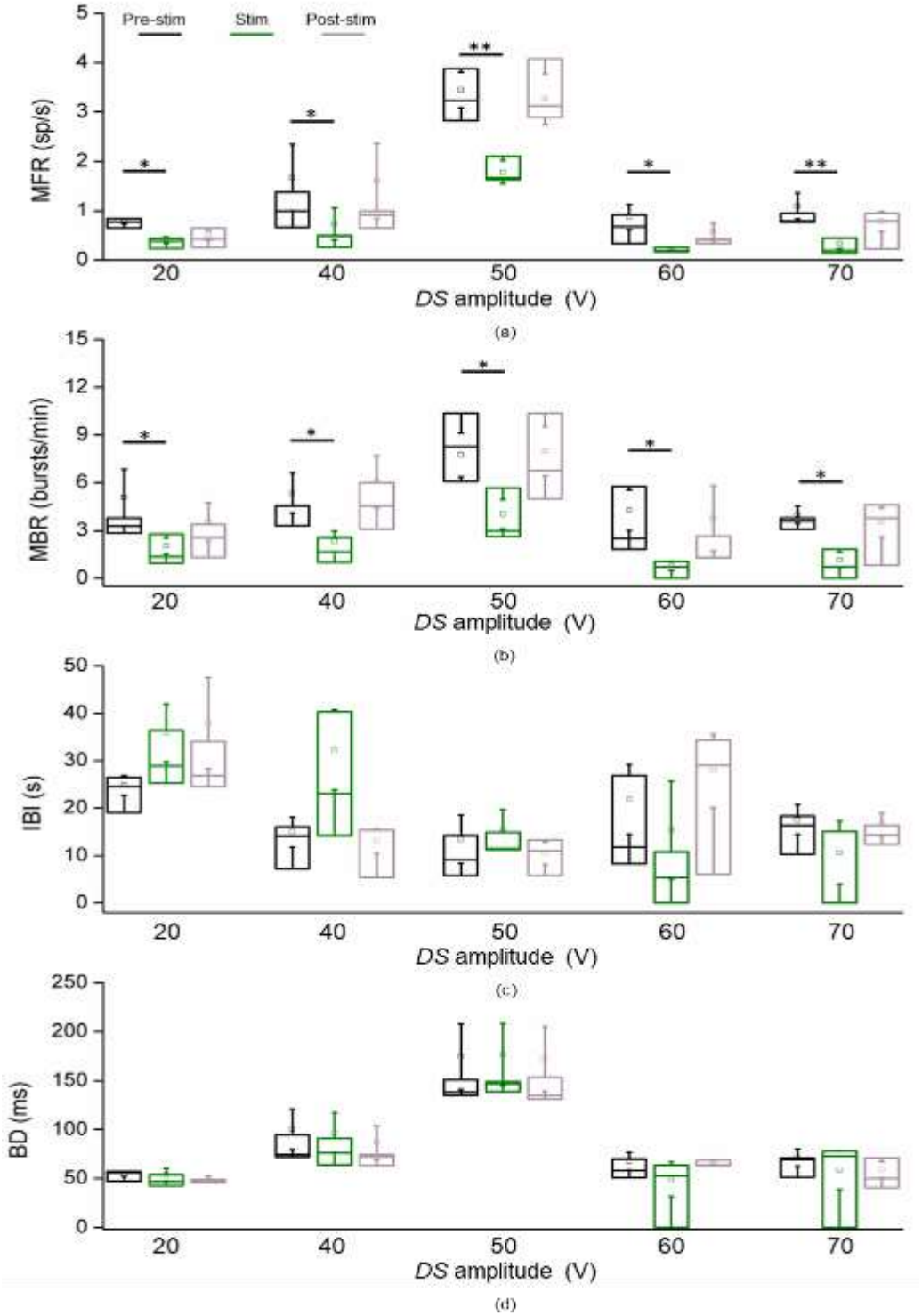

Figure 2.4 **(a)** *Spiking and* **(b-d)** *bursting activity of cortical cultures with BTNPs as a function of ultrasound DS*

To study the US effects on the cortical activity, each stimulation phase of the experimental

protocol (cf., Fig. 2.1e) was compared with its own pre- and post-phases. Fig. 2.4 shows these comparisons as a function of the used DS amplitudes. For all the considered voltage amplitudes (20, 40, 50, 60, and 70V), as cells are exposed to ultrasound stimulation mediated by piezoelectric nanoparticles, both spiking (MFR) and bursting (MBR) activity decreases in a statistically relevant manner between the pre-stimulus (black) and stimulation phase (green). Such a detected inhibition is transient, as in the post-stimulation phase (gray), both spiking and bursting activities recovery the initial conditions (pre-stimulus). Furthermore, although the US stimulation induces a substantial decrease in the frequency of the bursts, it does not modify their characteristics; in particular, the inter bursts interval (IBI) (Fig. 2.4c) and the duration of the burst (BD) (Fig. 2.4c) remain constant for all DS amplitudes during the three phases.

The MFR and MBR values were calculated considered all active channels (i.e., MFR ≥ 0.1 sp/s) detected during the pre-stimulation phase (C.f., Section 2.6). During the US stimulation, a decrease in firing activity was overall observed, and some electrodes were completely silent. In order to ensure whether this phenomenon was not due to irreversible damage to the neural network, but to a single transient effect associated with stimulation, the percentage of active channels ($\%Ch_{active}$) in the Pre-stim, Stim, and Post-stim phases was investigated. In order to compare the values of different cultures, for each experiment, the number of active channels was normalized to the corresponding value calculated before the stimulation phase (considered the reference percentage, such as 100% (pre-stim, black dots). Fig. 2.5a suggests that the $\%Ch_{active}$ during the stimulus phase (green dots) never dropped below 65% and remained at an average value of 90% for DS below 50V and about 68% for the highest simulation amplitudes. Therefore, I could assume that the reduction of the firing highlighted by the MFR and MBR parameters is related to the transient inhibition/depression of the whole network. In fact during the post-stimulation phase (gray dots) the percentage settled back to about 100%, reaching the lowest value of 93% for stimulation with a DS of 70V. It could therefore deduce the stimulus caused a transient inhibition, which was entirely reversible.

Since cortical networks were modulated by pulsed stimulation, the probability that the electrodes were activate during the stimulation phase ($P(Ch_{active})$) was assessed by keeping the on and off phases of the US train separate. Fig. 2.5b shows for one significant experiment and for each considered amplitudes, the probability that the channels are triggered during the off-period (US_{off}, red line) and on-period (US_{on}, green line). Up to 50V, a regular pattern of activation is clear and evident for all the off-periods during the entire stimulation (red lines), as well as the probability during the on-period (green lines). Moreover, Figure 5b indicates that the ($P(Ch_{active})$) is almost greater in the US off-period than in the on-period. Observing the last two panels of Fig. 2.5b, descriptive for 60V and 70V, it could also be observed that, the ($P(Ch_{active})$) during the US_{off} does not last for the entire duration of the US stimulation, but it interrupts after 10-20 pulses. Similarly, also

the probability of activation during the US_{on} (green lines) quickly decreases.

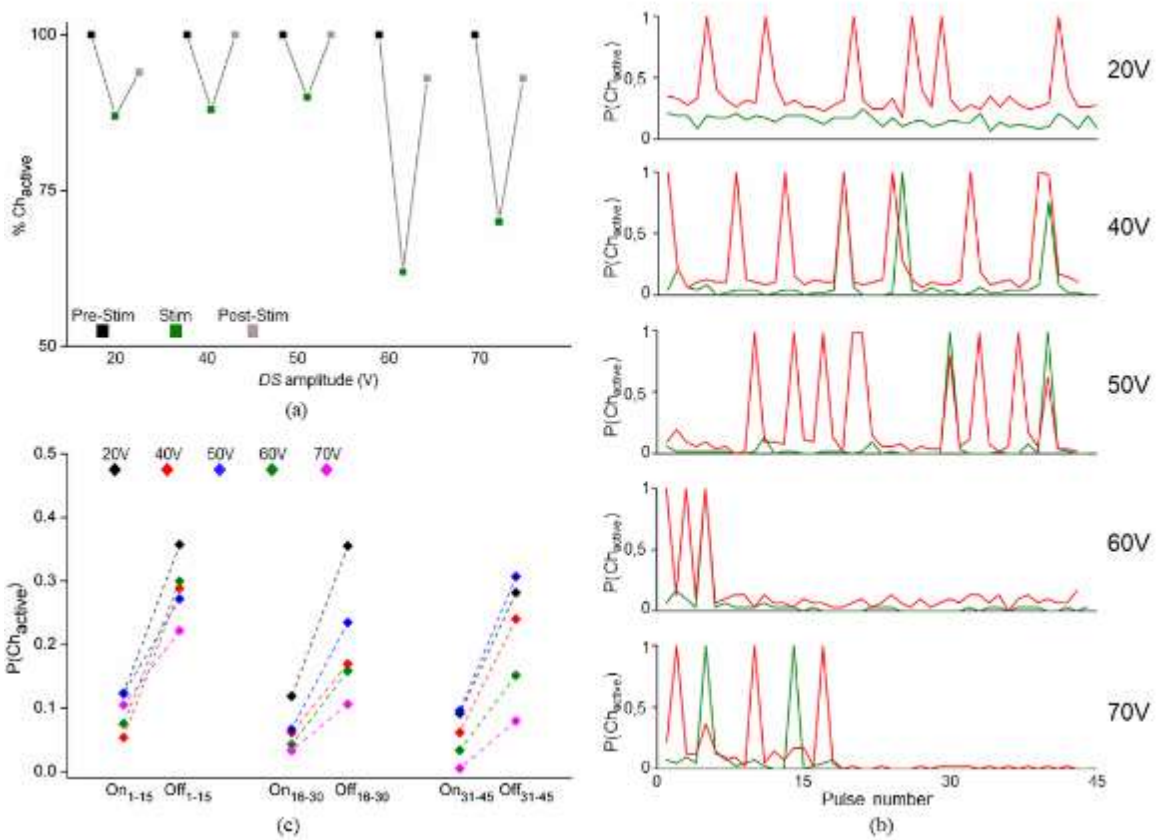

Figure 2.5: **a)** *Percentage of active channels (%Ch) as a function of different DS during the three protocol phases: pre-stimulus (Pre-Stim, black dots), stimulus (Stim, green dots) and post stimulus (Post-Stim, gray dots*). **(b)** *The trends of the probability of the active channels of a representative experiment in the 45 stimuli for the on (green line) and off period (red line) for the US stimulation amplitude of: 20V, 40V, 50V, 60V and 70V***; (c)** *probability that the electrodes are active during on and off stimulation phases divided into three stimuli groups (1-15, 16-30 and 31-45).*

To evaluate a possible involvement of network weakness due to US stimulation, the 45 stimuli were split into 3 groups of 15 for both US_{on} and US_{off} times. Figure 5c reinforces that for all US stimulus amplitudes in all 3 groups, the probability that the channels are involved is much higher in the US_{off} times than in the US_{on} ones. For 20V (black diamond), 40V (red diamond), and 50V (blue diamond) the probability that the channels are activated during the off-period compared to the on is statistically significant ($p < 0.04$) in all three groups. When the stimulation amplitude is set to 60V (green diamond) or 70V (magenta diamond), the significance difference between US_{on} and US_{off} periods for the second group is lost ($p = 0.1$ and $p = 0.08$, respectively) while it is kept for the first and third groups. In order to rule out any stimulation stress effect on the cortical networks, the ($P(Ch_{active})$) in the USo_{ff} periods for each amplitude were compared and no statistical differences among the three stimulation groups were found (20V: $p = 0.5$; 40V: $p = 0.08$; 50V: $p = 0.85$; 60V: $p = 0.13$; 70V: $p = 0.07$). The percentage of probability variation between the off and on period (% ΔP) highlights the stimulation propensity to decrease the chance of activation as the US amplitude increases. During the third stimulus period with the lowest amplitude, I

have a 20% variation with a 0.2 probability of activation between both on and off periods, and this % ΔP value was maintained constant up to 50V amplitude stimulation (40V: 18% with an average of 0.4 activation probability; 50V: 21% with an average of 0.21 activation probability). These values are close to those observed with the same amplitudes in the first stimulus group (1-15); in particular the % ΔP sets at 23% for 20V and 40V and 18% for 50V with average activation probability at 0.2, 0.17 and 0.21 respectively. These results further prove that there was no alteration in the activation trend during the 45 stimuli within this range of stimulation amplitudes.

At 60V and 70V stimulation amplitude, the % ΔP decreases to 12% and 7% with an average activation value of 0.09 and 0.05, respectively, during the last stimulus group (31-45). Compared to the same values with lower amplitudes, it points out that the probability of getting active channels is very low even in the US_{off} period, also confirmed by the higher % ΔP and the higher average probability of the first category of stimuli (1-15) at 60V and 70V: 22% of % ΔP with a medium activation probability of 0.18, and 12% with 0.05, respectively.

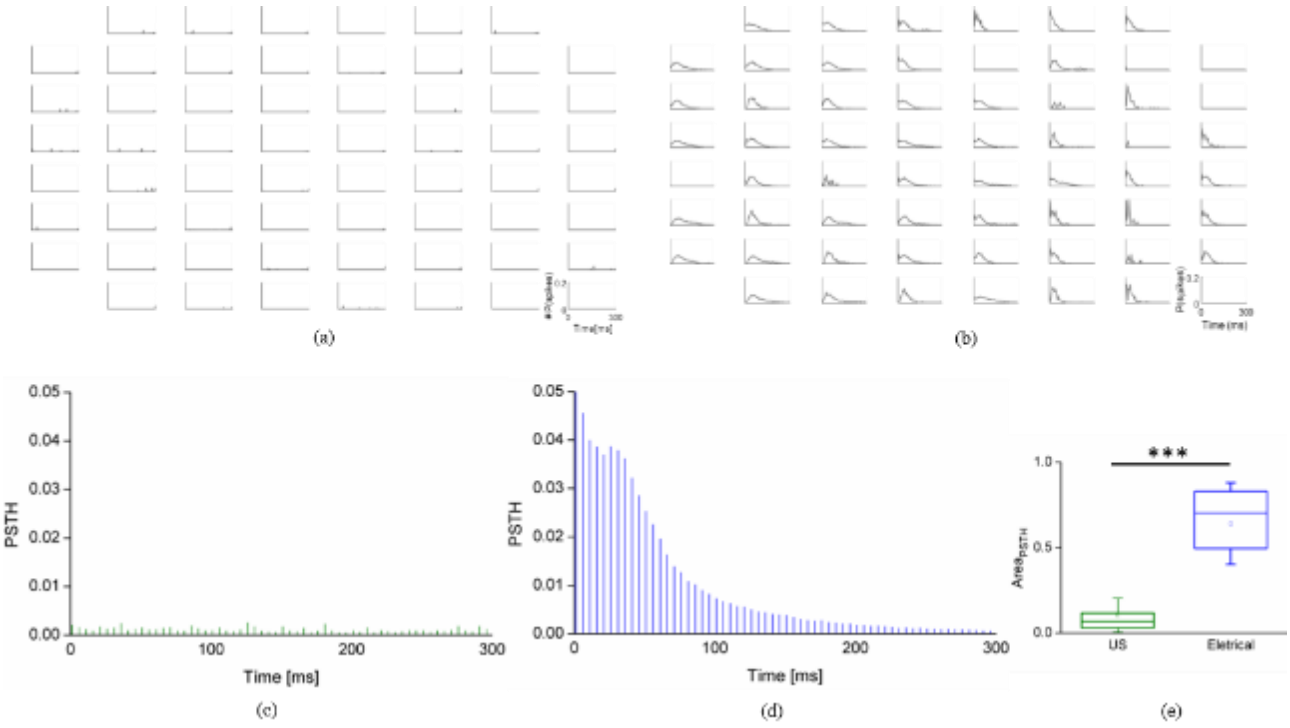

Figure 2.6: *Representative Post stimulus time histogram (PSTH) of the probability of channels activation after the delivery of:* **(a)** *US stimulation and* **(b)** *electrical stimulation (bin 5ms). Cumulative PSTH after the delivery of:* **(c)** *US stimulation and* **(d)** *electrical stimulation (bin 5ms)* **(e)** *PSTH area of the US and electrical stimulation.*

At the end of the each experimental session, cortical cultures were electrically stimulated by one randomly selected electrode to observe whether the cells were adequately receptive to external stimuli. Electrical stimulation was delivered for three minutes at an amplitude of ±1500 mV at the same frequency as US stimulation. I looked at the PSTH as the probability of the channels activation in the first 300 ms after electrical or US stimulation

(bin 5 ms). Fig. 2.6a shows the trend of PSTHs of all 60 channels of a representative cortical culture subjected to US stimulation at 50V, it can be observed that the most of channels do not exhibit any response in the 300 ms following the pulse. During this temporal window, some channels display electrophysiological activity, albeit in a scattered fashion over time. By examining the electrical stimulation delivered to the same culture, we may note that most of the channels are involved in the post-stimulation activity (Fig. 2.6b). Observing the cumulative PSTH of all cortical cultures interested by US stimulation (Fig. 2.6c), the almost flat and low (<PSTH> = 0.001) trend confirms the non-responsivity to the US stimulation. On the other hand, the cumulative PSTH induced by the electrical stimulation (Fig. 2.6d) shows that the probability of activation is very high during the first bins (fast AMPA receptors activation), to then decrease exponentially (after slow-NMDA receptor activation). In order to quantify the response at the two different stimulations, I compared the underlying PSTH areas that indicate a strong statistically difference ($p = 3.8 \cdot 10^{-7}$). This allows us to claim that cortical networks coupled to MEAs were actually able to respond to an external stimulation and, furthermore, as electrical stimulation was performed after ultrasound stimulation, it ensures that the US parameters did not stress the networks.

2.3.3 Ultrasound without BTNPs

The same stimulation protocol was used on a batch of n = 20 cortical cultures not treated with BTNPs. This control experiment (performed at DIV 21) allowed us to evaluate whether i) the decrease in firing and bursting rate was not related to damage caused by US waves and ii) the observed inhibitory effect was associated to the co-presence of US stimulation and piezoelectric nanoparticles. The analysis of sister cultures allowed to prove that both firing and bursting activity does not change as a result of a mere US stimulation without the delivery of BTNPs (Fig. 2.7).

The electrophysiological activity preserves the same trend in pre-, post- and stimulation phases on average, without any statistical wariations. In order to confirm that mere stimulation, in the absence of piezoelectric nanoparticles, has no impact on cortical cultures, the number of active channels in the three phases of the stimulation experiment has also been assessed. With respect to the number of active channels during the pre-stimulation phase, no significant decrease during stimulation was observed: the channel activation percentage was set to 99% for 20V and 70V, and to 100% for the remaining stimulation amplitudes. In the post-stimulation period, the channel activation percentage

remained at 99% for 20V, 40V and 60V and to 96% for 50V and 70V.

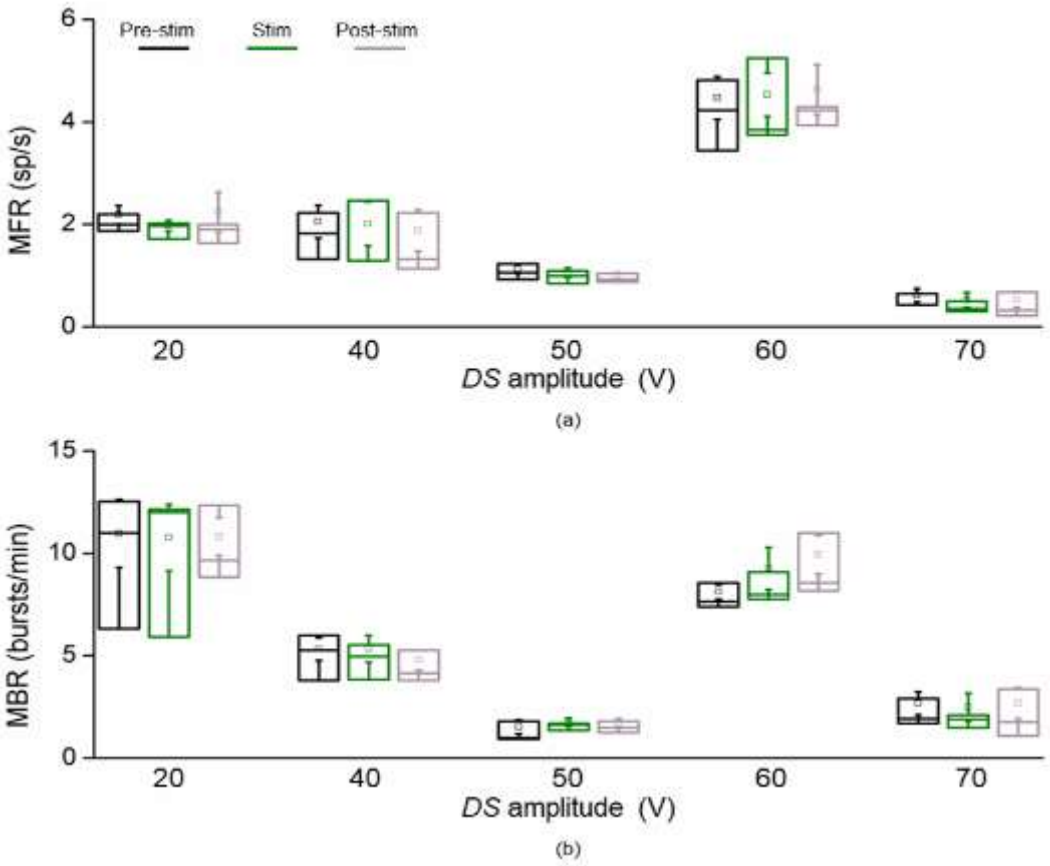

Figure 2.7: **(a)** *Spiking and* **(b)** *bursting activity of cortical cultures with BTNPs as a function of ultrasound DS amplitude.*

2.4 Conclusions

US stimulation is emerging as an alternative noninvasive brain modulation technique in neuroscience (Blackmore et al., 2019). Previous studies demonstrated the possibility of neuronal stimulation using nanomaterials (Rojas et al., 2018) (Marino et al., 2020). In (Rojas et al., 2018) it was observed that extremely low US intensity of about 1-2 kPa, coupled with BTNPs, induced an excitation on both cortical and hippocampal neuronal networks.

In this work, I studied the effects of higher US pressure fields (from 0.05 to 0.3 MPa) on networks of neurons from the rat cortex, and I observed that US stimulation causes a reproducible and reversible inhibition of the spontaneous activity. The inhibition, characterized for different US intensities, could be selectively observed for the duration of the stimulus. In fact, I also found that after the stimulation the network recovers to the spontaneous activity observed before, both in terms of firing and bursting rate. I also evaluated the changes in the temperature medium during the stimulation protocol. The temperature increase is below what is considered safe by the FDA in terms of the Termal Index (TI) value. Furthermore, control experiments show that the same temperature increase does not cause any change in the spontaneous electrical activity of the neuronal network when BTNPs are not present.

The response I observed (i.e., activity inhibition rather than excitation) could be ascribed to a localized rise in temperature caused by the interaction of US and nanoparticles. Indeed, nanoparticles have been used to induce localized heating when irradiated with hexogen stimuli (Kabb et al., 2015; Kaczmarek et al., 2018). Considering that the mechanism of neurons inhibition is a complex function affected by the heat dependence of membrane conductance, membrane potential and capacitance changes, one can speculate that the heating induced by the nanoparticles adsorbed on the cell membrane could cause a temporal inhibition on the cortical activity as observed using gold nanorods absorbing near infrared light (Yoo et al., 2014).

Based on these preliminary results I propose a US stimulation regime at higher intensities than previous work conducted in my lab, however still well below any threshold to be considered safe for humans, which provide a different electrophysiological response with respect to the one previously observed in the same experimental model (i.e. inhibition instead of excitation). If more systematic experiments will confirm this trend, and a biophysical model of the transduction mechanism capable to interpret both results will be developed, US stimulation mediated by piezoelectric nanoparticles could represent an extremely powerful neuromodulation technique with a translational potential in the clinics.

References

Blackmore, J., Shrivastava, S., Sallet, J., Butler, C. R., & Cleveland, R. O. (2019). Ultrasound Neuromodulation: A Review of Results, Mechanisms and Safety. In *Ultrasound in Medicine and Biology* (Vol. 45, Issue 7, pp. 1509–1536). Elsevier USA. https://doi.org/10.1016/j.ultrasmedbio.2018.12.015

IEC 62359: Ultrasonics – Field characterization – Test methods for the determination of thermal and mechanical indices related to medical diagnostic ultrasonic fields; International Standard IEC 62359 Ed.2.0, Geneva 2010-10. (n.d.).

Kabb, C. P., Carmean, R. N., & Sumerlin, B. S. (2015). Probing the surface-localized hyperthermia of gold nanoparticles in a microwave field using polymeric thermometers. *Chemical Science*, *6*(10), 5662–5669. https://doi.org/10.1039/c5sc01535a

Kaczmarek, K., Hornowski, T., Kubovč, M., Timko, M., Koralewski, M., & Józefczak, A. J. (2018). *Heating Induced by Therapeutic Ultrasound in the Presence of Magnetic Nanoparticles*. https://doi.org/10.1021/acsami.8b02496

Marino, A., Genchi, G. G., Pisano, M., Massobrio, P., Tedesco, M., Martinoia, S., Raiteri, R., & Ciofani, G. (2020). Nanomaterial-Assisted Acoustic Neural Stimulation. In *Neural Interface Engineering* (pp. 347–363). Springer International Publishing. https://doi.org/10.1007/978-3-030-41854-0_15

Rojas, C., Tedesco, M., Massobrio, P., Marino, A., Ciofani, G., Martinoia, S., & Raiteri, R. (2018). Acoustic stimulation can induce a selective neural network response mediated by piezoelectric nanoparticles. *Journal of Neural Engineering*, *15*(3), 036016. https://doi.org/10.1088/1741-2552/aaa140

Tyler, W. J. (2011). Noninvasive neuromodulation with ultrasound? A continuum mechanics hypothesis. *Neuroscientist*, *17*(1), 25–36. https://doi.org/10.1177/1073858409348066

Yoo, S., Hong, S., Choi, Y., Park, J. H., & Nam, Y. (2014). Photothermal inhibition of neural activity with near-infrared-sensitive nanotransducers. *ACS Nano*, *8*(8), 8040–8049. https://doi.org/10.1021/nn5020775

Chapter 3

Activation of Piezo1 by US

3.1 Abstract

As discussed in the previous chapters, several research groups have studied US effects on electrical activity of nervous tissue, with the aim of employing US neuromodulation as a method for treating mental and neurological disorders (Chan et al., 2017; Menz et al., 2013; Tufail et al., 2010; Tyler et al., 2008). Nevertheless, the mechanisms underlying US neurostimulation are still unclear; these may include mechanical forces, heating, and cavitation. In this work I investigated the effects of US on the membrane channel Piezo1 expressed in a model cell line (HEK-293) by imaging intracellular calcium dynamics. The focus of this study was to evaluate whether US can activate Piezo1, which is a cationic channel sensitive to plasma membrane mechanical deformations. Piezo1 channels have been found in the peripheral nervous system of mammals (e.g. DRG cells) but not in the brain (Coste et al., 2010). Therefore the long term strategy would be to render a neuronal population in the brain selectively sensitive to low intensity US by overexpressing Piezo1 (e.g. by exploiting some gene therapy approach).

3.2 Experimental Protocol and Analysis

3.2.1 Experimental protocol.

The experimental set-up for simultaneous US stimulation and calcium imaging recording of cultured cells is illustrated in Chapter 1. Briefly, the set-up is based on a iMIC microscope and a 1MHz US transduecer. An US unfocused beam was trasmitted from the piezoelectric transducer directly immersed into the culture medium above the culture substrate and positioned parallel to it. I also verified, using a needle hydrophone, that with this configuration the US field resulted uniform over the cell culture area. HEK293 cells were plated into glass-bottomed Petri dishes (C.f., Chapter 1 | 1.4.4). On the day of the experiment, the cells were removed from the incubator, loaded with the calcium sensitive fluorescent dye (Fluo4 C.f., Chapter 1 | 1.5.2), and placed back in the incubator for 20 minutes. After that the culture medium was replaced by 2 ml buffer solution and the recording area was selected using the motorized stage of the microscope. Cells were then exposed to a train of US pulses with a period of 100 ms and a duty cycle of 10% for a total time of 2 seconds. The same experimental protocol was repeated at different US intensities and for three different cell culture substrates: uncoated glass, 4 kPa PMMA hydrogel layer, and 40 kPa PMMA hydrogel layer (Fig. 3.1). PMMA layers were deposited at the Centro Cardiologico Monzino IRCCS in Milan, using the protocol described in (Santoro et al., 2018). The resulting thickness of the layer was estimated to be 200 µm.

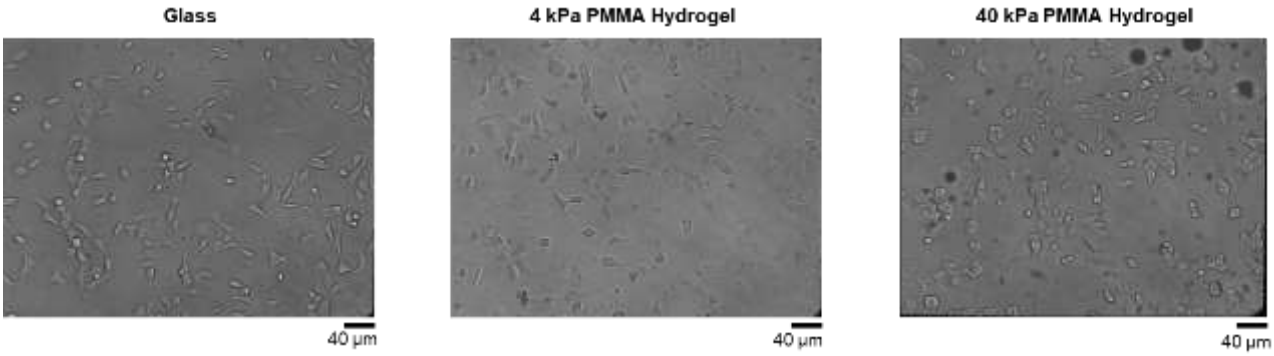

Figure 3.1: *Optical images of HEK 293 cells plated on different substrates: glass (left), 4 kPa PMMA hydrogel (middle) and 40 kPa PMMA hydrogel (right).*

3.2.2 Data Analysis

Data were analyzed using Fiji, an open source image processing package based on ImageJ2, and Ana Software, open source software developed by Michael Pusch. Curve fitting was performed using MatLab. All data presented are the average at least three experimental sessions. Appendix A contains a detailed description of the analysis protocol. The percentages shown in the results were determined using three Petri dishes containing an average of n = 50 cells. The box plots representation indicates the percentile 25-75 (box), the standard deviation (whiskers), the mean (square), and the 99% (x) of values.

3.3 Results

I evaluated how the calcium signal upon US exposure is related to the expression of Piezo1, US intensity, and the stiffness of the substrate. The signal I measured in the experiments is the intensity emitted by a calcium dye (Fluo4, Fig. 3.2) and how it varies over time during US stimulation. Different processes can induce changes in the intensity of the signal: I considered a decrease (modeled as exponential) due to photobleaching of the dye and an increase due to the opening of the Piezo1 channels that allow calcium influx which, in turn, can trigger calcium release from intracellular stores.

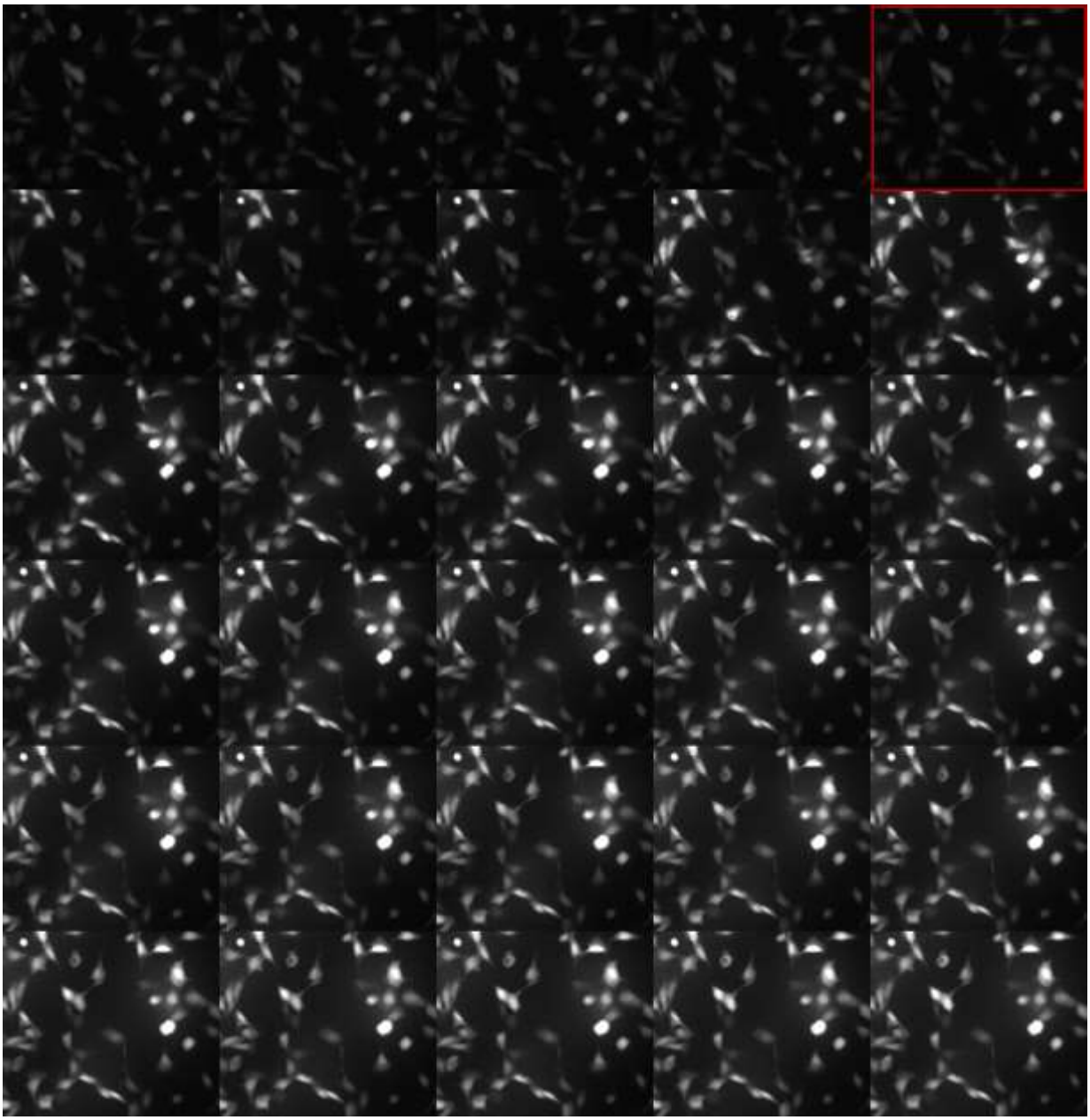

Figure 3.2*: Sequence of successive calcium images for a representative experiment showing the increase in intensity emitted by the calcium dye after US stimulation. The red mark indicates when the US stimulation is started; time interval between images: 0.33 s.*

For the results, I analyzed the fluorescence imaging stack of the cells to detect those which

increase their fluorescence intensity (I_F). As a result, I measured the percentage of cells with Piezo1 channel activation in relation to the total number of cells in the optical region. Moreover, a normal calcium signal was characterized by the descendent pattern that is typical of photobleaching, the photochemical irreversible inactivation of a dye. I analyzed the calcium signal integrated over a single cell by looking for a change in its concavity (i.e. change in sign of the second derivative: inflection point) after the beginning of the US stimulation as a marker of activation (i.e. opening) of the Piezo1 channels. Moreover, I determined the time interval (ΔT) between the start of US stimulus and the Piezo1 activation (i.e. inflection point).

3.3.1 HEK 293 cells and ultrasound

Firstly, I verified the normal calcium signal trend of transfected cells to express Piezo1 channels, without US stimulation. Figure 3.3a shows the expected exponential decrease of the I_F due to photobleaching. Then, to evaluate whether the calcium transients could be induced by US stimulation only, I submitted non-transfected HEK 293 cells to the US stimulation protocol at intensities of 0.21, 2.56 and 6.78 W/cm^2. Figure 3.3b reports the calcium signal response of three representative cells for the three US intensities which follow the decrease due to photobleaching. As a result, I deduced that US alone cannot induce calcium transients in HEK 293. The same experiments were performed on cells transfected in order to express CD8 membrane protein instead of Piezo1. As shown in Fig 3.3c, US did not induce any effect on the recorded I_F signal, as a clear indication that the cell transfection procedure itself does not sensitize cells to US. This control was replicated for n = 50 cells for each cell substrate (glass, 4 kPa hydrogel, and 40kPa hydrogel) producing the same results, reported in figure 3.3c.

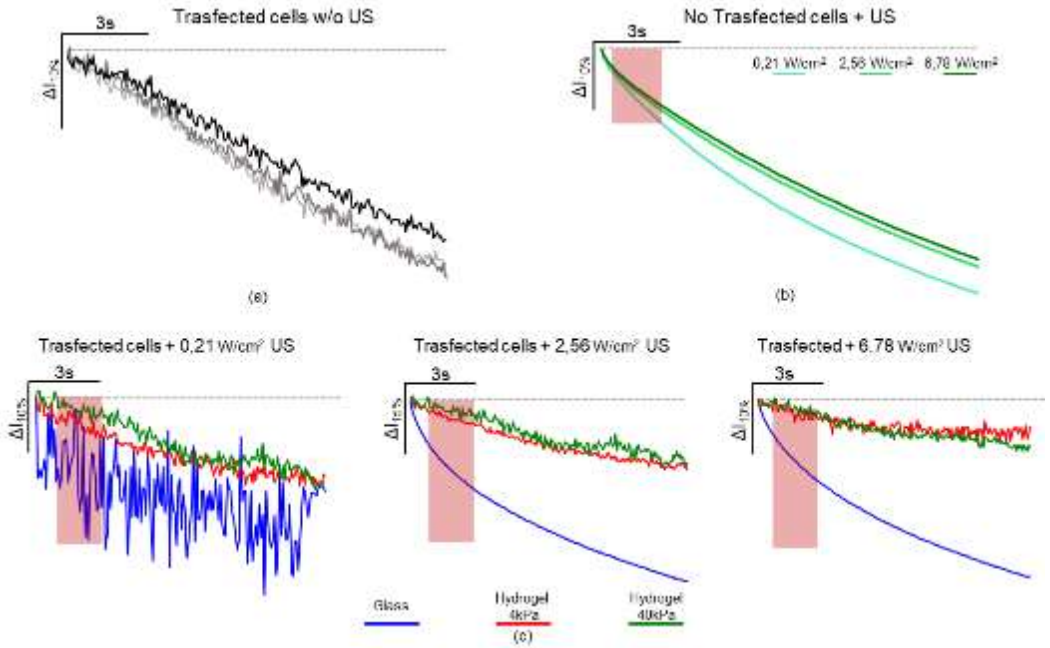

Figure 3.3: *Results of calcium imaging of control experiments: (a) Photobleaching pattern of transfected HEK cells in absence of US stimulus. (b) HEK 293 non transfected and subjected to US stimulation (red rectangle) at different intensities: 0.21 W / cm^2, 2.56W / cm^2 and 6.78 W / cm^2. (c) HEK 293 transfected to express CD8 protein US stimulated (red rectangle) at different intensities and plated on different substrates: glass (blue), 4 kPa hydrogel (red) and 40 kPa hydrogel (green)*

At this point, I investigated the calcium signal in HEK cells transfected with Piezo1 channels and stimulated with different intensities of US. This was carried out for each of the substrates used for cell plating. I started studying the responsiveness of cells plated directly on a glass coverslip. Figure 3.4a shows the ΔT between US stimulus starting instant and the inflection point of fluorescence intensity as a function of US intensities. The cells started to exhibit Piezo1 channel activation after US stimulation at 0.02 W / cm^2. In this case, a small rise in I_F was rapidly depleted (Fig. 3.4b). Furthermore, the percentage of activated cells was equal to 16% for this US intensity. The same trend was observed with a 0.08 W/cm^2 US, with the only difference being an activation percentage that settled around 29%. From 0.21 to 6.78 W/cm^2, the Piezo1 channels were triggered with rising percentages of 34%, 42%, 67%, 85%, and the I_F started to increase with smaller ΔT, indicating a more pronounced correlation with US stimulation. We may deduce that the decrease in ΔT was caused by higher US intensities, which resulted in the opening of a larger number of Piezo1 channels. For the two maximum US intensities (2.56 and 6.78 W / cm^2), it is worth noting that the ΔT was determined based on the detection of the inflection that blocked the photobleaching pattern. The final fluorescence peak was triggered at a ΔT of around 1.26 s and 1.98 s for intensities of 2.56 and 6.78 W / cm^2, respectively, after a brief increase in the observed I_F trend. Figure 3.4b shows representative trends of a cells I_F for each US intensities.

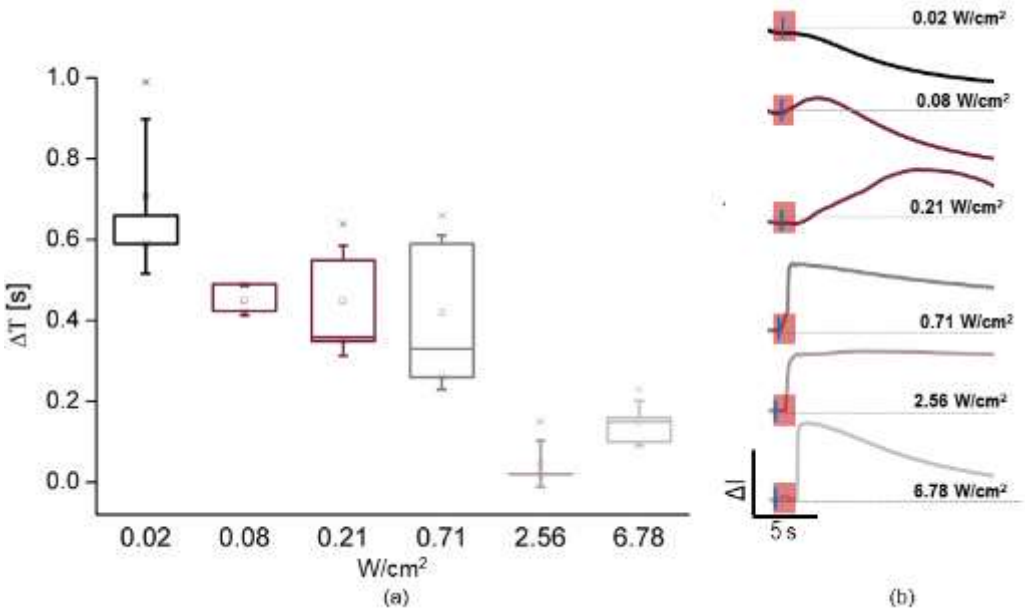

Figure 3.4*: **(a)** Time difference (ΔT) between the start of US stimulation and the inflection of the fluorescence intensity of the cells (related to the calcium transients) as a function of US intensities. Measured on n = 5 cells.* **(b)** *Fluorescence intensity trends of a representative cell for each US intensities. The red square indicates the US stimulation, while the blue line indicates the inflection point.*

The activation of Piezo1 channels in response to US was then observed in cells on a 40 kPa hydrogel substrate. With 0.02 and 0.08 W / cm^2 US stimulation, I_F increased for 0% of the cells, and no inflection was observed. The first I_F increase was observed with 0.21 W / cm^2 US intensity. In this case, the I_F was detected about 0.7 s after the s and art of US stimulation (Fig. 3.5a), and returned to basal values after a few minutes, but only 17% of the cells followed this pattern. By increasing the stimulus intensity to 0.71W / cm^2, the cells responsiveness was comparable to those

observed for cells plated directly on glass (Fig. 4b). The I_F increment was detected about 0.3s after the US stimulus and about 42% of cells were activated (Fig. 3.5a). The I_F gradually increased up to 3 seconds, then continued to rise more rapidly (Fig. 3.5b). For the highest US intensities, 2.56 W / cm^2 and 6.78 W / cm^2, the photobleaching effect stopped after about 0.21s and 0.14s (Fig. 3.5a) leading to the rapid increase in intensity after 0.83s and 1.21s (Fig. 3.5b), respectively. For stimulation at 2.56 W / cm^2 the activation percentage settled at 65% while for 6.78W / cm^2 at 77%.

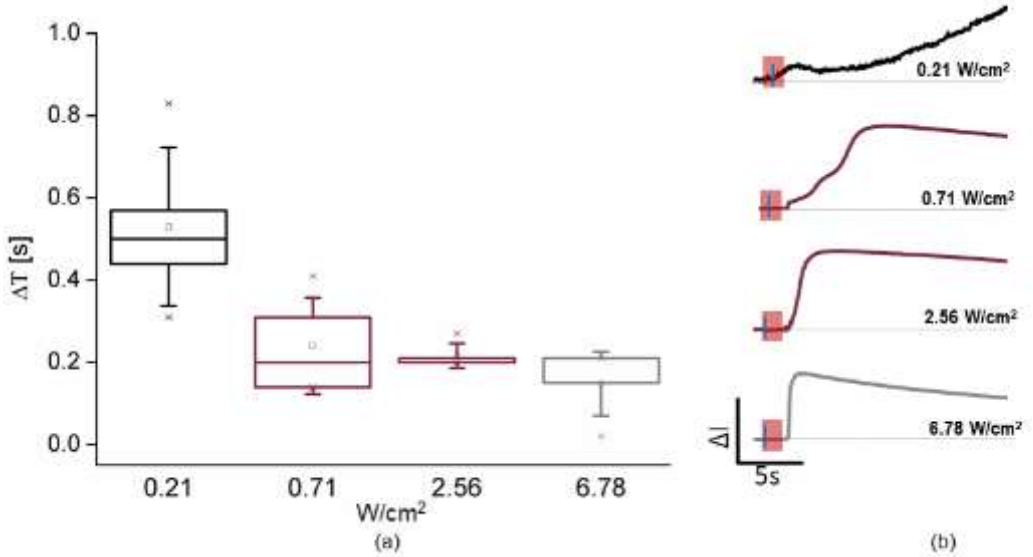

Figure 3.5 *(**a**) Time difference (ΔT) between the start of US stimulation and the inflection of the fluorescence intensity of the cells (related to the calcium transients) as a function of US intensities. Measured on n = 5 cells.* ***(b)*** *Fluorescence intensity trends of a representative cell for each US intensities. The red square indicates the US stimulation, while the blue line indicates the inflection point.*

Finally, the same analysis was performed on cells plated on 4 kPa hydrogels. The first ultrasound intensity at which the piezoelectric channels were activated in this case was 0.71 W / cm2, while the lowest intensities (i.e., 0.02, 0.08, and 0.21 W / cm^2) exhibited 0% cells reactive to stimulus. A clear calcium transient peak was not observed, a small rise in the I_F of the cells was found at a ΔT of 1.7 s, which blocked the photobleaching trend (Fig. 3.6a). The percentage of cells settles at about 17%. As the pressure of the US was increased to 2.56 W / cm^2, a more pronounced rise is observed (Fig. 3.6b), but only in approximately 20% of the cells. In this case the increment in I_F started at ΔT of 1.21 s (Fig. 3.6a). US intensities of 5.12 and 6.78 W / cm^2 showed typical peaks associated with calcium transients (Fig. 3.6b) and the percentage of activated cells settled at values of 38% and 65%, respectively. It should be noted that for higher intensities, the image acquisition was influenced by the US induced vibration, making it difficult to detect the exact moment when the curve began to rise, and the calculation could be affected by smaller precision errors. However, the inflection that interrupted the photobleaching pattern was observed at ΔT values of around 0.43 and 0.26 s for intensities of 5.12 and 6.78 W / cm^2, respectively (Fig. 3.6b); furthermore, the usual peak of calcium transients was triggered with a slight delay, after 1.79s (5.12 W / cm^2) and 1.32s (6.78 W / cm^2) with respect to the start of ultrasound stimulation.

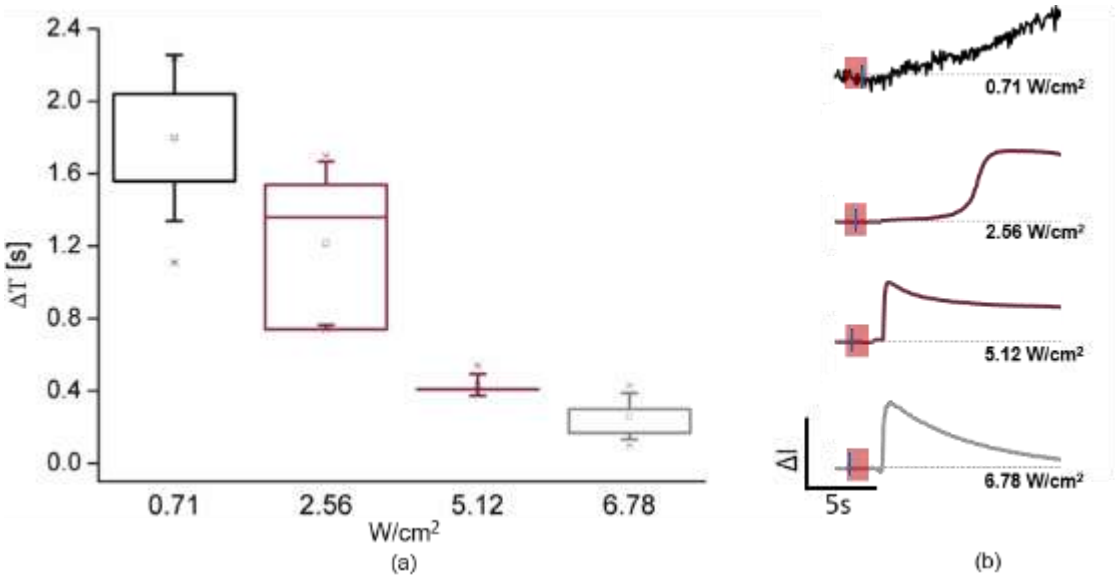

Figure 3.6: **(a)** *Time difference (ΔT) between the start of US stimulation and the inflection of the fluorescence intensity of the cells (related to the calcium transients) as a function of US intensities. Measured on n = 5 cells.* **(b)** *Fluorescence intensity trends of a representative cell for each US intensity. The red square indicates the US stimulation, while the blue line indicates the inflection point.*

Figure 3.7 shows the percentage of cells that displayed intracellular calcium increase for the three different substrates as a function of US intensity. Cells plated directly on glass consistently demonstrated the highest activation rate, with 30% of activated cells for a stimulus at 0.08 W / cm^2) and more than 50% for 2.56 W / cm^2 and up to 85% for 6.78 W / cm^2. Cells plated on 40 kPa hydrogels displayed activation percentages very close to those of glass for US pressure values greater than 0.71 W / cm^2, stopping at 78% for the larger intensities. Regarding the cells plated on 4 kPa hydrogels, it was observed that Piezo1 channels were activated only for very high US intensity values, but they included less than half of the cells for sound stimulus up to 5.12 W / cm^2, and only for the maximum intensity they achieved 65% activation.

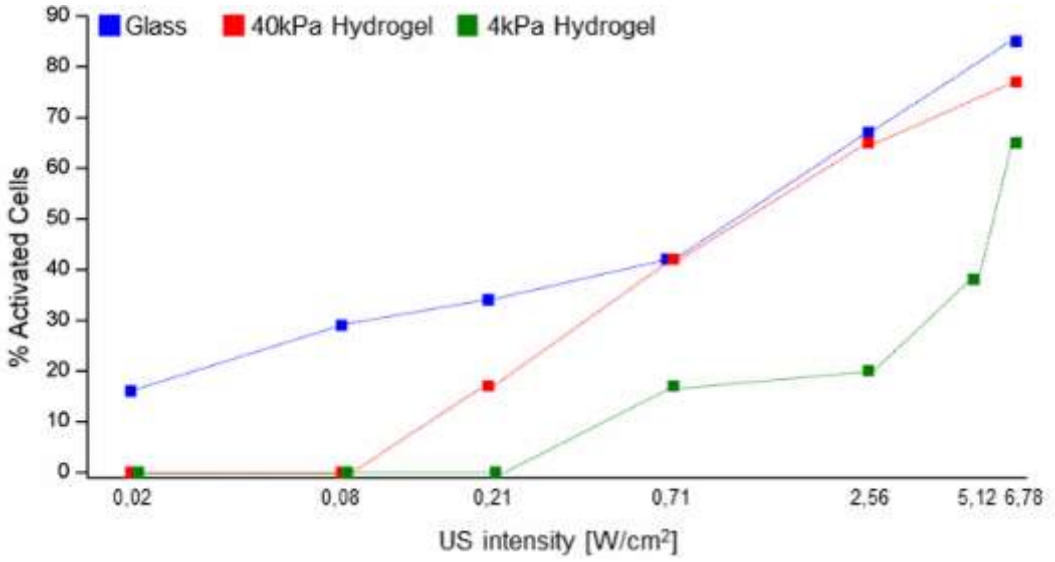

Figure 3.7: *Percentage of the activated cells on the different substrate: glass (blue squares), 40 kPa hydrogel (red squares) and 4 kPa hydrogel (green squares). The percentage was calculated on about n= 200 cells for each experimental configuration. US intensities were reported on a logarithmic scale.*

3.4 Conclusions

The experiments reported here agree with the work published by (Qiu et al., 2019) and confirm that the mechanical stimulation produced by low-intensity US (i.e. in a sub-cavitation regime and short enough to induce neglectable temperature increases (C.f., Chapter 2, I used the same US set up) is capable to activate Piezo1 channels and generate a detectable collective ion flux at the single cell level.

I observed an effect of the US intensity which I quantified as the percentage of cells over the whole population that showed an increase in fluorescence following US stimulation. More interestingly, for the first time in my knowledge, I also investigated the effect of the cell substrate on such response. The motivation for adding an hydrogel layer as cell culture substrate was twofold: on one end I wanted to move away cells from the solution/glass interface: due to the large difference in acoustic impedances between the two media there might be effects on US propagation (e.g. reflections and interferences) which might cause relevant mechanical effects in the region close to the interface on the other end it is well known that cells are sensitive to the mechanical properties of the substrate and respond accordingly rearranging their cytoskeleton; it has been shown that Piezo1 is not directly activated by mechanical stresses applied to the plasma membrane (Coste et al., 2010) but is also involved in the transduction of changes of ECM stiffness into a physiological response (Chakraborty et al., 2021; Emig et al., 2021; Wang et al., 2021). It seems therefore reasonable that its activation to the mechanical stimulation provided by the US pressure wave is affected by the substrate stiffness either directly or indirectly by a cytoskeleton reorganization.

Indeed, I observed an increase in the percentage of activation for the hydrogel with higher stiffness at all intensities. Accordingly, for glass I observed a response at even lower intensities, while at higher intensities the response was similar to the one for the stiffer hydrogel. This result is relevant not only for the basic understanding of the mechanism of sonogenetics, but also when thinking of translating this technology in vivo, where the microenvironment sense by cells has mechanical properties more similar to a soft hydrogel rather than a hard glass substrate.

From the preliminary results I obtained it seems that “moving away” the cells from the solution/glass interface by 200 µm did not induce a significative difference in the calcium response. One should not that that the wavelength of 1 MHz US wave propagating in water is 1.48 mm: the difference in the position of the cells with respect to the interface with glass was therefore only 13% of the wavelength and therefore interference effects due to reflections, even if present, might not be relevant.

The experimental setup I used limited the maximum thickness of the hydrogel since the US transducer is immersed in the solution from the top and the microscope objective needs therefore to approach from below. More experiments are needed, possible with a setup where US stimulation is coupled to the cell culture dish from the bottom in order to approach the cell culture plane with an objective from the top.

References

Chakraborty, M., Chu, K., Shrestha, A., Revelo, X. S., Zhang, X., Gold, M. J., Khan, S., Lee, M., Huang, C., Akbari, M., Barrow, F., Chan, Y. T., Lei, H., Kotoulas, N. K., Jovel, J., Pastrello, C., Kotlyar, M., Goh, C., Michelakis, E., … Winer, D. A. (2021). Mechanical Stiffness Controls Dendritic Cell Metabolism and Function. *Cell Reports*, *34*(2), 108609. https://doi.org/10.1016/j.celrep.2020.108609

Chan, R. W., Leong, A. T. L., Ho, L. C., Gao, P. P., Wong, E. C., Dong, C. M., Wang, X., He, J., Chan, Y. S., Lim, L. W., & Wu, E. X. (2017). Low-frequency hippocampal–cortical activity drives brain-wide resting-state functional MRI connectivity. *Proceedings of the National Academy of Sciences of the United States of America*, *114*(33), E6972–E6981. https://doi.org/10.1073/pnas.1703309114

Coste, B., Mathur, J., Schmidt, M., Earley, T. J., Ranade, S., Petrus, M. J., Dubin, A. E., & Patapoutian, A. (2010). Piezo1 and Piezo2 are essential components of distinct mechanically activated cation channels. *Science*, *330*(6000), 55–60. https://doi.org/10.1126/science.1193270

Emig, R., Knodt, W., Krussig, M. J., Zgierski-Johnston, C. M., Gorka, O., Groß, O., Kohl, P., Ravens, U., & Peyronnet, R. (2021). Piezo1 Channels Contribute to the Regulation of Human Atrial Fibroblast Mechanical Properties and Matrix Stiffness Sensing. *Cells*, *10*(3), 663. https://doi.org/10.3390/cells10030663

Menz, M. D., Oralkan, Ö., Khuri-Yakub, P. T., & Baccus, S. A. (2013). Precise neural stimulation in the retina using focused ultrasound. *Journal of Neuroscience*, *33*(10), 4550–4560. https://doi.org/10.1523/JNEUROSCI.3521-12.2013

Qiu, Z., Guo, J., Kala, S., Zhu, J., Xian, Q., Qiu, W., Li, G., Zhu, T., Meng, L., Zhang, R., Chan, H. C., Zheng, H., & Sun, L. (2019). The Mechanosensitive Ion Channel Piezo1 Significantly Mediates In Vitro Ultrasonic Stimulation of Neurons. *IScience*, *21*, 448–457. https://doi.org/10.1016/j.isci.2019.10.037

Santoro, R., Scaini, D., Severino, L. U., Amadeo, F., Ferrari, S., Bernava, G., Garoffolo, G., Agrifoglio, M., Casalis, L., & Pesce, M. (2018). Activation of human aortic valve interstitial cells by local stiffness involves YAP-dependent transcriptional signaling. *Biomaterials*, *181*, 268–279. https://doi.org/10.1016/j.biomaterials.2018.07.033

Tufail, Y., Matyushov, A., Baldwin, N., Tauchmann, M. L., Georges, J., Yoshihiro, A., Tillery, S. I. H., & Tyler, W. J. (2010). Transcranial Pulsed Ultrasound Stimulates Intact Brain Circuits. *Neuron*, *66*(5), 681–694. https://doi.org/10.1016/j.neuron.2010.05.008

Tyler, W. J., Tufail, Y., Finsterwald, M., Tauchmann, M. L., Olson, E. J., & Majestic, C. (2008). Remote excitation of neuronal circuits using low-intensity, low-frequency ultrasound. *PLoS ONE*, *3*(10). https://doi.org/10.1371/journal.pone.0003511

Wang, B., Ke, W., Wang, K., Li, G., Ma, L., Lu, S., Xiang, Q., Liao, Z., Luo, R., Song, Y., Hua, W., Wu, X., Zhang, Y., Zeng, X., & Yang, C. (2021). Mechanosensitive Ion Channel Piezo1 Activated by Matrix Stiffness Regulates Oxidative Stress-Induced Senescence and Apoptosis in Human Intervertebral Disc Degeneration. *Oxidative Medicine and Cellular Longevity*, *2021*. https://doi.org/10.1155/2021/8884922

Chapter 4

US-mediated Drug Delivery

4.1 Abstract

In recent years, demand for novel drug delivery systems has risen to minimize the adverse effects associated with systemic administration of drugs that affect both healthy and diseased tissues. Controlled and targeted drug release will lead to an improvement in the effectiveness and safety of the treatment, with positive effects for the health of the patient (Ricotti et al., 2015). In particular, there is an increasing interest in *Pulsatile Drug Delivery Systems* (PDDS) that allow targeted treatment in spatial and temporal terms (Arora et al., 2006). The aim of this work is ultrasound (US) as a fully non-invasive method for developing a protocol for the release of a model drug (doxorubicin) contained in polyelectrolyte microcapsules (PCs) (Cf., Chapter 1 | 1.6). The proposed ultrasound-based release protocol was first characterized and then tested *in vitro* for cancer cells, MCF7 (Cf., Chapter 1 | 1.4.5). We have therefore demonstrated that the use of the appropriate transducer enables the release of the drug from the capsules in a controlled manner, to be safe for human tissues and to respect the biocompatible values of the mechanical and thermal index.

4.2 Experimental Protocol and Analysis

4.2.1 Experimental protocol.

The US-based drug delivery method was tested with microcapsules made with synthetic polymers (PSS/PAH) and capsules made with biopolymers (DEX/PLA). The PCs were obtained on the day of the experiment using the LbL approach outlined in chapter 1 | 1.6.1. For *in vitro* tests, after 24 h from plating, MCF7 cells are taken from the incubator and exposed to different conditions: DOX-loaded PCs with and without US stimulation, hollow PCs without US stimulation, and DOX-free with and without US stimulation (the latter configuration was only tested for bio-polymeric capsules). In particular, DOX-loaded PCs at the final DOX concentration of 8 μg/ml were added to each Petri. To maintain consistency, the same amount of hollow PCs was added. For DOX-free samples, two different concentrations of DOX were directly added to each Petri: 30% and 70% of the total, i.e. 8 μg/ml. Moreover, cells directly treated and no treated with US stimulation were cultured as a control in order to evaluate the cell response to US. The US stimulation was applied immediately after the addition of the PCs onto cells. To generate the US I employed the *Sonidel setup* (Cf. Chapeter 1 | 1.1.2.). In order to minimize thermal effects, the ultrasonic treatments were performed within 0.25 – 1.5 W/cm^2 US intensity range, with 100 Hz pulse frequency and 20% duty cycle. The US transducer was positioned over the Petri dish containing the sample to be exposed, directly in contact with the solution.

4.2.2 Data Analysis

All the parameters used for the analyses have been described in chapter 1. For in vitro studies, cell viability was investigated using an MTT test (Cf., Chapter 1 | 1.4.6.). As already reported (Missirlis et al., 2006), DOX absorbance tends to produce artifacts in the UV-vis measurements. Besides this, it was elsewhere found that DOX interacts with MTT test solutions and thus produces artifacts in UV-vis measurements (Luis et al., 2019). Taking into account this issue, all the UV-vis measurements of the MTT test were referred to the baseline value of the different theoretically released DOX amounts dissolved in the same MTT stock solution. Statistical analysis was performed using Origin (Origin Lab Northampton, Ma). I performed a non-parametric Kruskall-Wallis test. Significance levels were set at $p < 0.05$. The box plots representation indicates the percentile 25-75 (box), the standard deviation (whiskers), the mean (square), and the 99% (x) of values. Asterisks above the plots indicate statistically significant differences.

4.2.3 Immunocytochemistry Analysis

To characterize the effect of the US on PCs, a wide field fluorescent microscope (Olympus IX51/TH4-200) and a confocal one (Leica DMIRE2) were used. Dextran-FITC was used to label the seventh layer of the PCs for shell visualization (Cf., Chapter 1 | 1.6.1.), both for non-biodegradable and biodegradable PCs. Moreover, the non-biodegradable capsules were initially filled with Fluo-Spheres™ to simulate the presence of DOX.

4.3 Results

After a brief introduction on the US parameters, this section will present the results obtained from the study of US mediated drug delivery on non-biodegradable capsules made with PSS/PAH and subsequently on biodegradables ones made with DEX/PLA obtained by LbL technique (Fig. 4.1a). In both cases the US effects on loaded or empty capsules and the results of the *in vitro* experiments will be described. Figures 4.1b-e show a representative images of capsules: (b) immediately after the $CaCo_3$ core is dissolved, (c) the fluorescent DEX-FITC staining in the shell, (d-e) and how they appear at the confocal microscope with both the shell and DOX load stained.

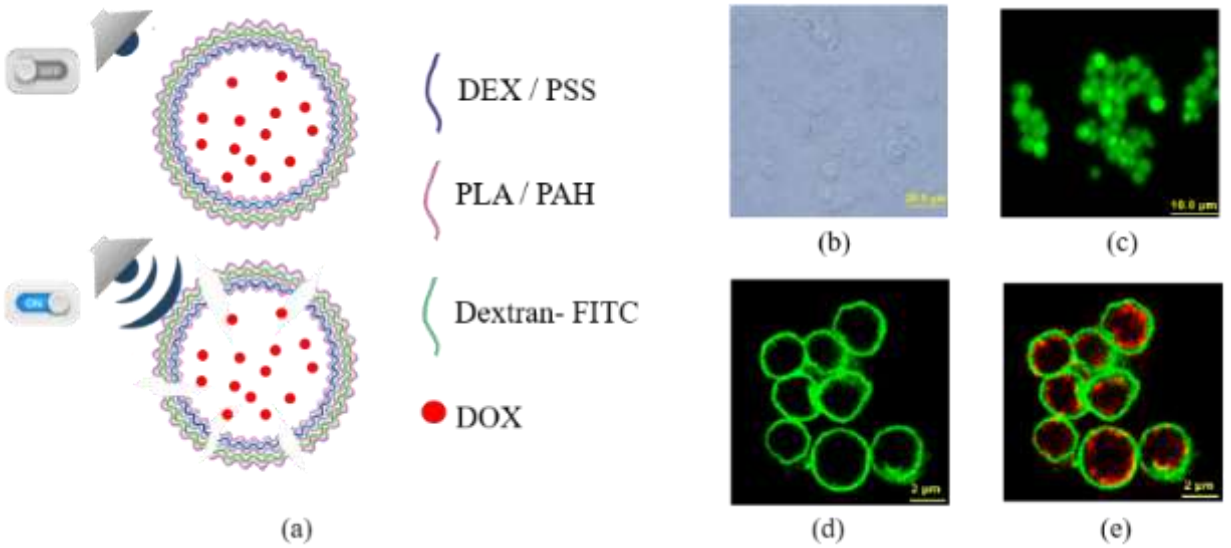

Figure 4.1: **(a)** *Ultrasound stimulation induces capsules breakage promoting the release of the encapsulated drug.* **(b)** *Phase contrast microscopy image of polyelectrolyte microcapsules in solution/adsorbed on glass.* **(c)** *Fluorescence image of polyelectrolyte microcapsules stained with FITC-dextran* **(d-e)** *confocal image: polyelectrolyte microcapsules with a FITC-dextran layer (green) and filled with DOX (red).*

4.3.1 Ultrasound parameters

US has been first characterized in terms of the generated pressure field (CF. Chapters 1 | 1.1.3) and temperature increase within the culture dishes where all experiments were performed. Fig. 4.2a shows the corresponding mechanical index (MI) value as a function of the nominal power density values of the US source. MI is dimensionless parameters related to acoustic intensity which is used to asses potentially harmful mechanical effects on cells and biological tissues (Cf., Chapter 1 | 1.1.1). I performed all experiments on capsules and cells with US intensities less or equal 1.5 W/cm2 that correspond to MI values below 1.9, the safe threshold. Figure 4.2b shows the temperature of the cell culture medium close to the cell culture substrate, over three minutes of pulsed US generation at 1.5W/cm2 intensity. In these conditions I observed an increase in temperature with a rate of around 0.2 °C/min after the first minute. This mild increase has no effect on the capsules; in fact, polymeric capsules change their permeability or are subject to breakage when the temperature is subjected to variations of some degrees, which can even reach 80°C (Delcea et al., 2011). Furthermore, in this case, the temperature rise is less than one; so,

keeping in mind that TI is implied by the ratio of ultrasound power to those that induce a temperature rise of one degree in the tissue (Cf., Chapter 1 | 1.1.1.), and keeping in mind that the FDA set the safe threshold at six, I may assume that my system is a safe system.

4.3.2 Non-biodegradable PCs

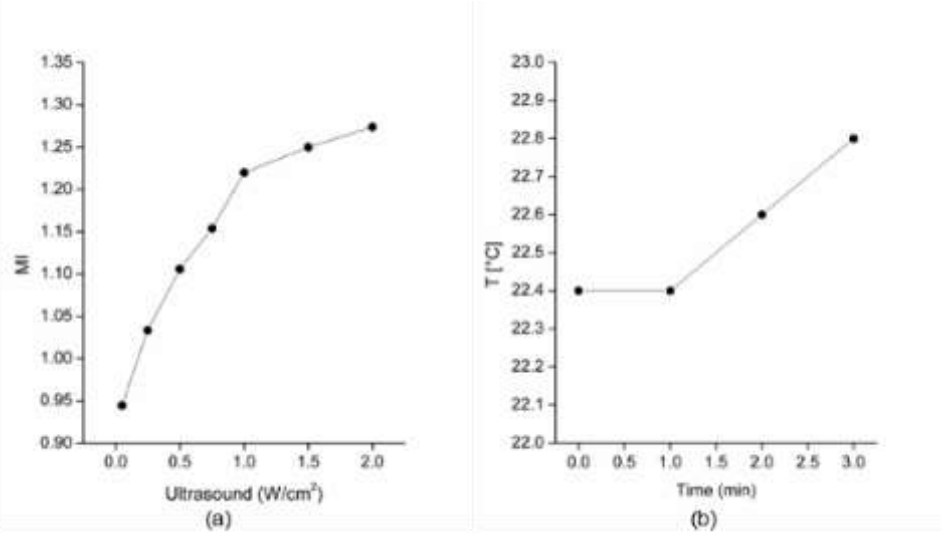

Figure 4.2: **(a)** *Measured mechanical index (MI) as a function of the source power density.* ***(b)*** *Temperature increase of the solution over time by the US stimulation at 1.5W/cm² power density*

After making the non-biodegradable PCs, I characterized the effects of US stimulation on this type of capsules. In this case, a 1.5W / cm2 stimulus was used for 5 minutes because previous research found that lower intensities had no effect on this type of capsule.

I first characterized empty and FluoSpheres™ filled microcapsules, with fluorescence and confocal microscope in order to check for breakage, and I observe two completely different behaviours. In Figure 4.3a it is possible to observe that empty microcapsules, when sonicated with US protocol, do not break but shrink themselves, decreasing their areas in a significant way ($p = 0.01$). Figure 4.3b highlight this result. On the contrary, filled microcapsules tend to break when sonicated (Fig. 4.3c), letting the internal substances get out. This difference in behavior is probably due to the presence of the support given by the nanoparticles inside the microcapsules or to its absence. Once the experimental protocol to break microcapsules with US was established, the PCs were filled with the DOX. Microcapsules filled with DOX with the efficiency of encapsulation (EE%) of about 50% were used to evaluate the quantity of released DOX after US stimulation, using UV-vis spectrophotometry. Figure 4.3d shows the increase of DOX

concentration into the solution with sonicated microcapsules compared to solution with non-sonicated ones.

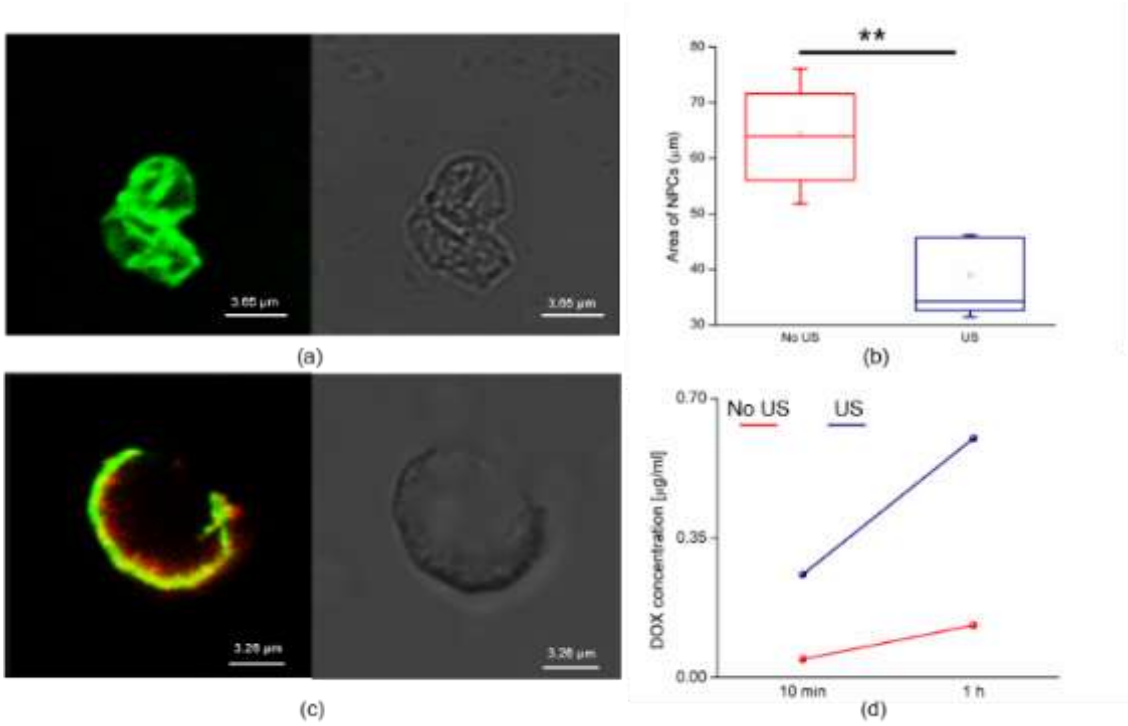

Figure 4.3: **(a)** *confocal images of empty PCs after US exposure; (b) graphical representation of the significative difference between the areas of not sonicated (No US) and sonicated empty PCs (US) (p = 0.01); (c) confocal images of FluoSpheres™ filled microcapsules after US exposure; (d) DOX concentrations of control and sonicated samples to calculate the DOX released by the PCs with and without the US stimulation*

The achieved results show that even if US treatment has an immediate effect, the release continues also in the subsequent time. Finally, the system was tested directly on MCF7-cells, and the MTT assay was carried out to characterize the in vitro cytotoxicity of the system. Cell viability (CV%) was estimated 24 h after the stimulation. Results are shown in figure 4.4a. For empty PCs with (blue box, EC + US) and without (green box, EC) US stimulation, CV% remained very high when compared with the control sample (red box). This result means that US does not cause damages to cells. However, the presence of synthetic material in the cell solution for 24 h may explain the slight morality. Microcapsules filled with DOX and stimulated at 1.5 W/cm2 for 5 minutes show a significant decrease in CV%, which means that DOX is released slowly, allowing cells to absorb it, thus causing cell degradation. This percentage value could rise by increasing the administration of the capsules number and therefore the concentration of DOX that would be released, while the power of ultrasound should not increase to avoid thermal effects. For all the experiments microscopy images were acquired to qualitatively check cell mortality (Fig 4.4b). Therefore, the obtained results overall confirm that US treatment, in conditions that respect biocompatible mechanical index values, has an effect on the microcapsules system and triggers the DOX release by breakage in a controlled fashion.

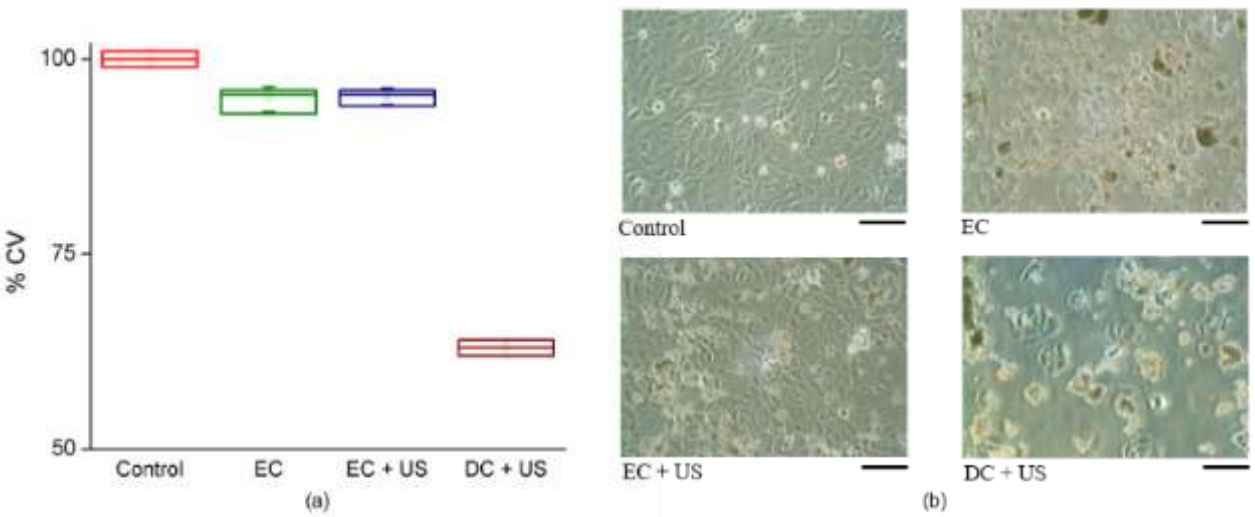

Figure 4.4: *Results from cell viability MTT assays after 24h from plating* **(a)** *Boxplot of MCF7 cell viability without any treatment (control), incubated with empty capsules (EC), with exposed to US empty capsules (EC+US) and exposed to US Dox-filled capsules (DC).* **(b)** *Phase contrast microscopy images of the samples tested for cell viability; scale bar: 100 μm.*

4.3.3 Biodegradable PCs

Following the validation of the US stimulation method for drug delivery on PSS/PAH capsules, the experiment was repeated on capsules made from biopolymers, namely DEX and PLA. As a first step, I used confocal microscopy to characterize the effects of US exposure on the integrity of DOX-loaded PCs. The first results showed that an US stimulus at 1.5 W / cm^2 for 5 minutes resulted in the total disintegration of the PCs. This behavior is likely due to the biopolymers' increased brittleness. Following several experiments, I determined that it was reasonable to reduce the ultrasound exposure time to three minutes and observe what happened at various intensities. Images in figure 4.5a show non-sonicated NPSs and sonicated ones: many PCs, after US exposure, present holes and breaks in the shell, which cause DOX release. One can observe that such release is only partial since there is not a complete release of the molecules due to the net positive charge of DOX, which promotes its interaction with the charged multilayer, as already observed in the literature for charged molecules (Pastorino et al., 2011). I evaluated the percentage of DOX-loaded PCs that appears broken after US exposure, as a function of the US intensity (Fig. 4.5b). Such values were assessed by examining an average of 70 capsules for three different samples under the same stimulation protocol. At power densities below 0.25 W/cm^2 I obtained rather scattered results with percentage values below 10%. At the higher limit, I observed an average of 73% broken capsules for 1.19 MPa US intensity which did not increase significantly when reaching the maximum power density of 1 W/cm^2.

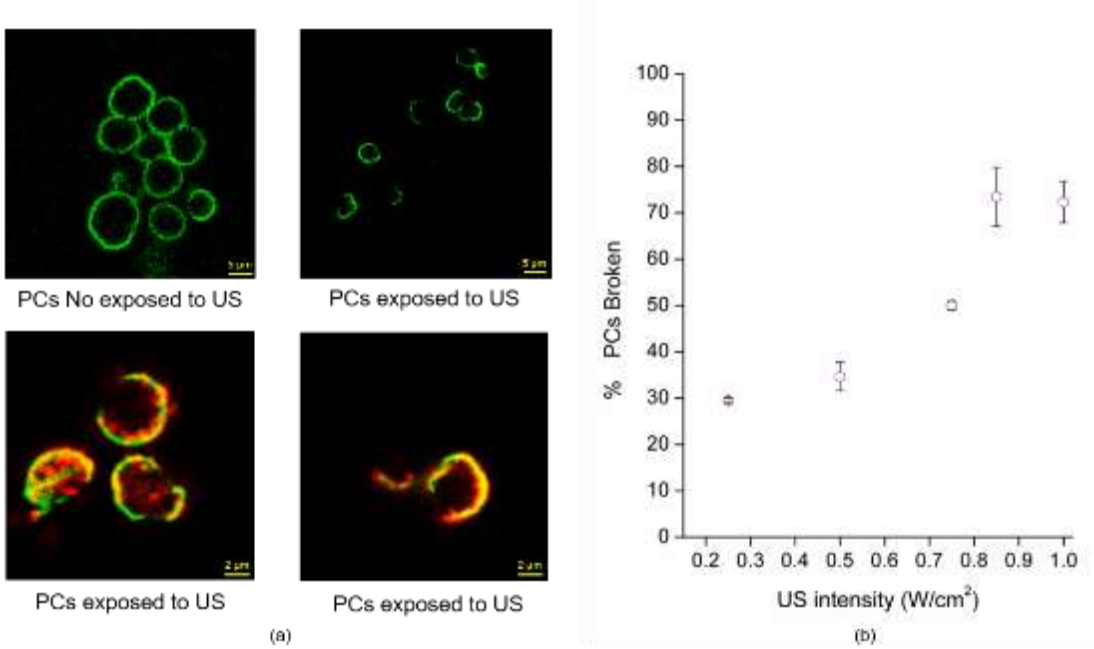

Figure 4.5: **(a)** *Confocal images of PCs before and after US exposure (red, DOX and green, layer)* **(b)** *Percentage of broken DOX-loaded PCs as a function of US intensity. Values are calculated over three different samples, considering for each sample 70 PCs.*

Then, I tested the US-mediated drug delivery protocol on MCF7 cells; MTT assay was conducted to characterize in vitro cytotoxicity. Cell viability (CV%) was measured 24 h after stimulation and the cell sample (without PCs or ultrasound stimulation) was used as control (Fig.s 4.6a, 4.6b, 4.6c red box, Cell). First, I evaluated whether unloaded PCs or the US alone were able to produce a cytotoxic effect on cells. The unloaded PCs led to a slight decrease in cell viability by 2% (Fig. 4.6a, green box, EC). This behavior can be explained taking into account both the sedimentation of PCs onto cells, which hinders cell duplication, and onto the cell culture substrate, which determines a competition for space. These factors were previously demonstrated to be responsible for the viability decrease of cells (Pastorino et al., 2009). To evaluate the US effect, the higher intensity was tested, and a 3% CV% decrease was observed (Fig. 4.6a, blue box, US HG). It is worth noting that the US transducer was immersed in the solution during the stimulation, so there may be a slightly negative effect on cell viability. At this point, I evaluated the effect of the stimulated DOX loaded PCs, comparing the viability for cells exposed to DOX loaded PCs (DC), DOX loaded PCs and low-intensity US stimulation (0.25 W/cm2, DC + LW US), and DOX loaded PCs and high-intensity US stimulation (1 W/cm2, DC + HG US). The DC induced cell mortality compared to the control (Fig. 4.6b, brown box); this has probably been due to DOX spontaneous release from PCs shell (Boi et al., 2020). However, the DOX loaded PCs with US stimulation induced higher cell mortality, bringing the percentage to 68% and 27% for low and high-intensity stimulation, respectively (Fig. 4.6b, dark grey and grey boxes). Ultrasound can causes transient pores on cell membranes (Deng et al., 2004), so we evaluated whether they contributed in triggering DOX internalization (Fig. 4.6c). The MTT assay was repeated using free DOX. The amount of free DOX we used was equal to the calculated DOX released from the

sonicated PCs. The percentage of broken PCs was 30% when 0.25 W/cm2 US was used, so the corresponding free DOX was added to the Petri dish with MCF7 cells (i.e. 2.5 μg/ml). Compared to the control, free DOX decreased the CV% to 63% (Fig. 4.6c, purple box). This value decreased to 54% when cells with the same amount of DOX where exposed to US at an 0.25W/cm2 intensity (Fig. 4.6c, pink box). The same experiment was carried out at the intensity of 1W/cm2 for US stimulation and at a concentration of free DOX of 5.6 μg/ml, corresponding to the DOX released from about 70% of broken PCs. This concentration of free DOX without US stimulation induced higher cell mortality, leading to 31% CV% (Fig. 4.6c, brown box). The same value decreased by 15% when the MCF7 cells were stimulated by the US at 1W/m2 in the presence of 5.6 μg/ml DOX (Fig. 4.6c, green box). I interpret this behavior as an indication that US stimulation triggered DOX internalization by cells. Comparing figures 4.6b and 4.6c, it can be observed that the CV% for cells exposed to DOX-PCs and to the low and high US is similar to the respective free-DOX value without the US. These CV% values may be justified if it is considered that the broken PCs catch part of the drugs on their shell, so the internalization of this amount of DOX required more time with respect to the DOX-free. For all the experiments microscopy images were acquired to qualitatively check cell mortality (Fig. 4.6d).

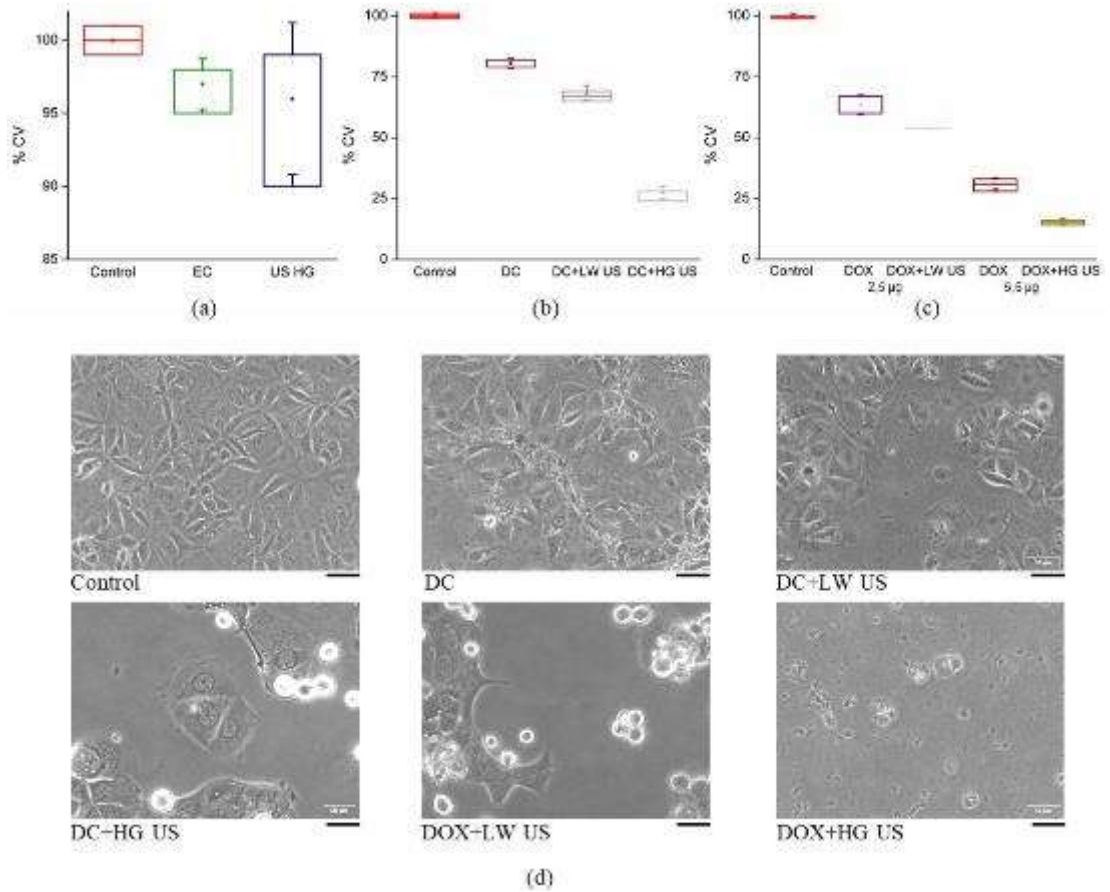

Figure 4.6: *Results from cell viability MTT assays after 24h from plating* **(a)** *Box-plot of MCF7 cell viability without any treatment (control), incubated with empty capsules (EC), and exposed to US protocol at max intensity (US HG).* **(b)** *MCF7 cell viability after 24h in culture dishes without any treatment (control), incubated with capsules loaded with Doxorubicin (DC), and exposed to US at 0.25w/cm2 intensity (DC + LW US) and 1W/cm2 intensity (DC + HG US).* **(c)** *MCF7 cell viability after 24h in culture dishes without any treatment (control), incubated with 2.5 μg or 5.6 μg of free Dox , and exposed to US at 0.25w/cm2 or 1W/cm2 intensity (DOX + LW US and DOX + HG US, respectively).* **(d)** *Phase contrast microscopy images of the samples tested for cell viability; scale bar: 50 μm.*

4.4 Conclusions

Two types of stimuli can be used in the development of localized drug delivery systems: endogenous stimuli and exogenous stimuli. The former enable controlled release over time and space by using, i.e. pH changes, reducing enzymes, or an oxidizing environment, while exogenous acoustic, magnetic, electric, or light stimuli can be applied in a controlled way to induce drug release. The necessity for drug administration at specific instants or time intervals require the development of pulsatile delivery systems, i.e. systems or devices capable of holding the drug in the absence of the stimulus and releasing it otherwise.

The focus of my PhD work is on low intensity US technology since it is a mechanical stimulation which can virtually reach any area in the human body with well-established safety studies in human applications (US imaging is consider a safe procedure even in critical situation such as in pregnant women).

I believe that US is a promising method for enhancing non-invasively the targeted delivery of therapeutic agents. To my knowledge, no study has previously described drug release from polyelectrolyte microcapsules (DEX-PLA) using US waves compliant with the safety limitations imposed to be defined as safe and biocompatible. I have shown that with the protocol presented, microcapsules filled with a model drug (DOX) can be remotely controlled, releasing the drug while under US stimulation. In addition, I have shown that the percentage of breakage capsules is related to the US intensity, which may allow control of the quantity of the drug released. Interestingly, experiments where US stimulation was coupled with administration of free DOX demonstrated that US alone can help drug internalization by cells. Finally, the stability over time of the DOX capsules without US exposure demonstrates that the system will be capable of exactly responding to the need for a pulsatile delivery system, as the capsules alone are capable of limiting the amount of drug released in the absence of stimulation. The presented results overcome the current limitations associated with US-mediated drug delivery that exploit processes such as cavitation or sonoporation that could lead to irreversible tissue damage and those requiring microbubbles in association.

References

Arora, S., Ali, J., Ahuja, A., Baboota, S., & Qureshi, J. (2006). Pulsatile drug delivery systems: An approach for controlled drug delivery. In *Indian Journal of Pharmaceutical Sciences* (Vol. 68, Issue 3, pp. 295–300). Medknow Publications and Media Pvt. Ltd. https://doi.org/10.4103/0250-474x.26655

Boi, S., Rouatbi, N., Dellacasa, E., Di Lisa, D., Bianchini, P., Monticelli, O., & Pastorino, L. (2020). Alginate microbeads with internal microvoids for the sustained release of drugs. *International Journal of Biological Macromolecules*, *156*, 454–461. https://doi.org/10.1016/j.ijbiomac.2020.04.083

Delcea, M., Möhwald, H., & Skirtach, A. G. (2011). Stimuli-responsive LbL capsules and nanoshells for drug delivery. In *Advanced Drug Delivery Reviews* (Vol. 63, Issue 9, pp. 730–747). Elsevier. https://doi.org/10.1016/j.addr.2011.03.010

Deng, C. X., Sieling, F., Pan, H., & Cui, J. (2004). Ultrasound-induced cell membrane porosity. *Ultrasound in Medicine and Biology*, *30*(4), 519–526. https://doi.org/10.1016/j.ultrasmedbio.2004.01.005

Luis, C., Castaño-Guerrero, Y., Soares, R., Sales, G., & Fernandes, R. (2019). Avoiding the interference of doxorubicin with mtt measurements on the mcf-7 breast cancer cell line. *Methods and Protocols*, *2*(2), 1–5. https://doi.org/10.3390/mps2020029

Missirlis, D., Kawamura, R., Tirelli, N., & Hubbell, J. A. (2006). Doxorubicin encapsulation and diffusional release from stable, polymeric, hydrogel nanoparticles. *European Journal of Pharmaceutical Sciences*, *29*(2), 120–129. https://doi.org/10.1016/j.ejps.2006.06.003

Pastorino, L., Erokhina, S., Caneva-Soumetz, F., & Ruggiero, C. (2009). Paclitaxel-containing nano-engineered polymeric capsules towards cancer therapy. *Journal of Nanoscience and Nanotechnology*, *9*(11), 6753–6759. https://doi.org/10.1166/jnn.2009.1580

Pastorino, L., Erokhina, S., Soumetz, F. C., Bianchini, P., Konovalov, O., Diaspro, A., Ruggiero, C., & Erokhin, V. (2011). Collagen containing microcapsules: Smart containers for disease controlled therapy. *Journal of Colloid and Interface Science*, *357*(1), 56–62. https://doi.org/10.1016/j.jcis.2011.02.010

Ricotti, L., Cafarelli, A., Iacovacci, V., Vannozzi, L., & Menciassi, A. (2015). Advanced Micro-Nano-Bio Systems for Future Targeted Therapies. *Current Nanoscience*, *11*(2), 144–160. https://doi.org/10.2174/1573413710666141114221246

Chapter 5

Interconnected and heterogeneous 3D cultures

5.1 Abstract

All the studies described so far have been developed *in vitro* on cellular models that do not perfectly mimic the real environment and conditions present *in vivo*. Hence, the need of developing an improved *in vitro* model that can also represent an effective testbed for the characterization of neurostimulation and drug delivery strategies, such as those mediated by ultrasound (cf. Chapters 2 and 4). With this target I am going to describe, in this chapter what I developed to design interconnected (i.e., modular) heterogeneous (cortical-hippocampal) neuronal cultures with a three-dimensional (3D) connectivity and to record their electrophysiological activity using Micro-Electrode Arrays (MEAs). In this perspective, a two-compartment polymeric mask for the segregation of different neuronal populations (cortex and hippocampus) was coupled to the MEA surface. Glass microbeads were used as a scaffold to mimic the 3D brain micro-architecture. I built a fully functional heterogeneous 3D neuronal network. From an electrophysiological point of view, I found that the heterogeneity induces a global increase of the activity rate, while the 3D connectivity modulates the duration and the organization of the bursting activity. *In vivo*, studies of network dynamics and interactions between neuronal populations are often time-consuming, low-throughput, complex, and suffer from low reproducibility. On the other hand, most of the commonly used *in vitro* brain models are too simplified and thus far from the *in vivo* situation. The achieved results demonstrate the feasibility to build a more realistic and controllable experimental *in vitro* model of interconnected brain regions on-a-chip whose applications may have impacts on the study of neurological disorders that impair the connectivity between brain areas (e.g., Parkinson disease).

All the results presented below have been published in: Pisano et al., et al 2020 J. Neural Eng. 17 056044.

5.2 Experimental Protocol and Analysis

5.2.1 Experimental protocol.

Cortical and hippocampal neurons were plated into a PDMS mask, which was used to define two rectangular compartments over the MEA-4Q chips (C.f., Chapters 1 | 1.3).
The dataset used in this work was composed of measurements from both 2D and 3D cells cultures as well as homogeneous and heterogeneous networks (C.f., Chapter 1 | 1.4.2 and 1.4.3). Briefly, we plated cortical and hippocampal cells onto the active area of the MEA defined by a PDMS mask at the final density of 1'500 cell/mm^2 and 1'300 cell/mm^2 respectively. These values led to a final 3D density of about 90·103 cells/mm^3 and 80·103 cell/mm3 for the cortical and hippocampal cell, respectively, values close to the density of the *in vivo* mouse brain cortex of 92·103 cells/mm3 (Schüz & Palm, 1989). In detail, besides the final configuration of a 3D cortical-hippocampal (Cx-Hp$_{3D}$) network, the following controls have been tested: 2D homogeneous cortical-cortical (Cx-Cx$_{2D}$) and hippocampal-hippocampal (Hp-Hp$_{2D}$) assemblies and 2D heterogeneous cortical-hippocampal (Cx-Hp$_{2D}$). The 3D controls were homogeneous cortical-cortical (Cx-Cx$_{3D}$) and hippocampal-hippocampal (Hp-Hp$_{3D}$) networks. For each configuration, I recorded 20 min of activity from n = 5 MEAs. The n = 30 networks were derived from seven dissections. All the recordings have been performed after 21 days *in vitro* (DIVs), which corresponds to a mature stage of development (Bardy et al., 2015). Spontaneous electrophysiological activity from neuronal networks was recorded using a commercial MEA2100 system (MCS).

5.2.2 Data Analysis

The analysis were performed in Matlab (The Mathworks, Natik, US) and all the details were reported in Appendix A. Statistical analysis was performed using Origin (Origin Lab Northampton, Ma). Since data do not follow a normal distribution (evaluated by the Kolmogorov-Smirnov normality test), we performed a non-parametric Kruskall-Wallis test. Significance levels were set at $p < 0.05$. The box plots representation indicates the percentile 25-75 (box), the standard deviation (whiskers), the mean (square), and the median (line) values. Asterisks above the plots indicate statistically significant differences and are color-coded to highlight differences due to the three-dimensionality (gray), and cell composition (black).

5.2.3 Immunocytochemistry Analysis

In order to verify the 3D structure and the interactions between the populations seeded in the two compartments through the microchannels, the immunofluorescence technique was used to gather structural information. Cell cultures were fixed in 4% paraformaldehyde in Phosphate Buffer Solution (PBS), pH 7.4 for 15 minutes at room temperature. Permeabilization was achieved with PBS containing 0.1% Triton-X100 for 15 min at room temperature and non-specific binding of

antibodies was blocked with incubation of 40 min in a blocking buffer solution consisted of PBS, 0.3% BSA (bovine serum albumin, Sigma-Aldrich) and 0.5% FBS (fetal bovine serum, Sigma-Aldrich). Cultures were incubated with primary antibody diluted in PBS Blocking buffer for 2 hours at room temperature. The following primary antibodies were used: Tau (mouse monoclonal 1:500, Synaptic System), NeuN (mouse monoclonal 1:500, Synaptic System) and MAP2 (rabbit polyclonal 1:500, Synaptic System). Afterwards, cultures were rinsed three times with PBS and finally exposed for 40 minutes at room temperature to the secondary antibodies: Alexa Fluor 488 (1:700, Invitrogen) and Alexa Fluor 549 (1:1000, Invitrogen) Goat anti-mouse or Goat anti-rabbit. Images were acquired with fluorescence equipped microscopes (Olympus BX-51 and Olympus IX-70) using a CCD camera (Orca ER II, Hamamatsu) and IC Image software (Hamamatsu). Fiji software (Schindelin et al., 2012) was used for image analysis.

5.3 Results

In this Section, results from the recordings of cortical, hippocampal and cortical-hippocampal networks organized in 2D and 3D are reported. In Sect. 5.3.1, immunofluorescence images of homogeneous (i.e., only cortical or only hippocampal) heterogeneous (i.e., cortical and hippocampal) populations are presented. Sections 5.3.2 presents the intrinsic dynamics of the cortical and hippocampal networks (both in 2D and in 3D), while Section 5.3.3 reports the characterization of the cortical dynamics by separately investigating the role of hippocampal input and 3D configuration. Finally, Sections 5.3.4 and 5.3.5 deal with the effects on the cortical dynamics (spiking, bursting, and network bursting) when both heterogeneity and 3D coexist. All the results come from recordings performed after 21 DIVs with 60-channel MEAs organized in a 4Q-configuration. It is worth to notice that the electrophysiological activity of the entire 3D network is recorded only from the layer directly coupled to the active area of the planar MEA, over which a stack of other neurons (3D assembled) is built.

5.3.1 Imaging characterization

To get structural information about the 3D and the inter-compartment connectivity, we performed immunofluorescence techniques after cell fixation (Cf., Sec. 2.2.2). Figure 5.1A shows a close-up of a few cells cultured in 2D on a planar substrate: dendritic processes (green, MAP2) and neuronal cell bodies (blue, NeuN). Figure 5.1C presents a small cluster of microbeads wrapped in dendritic processes (green, MAP2). When organized in 3D, the shape of cell bodies is more round (Figure 5.1C) than the surface plated neurons (Figure 5.1A), in agreement with what has been previously observed (Frega et al., 2014; Wang et al., 2006). The count of the neurons and the microbeads, which make up the different layers, allowed to estimate a ratio of about 3:1. To visualize the structural inter-compartment connectivity, we used Anti-GABA (green) to stain GABA neurotransmitter and NeuN (red) to stain neuronal nuclear protein (Mao et al., 2016). Figure 5.1B shows the rich neurites arborization within cortical (bottom) and hippocampal (top) compartment demonstrating the formation of an intricate connectivity, and the crossing-over of the neurites between the compartments mediated by the microchannels: this morphological evidence well supports the modular connectivity of this biological preparation (Sporns & Betzel, 2016). Figure 5.1D shows a similar scenario in the 3D configuration, where we find the neuritic growth through individual microchannels at the level of the bottom layer, which is directly coupled to the active area of the MEA. Moreover, in both the 2D and 3D configuration, it can be observed that cell bodies do not cross the microchannels and remain segregated in the plating compartment. 3D networks (both homogeneous and heterogeneous) are constituted on average by 4/5 layers of self-assembled microbeads resulting a 3D network of a total height of about 160−200 μm. Figure 5.1E shows four different layers of a representative heterogeneous cortical-hippocampal 3D culture. Ideally, the distance between the layers is equal to the diameter of the microbeads (40 μm). The rich and intricate neuritic growth that develops between the microbeads and wraps around them, causes mechanical stresses and displacements between the beads of the

various layers which are not all involved in the same way by the extensions that propagate from different directions. These variations in position, albeit small, cause a certain variability of the height of the different layers.

5.3.2 Intrinsic cortical and hippocampal activity

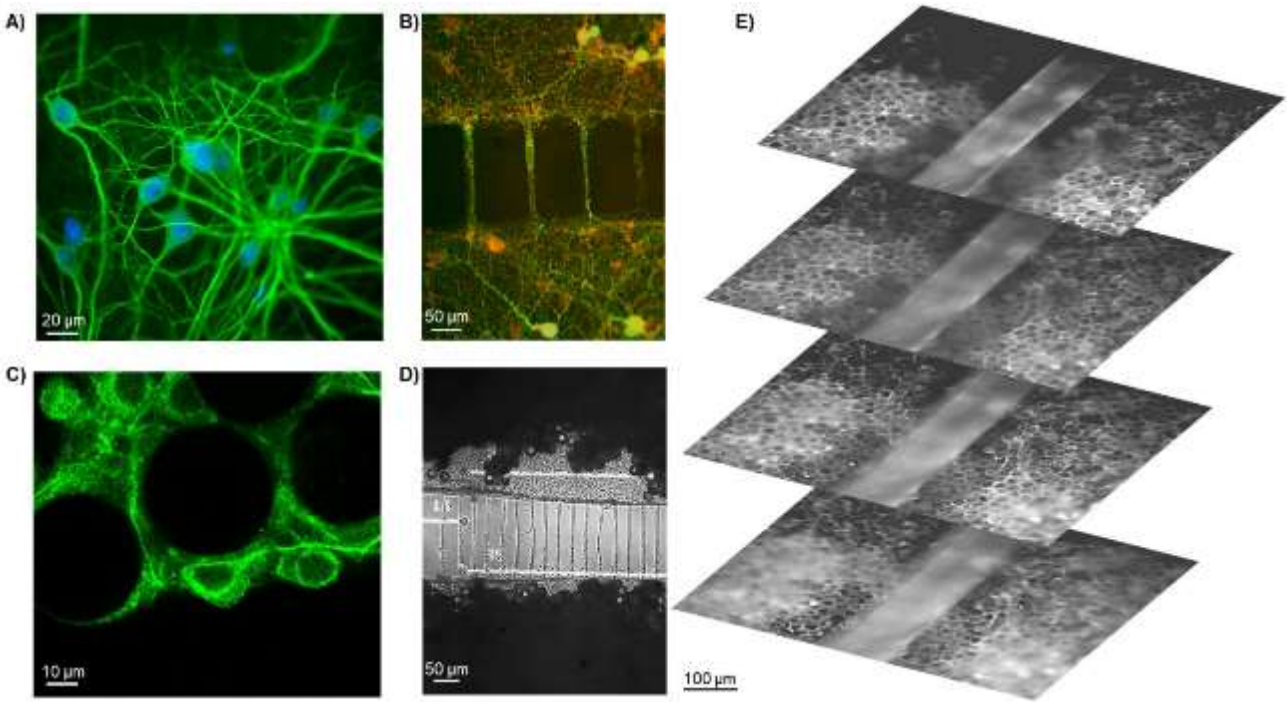

Figure 5.1: *Neuronal network images.* **(A)** *Mature 2D culture (21 DIV) on a planar substrate (green: MAP2 and blue: NeuN).* **(B)** *2D interconnected cortical-hippocampal culture at 21 DIV stained in order to visualize neuronal nuclear protein (NeuN, red) and GABA neurotransmitter (green: Anti-GABA); where the two markers overlap the cellular soma looks yellow-orange.* **(C)** *Mature 3D culture (21 DIV) on glass microbeads (green: MAP2).* **(D)** *3D interconnected cortical-hippocampal culture at 21 DIV on MEA. In the middle: the neurites across the microchannels. On the sides: neurons coupled to the glass microbeads.* **(E)** *Different layers of 3D heterogeneous culture: each stack is relative to one layer.*

Firstly, I investigated the electrophysiological variations when two interconnected homogeneous cortical and hippocampal populations are organized in a 2D or 3D configuration by recording their spontaneous activity. Among the parameters characterizing the electrophysiological activity (Cf., Appendix A), three bursting features mainly differentiate the two populations: MBR, burst amplitude (SpikesXBurst), and percentage of random spiking activity. MBR is higher in hippocampal than cortical networks (Figure 5.2B, MBR_{Hp} = 20 ± 4 bursts/min (mean ± std), p = 0.009 vs. MBR_{Cx} = 8.61 ± 3 bursts/min). Still, the cortical bursting activity is characterized by events with a higher number of spikes (Figure 5.2C, $SpikesXBurst_{Cx}$ = 24 ± 4 vs. $SpikesXBurst_{Hp}$ = 9.84 ± 1, p=0.009), similarly to the results achieved in (Soscia et al., 2017). Moreover, cortical spike trains display a more "packed activity" than hippocampal ones, as the lower percentage of random spike suggests (Figure 5.2E, $\%RandomSpikes_{Cx}$ = 14.68 ± 6 vs. $\%RandomSpikes_{Hp}$ = 36 ± 9, p= 0.009). Finally, though hippocampal bursts are likely shorter than cortical ones, no significant differences can be found (Figure 5.2C, BD_{Cx} = 200.26 ± 66 ms vs. BD_{Hp} = 139.21 ±

41 ms, p = 0.07). The MFR and IBI also do not show significant differences (p = 0.6 and p = 0.3, respectively) between the two neuronal networks (Figures 5.2A and 5.2D).

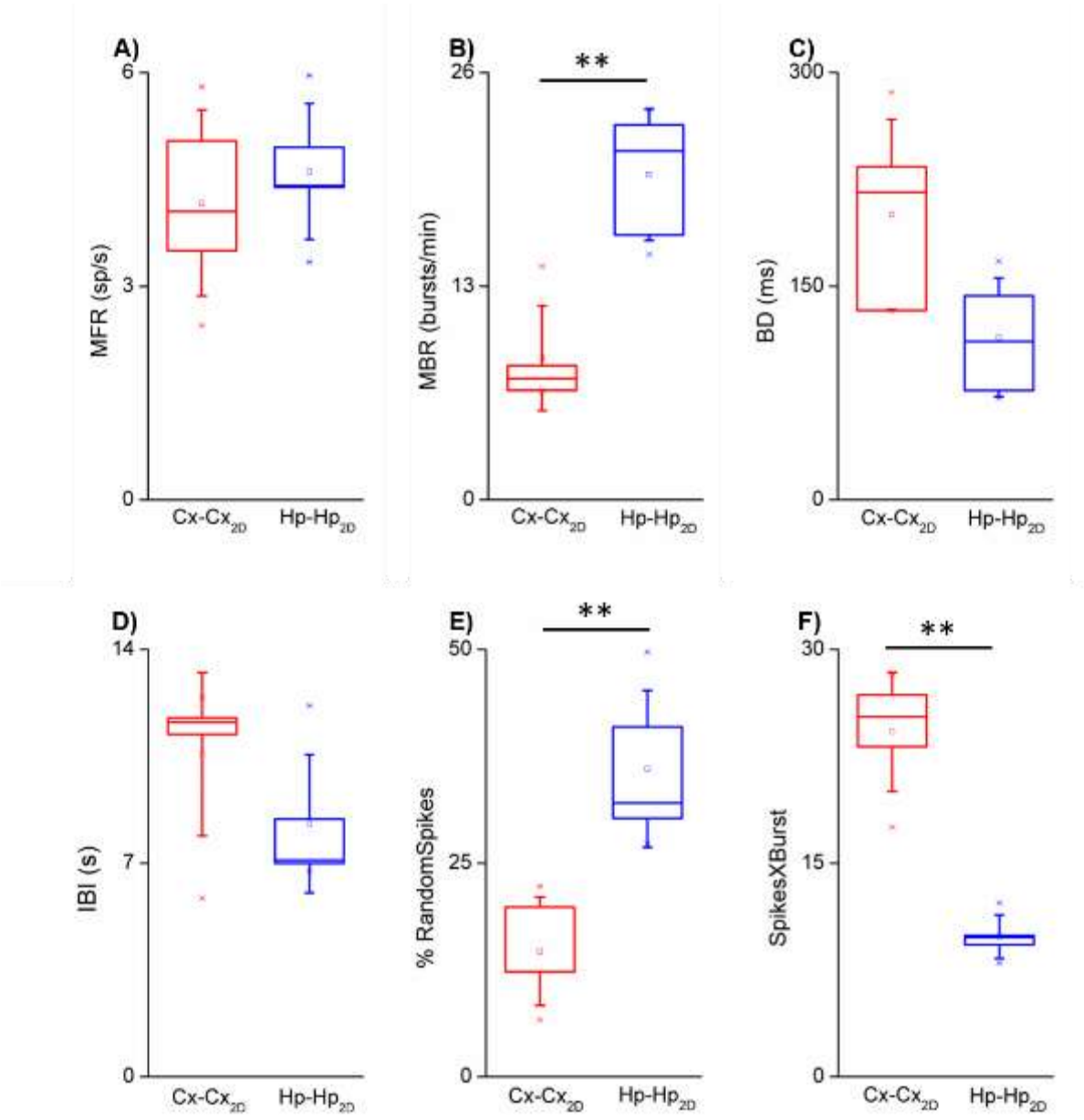

Figure 5.2: *Spiking and bursting activity characterization of 2D homogeneous cortical (Cx-Cx2D , red) and hippocampal (Hp-Hp2D, blue) cultures.* **(A)** *mean firing rate (MFR), p = 0.6;* **(B)** *mean bursting rate (MBR), p = 0.009;* **(C)** *burst duration (BD);* **(D)** *inter burst intervals (IBI), p = 0.3;* **(E)** *percentage random spikes (%RandomSpikes), p = 0.009;* **(F)** *spikes per burst (SpikesXBurst), p = 0.009;*

The same analysis was performed to evaluate possible differences in the electrophysiological activity when homogeneous cortical and hippocampal assemblies are organized in a 3D fashion (Figure 5.3). The differences between cortical and hippocampal activity observed in the 2D configuration are also maintained in 3D, suggesting an intrinsic natural firing pattern that each neuronal family has (Dauth et al., 2017). However, by carefully looking at Figure 5.3, it can be observed how such differences are more pronounced in the 3D configuration. Overall, the electrophysiological activity tends to be more packed in cortical than hippocampal networks, with

a higher spike number inside the burst (Figure 5.3F, $SpikesXBurst_{Cx}$ = 67 ± 22 vs. $SpikesXBurst_{Hp}$= 16 ± 3, p = 0.009) and a less random spiking activity (Figure 5.3E, % $RandomSpikes_{Cx}$ = 5.42 ± 3 vs. % $RandomSpikes_{Hp}$ = 21 ± 6 p = 0.009). However, the bursting hippocampal activity is higher than cortical one, as MBR box plots show (Figure 5.3B, MBR_{Cx} = 7.99 ± 2 bursts/min vs. MBR_{Hp} = 23.50 ± 13 bursts/min, p = 0.01). Indeed, the high values of spikes in the bursts of cortical network leads to a longer duration of the bursting events, as Figure 5.3C shows. In this case too, the MFR and IBI do not show statistically significant differences (p = 0.9 and p = 0.07, respectively) between the two neuronal networks (Figures 5.3A and 5.3D).

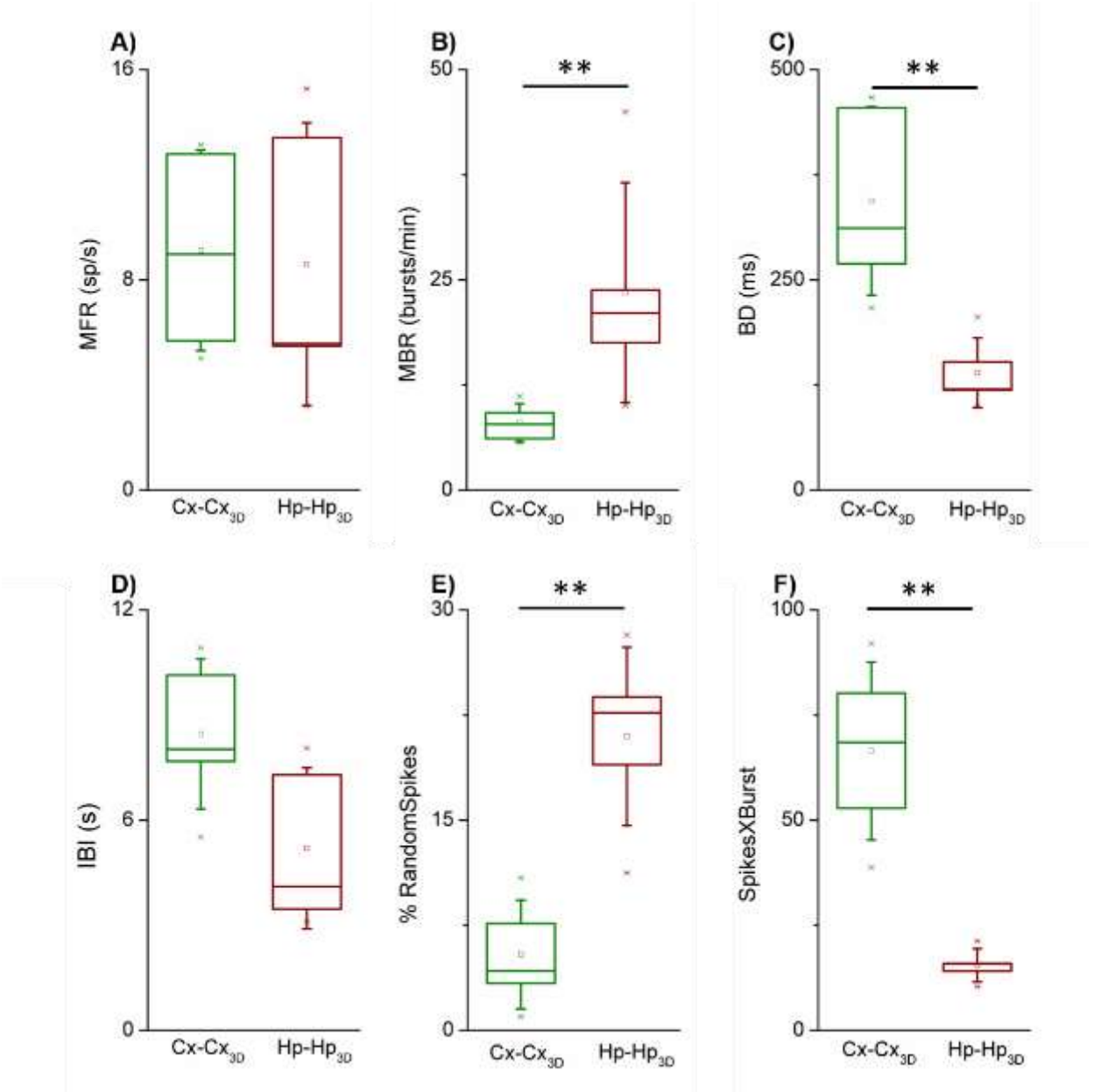

Figure 5.3 *Spiking and bursting activity characterization of 3D homogeneous cortical (Cx-Cx3D , red) and hippocampal (Hp-Hp3D , blue) cultures.* **(A)** *mean firing rate (MFR), p = 0.9;* **(B)** *mean bursting rate (MBR), p = 0.01;* **(C)** *burst duration (BD), p=0.009;* **(D)** *inter burst intervals (IBI), p = 0.07;* **(E)** *percentage random spikes (%RandomSpikes), p = 0.009;* **(F)** *spikes per burst (SpikesXBurst), p = 0.009;*

5.3.3 Cortical activity in heterogeneous or 3D configuration

The electrophysiological activity of a 2D homogeneous culture is merely a partial view of the actual in vivo conditions, where the activity is influenced by the presence of other neuronal families and a 3D structure. Consequently, we evaluated the role of 3D connectivity and hippocampal inputs on the cortical dynamics comparing the 2D homogeneous cortical cultures with both 2D heterogeneous culture and 3D homogeneous cortical cultures.

The presence of hippocampal neurons induces a pronounced increase of the spiking (+184%) and bursting (+178%) activity in the cortex (Figure 5.4A and 5.4B, black box plots) which follows the typical hippocampal activity (Figure 5.2A), suggesting the role of the hippocampal neurons as master. On the other hand, if the 3D-configuration does not induce a significant variation of the bursting rate in the cortical population (Figure 5.4B, green box plots, $p = 0.7$), it strongly increases the spiking rate (+118%, Figure 5.4A, green box plots). It is worth to notice how the effect induced on the MFR by the 3D configuration implies a larger variability than the presence only of an input coming from another brain region: the 25^{th} and 75^{th} percentiles relative to the MFR show values of $P_{0.25} = 5.69$ and $P_{0.75} = 12.8$ in the case of 3D cortical cultures, while, when coupled to hippocampal neurons, MFR values are $P_{0.25} = 11.74$ and $P_{0.75} = 11.9$. (Figure 5.4A and 5.4B), in agreement with (Frega et al., 2014): a more dense connectivity induces of the emergence of more dynamical states than those in the 2D arrangement.

The distribution of the random spiking activity was also evaluated: both the presence of hippocampal inputs and the 3D arrangement promote a decrease of the random spiking activity, as well as the increase of the number of spikes per burst (Figure 5.4C and 5.4D). The changes induced by the 3D architecture (%RandomSpikes: -64%, SpikesXBurst: +176%) are stronger than the ones induced by the hippocampal population (%RandomSpikes: -25%, SpikesXBurst: +14%): 3D configuration leads an increase in the cortical BD (+71%, Figure 5.4E), with a respective decrease in the cortical IBI value (-21%, Figure 5.4F). Contrariwise, in the heterogeneous configuration, the cortex shows BD values not statistically different to control ones ($p = 0.6$, Figure 5.4E) with a related decrease in IBI (-64%, Figure 5.4F), correlated to the increase in the bursting rate (Figure 5.4B).

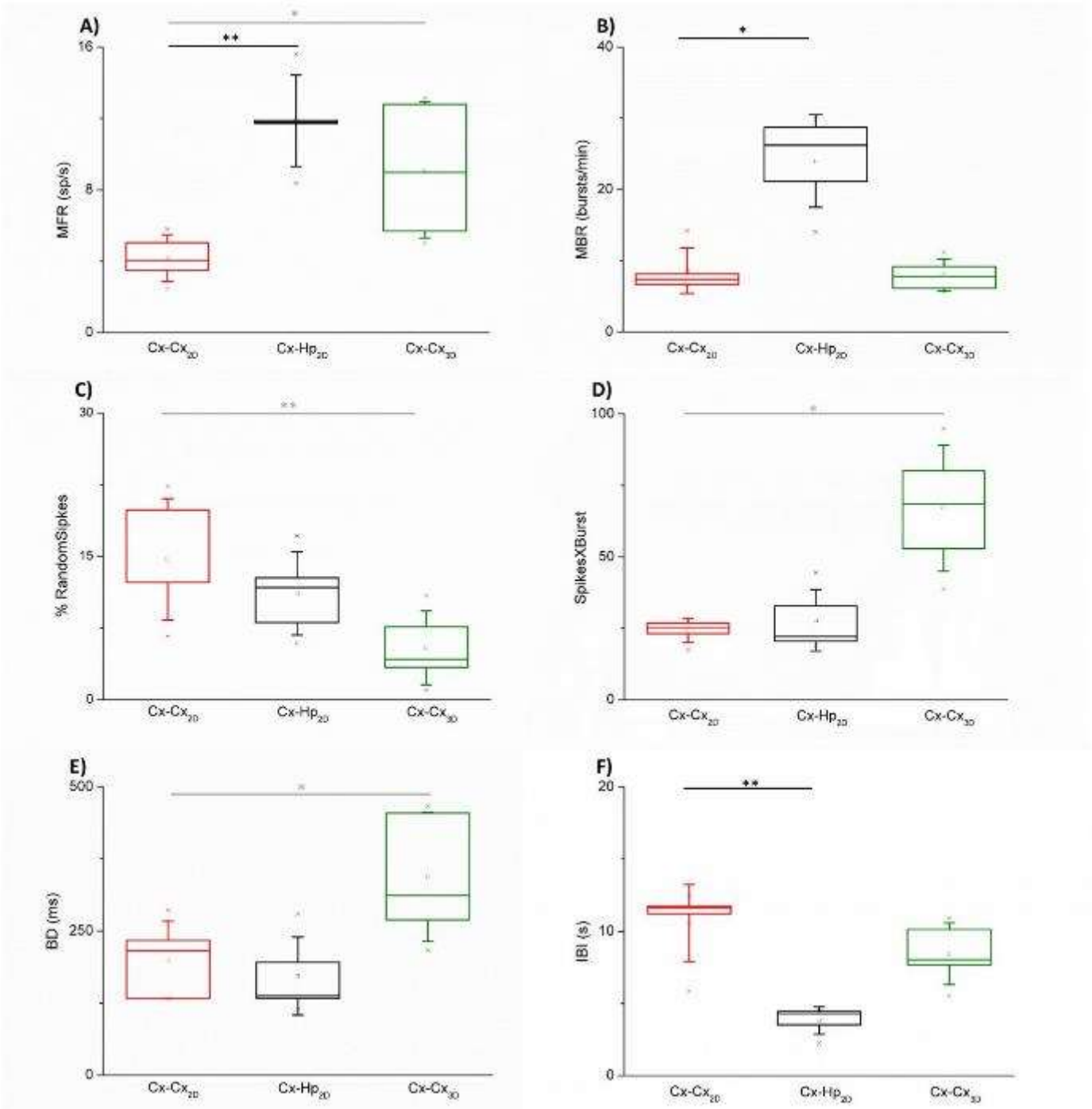

Figure 5.4: *Comparison of the spiking and bursting features of the different experimental configurations: 2D homogeneous cortical (Cx-Cx2D , red), 2D heterogeneous (Cx-Hp2D black), and 3D cortical (Cx-Cx3D , green) cultures.* **(A)** *Mean Firing Rate (Cx-Cx2D vs. Cx-Hp2D : p = 0.009; Cx-Cx2D vs. Cx-Cx3D : p = 0.04).* **(B)** *Mean Bursting Rate (Cx-Cx2D vs. Cx-Hp2D : p = 0.01).* **(C)** *Percentage of random spikes (Cx-Cx2D vs. Cx-Cx3D : p = 0.02).* **(D)** *Spikes per burst (Cx-Cx2D vs. Cx-Cx3D : p = 0.009).* **(E)** *Burst Duration (Cx-Cx2D vs. Cx-Cx3D : p = 0.04). (F) Inter Burst Intervals (Cx-Cx2D vs. Cx-Hp2D : p = 0.009).*

5.3.4 Cortical activity in heterogeneous and 3D configuration

Finally, we investigated the changes induced in the cortical electrophysiological activity when both heterogeneity and the 3D structure are introduced. For this analysis, 2D heterogeneous and 3D homogeneous configurations are considered as controls, whose effects on the cortical network activity have already been escribed (Cf., Sec., 5.3.3).

Moving from a 2D to a 3D heterogeneous configuration, a disruptive decrease of the spiking and bursting rate (FR: Cx-Hp$_{2D}$ = 11.88 ± 2 sp/s vs. Cx-Hp$_{3D}$ = 3.09 ± 1 sp/s, p = 0.009 and MBR: Cx-Hp$_{2D}$ = 24 ± 6 bursts/min vs. Cx-Hp$_{3D}$ = 10 ± 2 bursts/min, p = 0.009) can be appreciated from the radar plot of Figure 5.5A (grey shadow). The cortical bursting activity in the 3D configuration presents slightly shorter bursts than the one in 2D (p = 0.4), with a consequent decrease in the number of spikes per burst (SpikesXBurst: Cx-Hp$_{2D}$ = 27.79 ± 10 vs. Cx-Hp$_{3D}$ = 13.56 ± 5, p = 0.01). Such values induce an increase in the IBI (IBI: Cx-Hp$_{2D}$ = 3.81 ± 0.9 s vs. Cx-Hp$_{3D}$ = 12.96 ± 2 s, p = 0.009) and in the percentage of random spiking activity (%RandomSpikes: Cx-Hp$_{2D}$ = 11.12 ± 4 vs. Cx-Hp$_{3D}$ = 29.26 ± 10, p = 0.009).

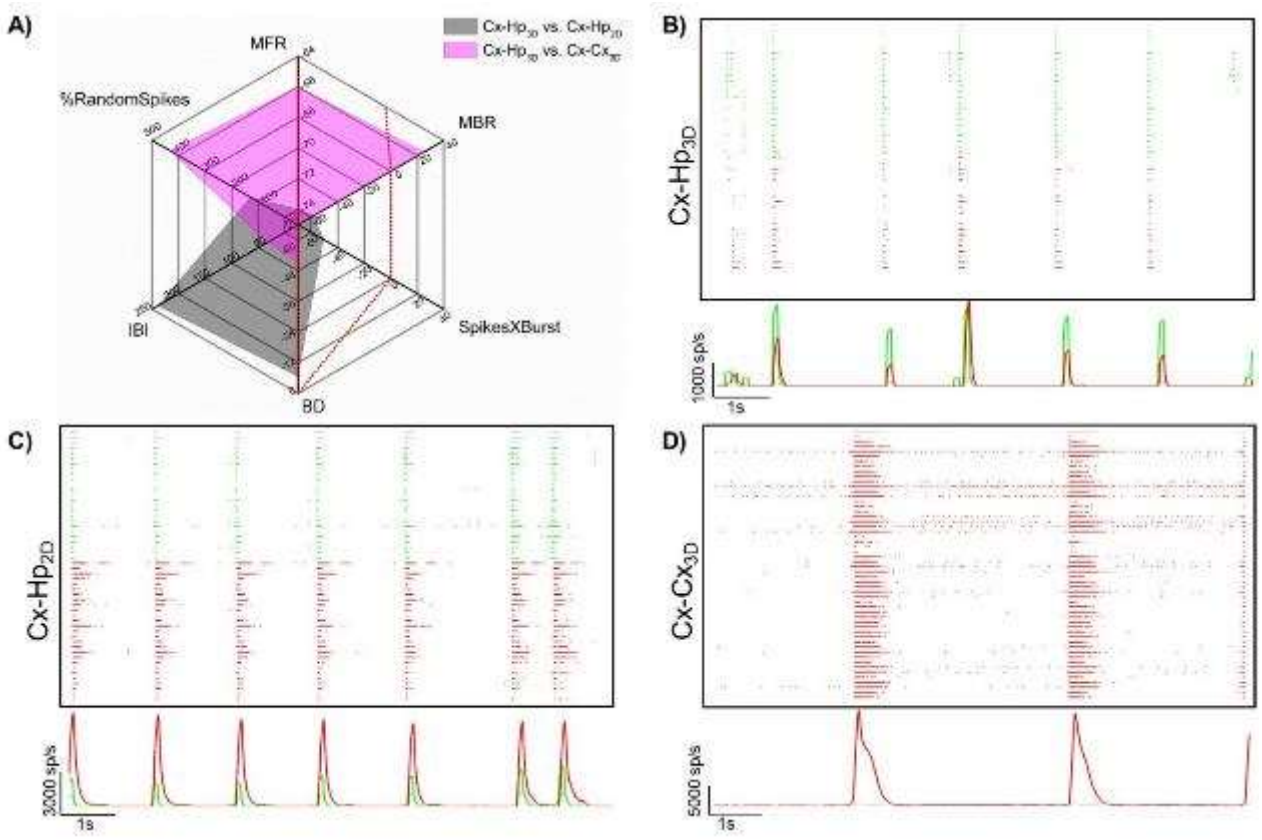

Figure 5.5: *Spontaneous electrophysiological activity of 3D heterogeneous cultures (Cx-Hp$_{3D}$) compared with 3D homogeneous cultures (Cx-Cx$_{3D}$) and 2D heterogeneous cultures (Cx-Hp$_{2D}$).* **(A)** *Radar plot showing the variations of the mean firing rate (MFR), mean bursting rate (MBR), burst duration (BD), inter burst interval (IBI), spikes per burst, and percentage random spikes induced by the different experimental configurations. Red line indicates no variations, gray shadow indicates the comparison heterogeneous 2D and 3D cultures, purple shadow indicates the comparison between 3D homogeneous and heterogeneous culture. Spontaneous activity and the relative trace of the instantaneous firing rate of a representative (10 s):* **(B)** *3D heterogeneous culture (Cx-Hp$_{3D}$, cortical-red and hippocampal-green).* **(C)** *2D heterogeneous culture (Cx-Hp$_{2D}$).* **(D)** *3D cortical culture (Cx-Cx$_{3D}$).*

The raster plots and the IFR traces (bin = 1ms) in Figures 5.5B and 5.5C show that in the 3D configuration the network activity is much faster than the one in 2D, with a much lower number of spikes per burst: the IFR shows peaks of about of 2'500 sp/s compared to 7'000 sp/s counted in the 2D configuration. Furthermore, Figure 5.5B also shows that the two neuronal populations

have very similar activities, while in Figure 5.5C it can be observed that the cortex displays longer bursts and higher IFR values than the hippocampus.
By comparing heterogeneous and homogeneous 3D populations, it is possible to see again that the cortical population changes its behavior. In the heterogeneous configuration, the cortex decreases the MFR but slightly increases its MBR (Figure 5.5A, purple). Furthermore, bursts are depleted of spikes in the presence of hippocampal population, inducing a strong increase in the percentage of random spikes. This trend leads to a decrease of the burst duration in the heterogeneous network. Finally, the significant increase of BD ($p = 0.04$) with the not-significant decrease of MBR ($p = 0.2$) leads to a significant increase of IBI ($p = 0.04$) in the 3D heterogeneous culture. The raster plots of the two configurations (Figure 5.5B and 5.5D) show very different activities: in the homogeneous one, the cortex presents a long-lasting network activity with about 15'000 sp/s during network events; in the heterogeneous one, short-lasting network events, yet more frequent, with an average of 1'500 sp/s, are detected.

5.3.5 Network Burst: the role of the hippocampal input

In this Section, I analyze the effects of the hippocampal input on the network bursting activity of the cortical region. In principle, hippocampal neurons favor a speed up of the cortical population activity independently from the spatial organization: the MNBR of the cortical activity strongly increases both in 2D (Figure 5.6A, + 251%, $p = 0.01$, black) and in 3D (Figure 5.6A, + 135%, $p = 0.03$, purple) network architectures. A modulation of the duration of these events has been observed: the NBD of the cortical ensembles decreases both in 2D (Figure 5.6B, -55%, $p = 0.01$, black) and in 3D (Figure 5.6B, -56% $p = 0.02$, purple). These results are supported by the dynamics of the hippocampal activity, which displays a shorter and faster bursting activity than the cortical one, (Figures 5.2A and 5.3A), thus suggesting how hippocampal neurons drive the collective activity of the heterogeneous system, in a sort of dominance-submissiveness configuration. Such an assumption is also supported by the analysis of the initiation sites of the network bursts. From each network burst, we identified the first spike and its relative position (i.e., electrode) in the MEA layout. Figures 5.6C, show four examples of the propagation of one randomly chosen network burst in a Cx-$Cx_{2D,}$ Cx-Hp_{2D}, Cx-Cx_{3D} and Cx-Hp_{3D} cultures. The largest black electrode identifies the initiation sites while the smallest black ones correspond to the no active sites (i.e., MFR < 0.1 sp/s). The color and size-coded electrodes display the propagation delays of the event. These propagation maps highlight that network bursts involve almost all the active electrodes of the MEA, regardless of the experimental configuration. In particular, the propagation of the network burst involves firstly the electrodes inside the compartment of the initiation site and then the second one. This result underlines the correct functional communication between two populations plated in the two chambers of the device supporting the structural evidences (Figures 5.1B and 5.1D): the propagation delay is related to the interaction mediated only by the channels and spans from a minimum of 40 ms to a maximum of 200 ms. In the heterogeneous 2D and 3D dataset, we found how network bursts have a mild

trend (statistically significant in the 3D configuration) to originate in the hippocampal assembly (Figure 5.6D, Cx-Hp$_{2D}$, p = 0.21, and Cx-Hp$_{3D}$, p = 0.04). In the case of the homogeneous 2D and 3D cortical networks no preferential regions were found (Figure 5.6D, Cx-Cx$_{2D}$, p = 0.91 and Cx-Cx$_{3D}$, p = 0.91), reinforcing the role of the hippocampal assembly as dominant sub-population.

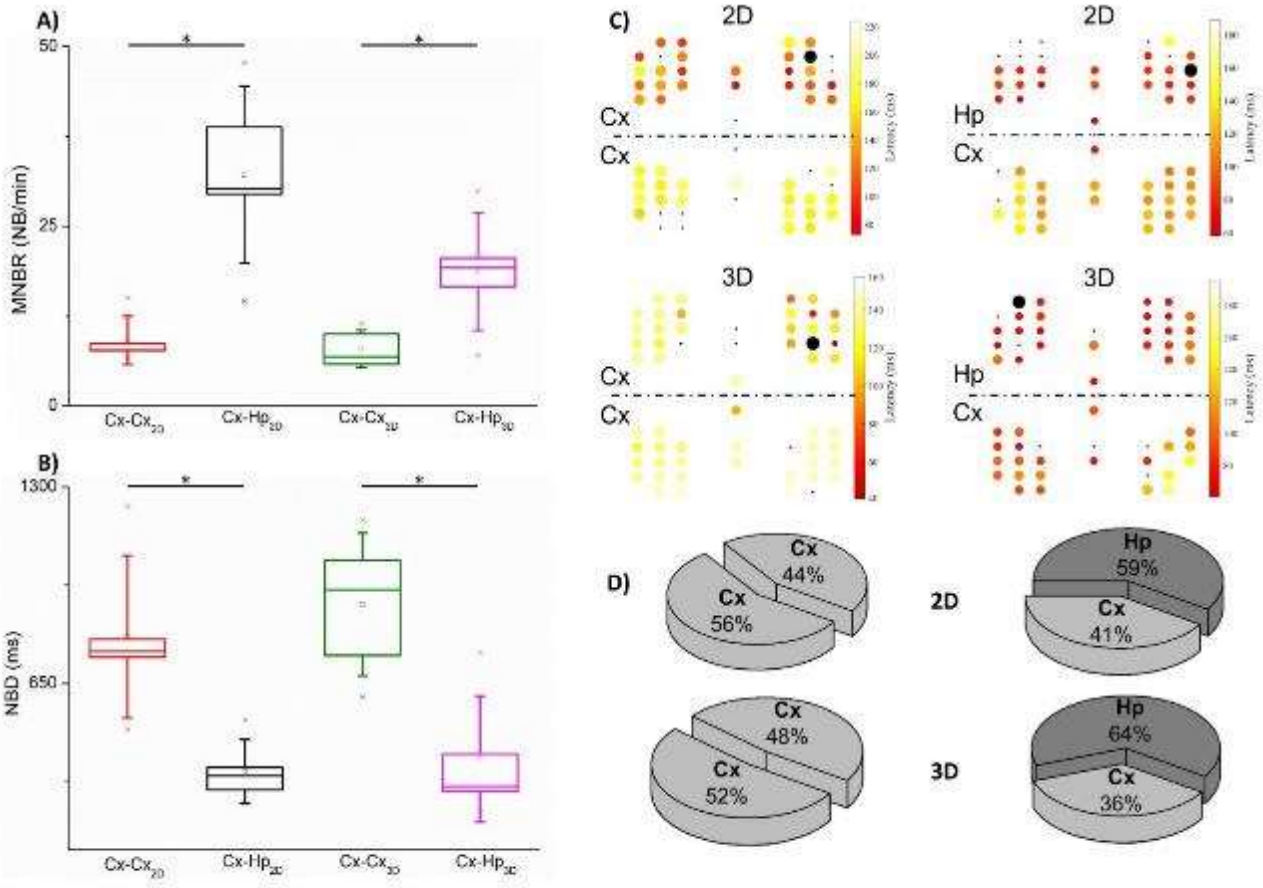

Figure 5.6: *Network bursting activity characterization of 2D homogeneous cortical (Cx-Cx$_{2D}$, red), 2D heterogeneous (Cx-Hp$_{2D}$ black), 3D homogeneous cortical (Cx-Cx$_{3D}$, green) and 3D heterogeneous (Cx-Hp$_{3D}$, purple) cultures.* **(A)** *Mean network bursting rate (MNBR, Cx-Cx$_{2D}$ vs. Cx-Hp$_{2D}$: p = 0.01; Cx-Cx$_{3D}$ vs. Cx-Hp$_{3D}$: p = 0.03).* **(B)** *Network burst duration (NBD, Cx-Cx$_{2D}$ vs. Cx-Hp$_{2D}$: p = 0.01; Cx-Cx$_{3D}$ vs. Cx-Hp$_{3D}$: p = 0.02).* **(C)** *Propagation maps of one network burst in the different experimental configuration. The big black dot represents the initiation site of the considered network burst. The color-coded shows the propagation delays of the event.* **(D)** *Percentage of the network burst origin evaluated over all the detected network.*

Once a network burst originates, all the active electrodes are involved (Figure 5.6C). Such recruitment is mediated by the choral activity of the excitation and inhibition pathways of the network, which modulates the rise (fast and glutamatergic-neurons mediated) and the decay (slower, and modulated by the GABAergic population) (Marom & Shahaf, 2002). Thus, we investigated the different phases (i.e., rise and decay) of the network burst trying to understand how the simultaneous 3D topology and hippocampal input modulate its shape. For this reason, we computed the STHs of the Cx-Hp$_{3D}$ configuration, and we compared them to Cx-Cx$_{3D}$ and Cx-Hp$_{2D}$ (Figure 5.7A).

At first glance, it is clear how the 3D homogeneous cortical population displays longer network bursts than the heterogeneous ones, both in 2D (black) and in 3D (purple) configurations. The inset of Figure 5.7A summarizes quantitatively this difference, by evaluating the differences of the three STH shapes in terms of the normalized distance described in Eq. (3). Keeping the Cx-

Hp_{3D} configuration as reference, I achieved a normalized distance D = 0.9 when compared to homogeneous 3D cortical networks, and D = 0.44 in the case of Cx-Hp_{2D}. From this analysis, it emerges how the introduction of the third dimension induces a weaker variation than the presence of another population type. The early phase of the network burst is characterized by the fast involvement of all the active electrodes and by a consequent increase of the firing rate fitted by the double exponential fit function $r(t)$ reported in Eq. (1). The first 40 ms of activation of three representative recordings of Cx-Hp_{3D} (purple), Cx-Hp_{2D} (black), Cx-Cx_{3D} (green) and their relative fits (solid lines) are reported in Figure 5.7B. The exponents span from 0.99 to 1.04 (average R^2 = 0.96) with no statistical differences (Cx-Hp_{3D} vs. Cx-Hp_{2D} p = 1, Cx-Hp_{3D} vs. Cx-Cx_{3D} p =0.67). From this analysis, it is possible to deduce that the neuron recruitment in such collective events is fast (τ < 1ms, no statistically significant differences, Figure 5.7B, *right*), independently from the network organization, but strongly regulated by the massive enrollment of the excitatory network (Eytan and Marom, 2006).

More variability is observed in the decay phase. Figure 5.7C *left* shows the STHs tails of the same three representative experiments and the correspondent exponential fitting (solid lines) derived from Eq. (2). The exponents span in a wider range of values than the activation phase (Figure 5.7C *left*, inset) as well as the correspondent time constants (Figure 5.7C, *right*), ranging from 51.91 ± 26 ms (Cx-Hp_{3D}) to 219.1 ± 71 ms (Cx-Cx_{3D}). The faster decay behavior in the heterogeneous cultures can be explained by the inhibitory nature of the connections from the hippocampal assembly to the cortical one, which can short the duration of the network burst, or the delay time of the propagation (larger negative exponents). Nonetheless, this trend is slightly observed when we moved from a 2D to a 3D configuration suggesting a larger amount of inhibitory links among the layers of the hippocampus network (Eytan and Marom, 2006). It is worth to notice that between the two compartments there are only 25 channels, this could justify the lack of statistical relevance between Cx-Hp_{3D} and Cx-Hp_{2D} (mean τ, Cx-Hp_{3D} = 51.4 ms vs. Cx-Cx_{3D} = 96.2 ms , p = 0.05).

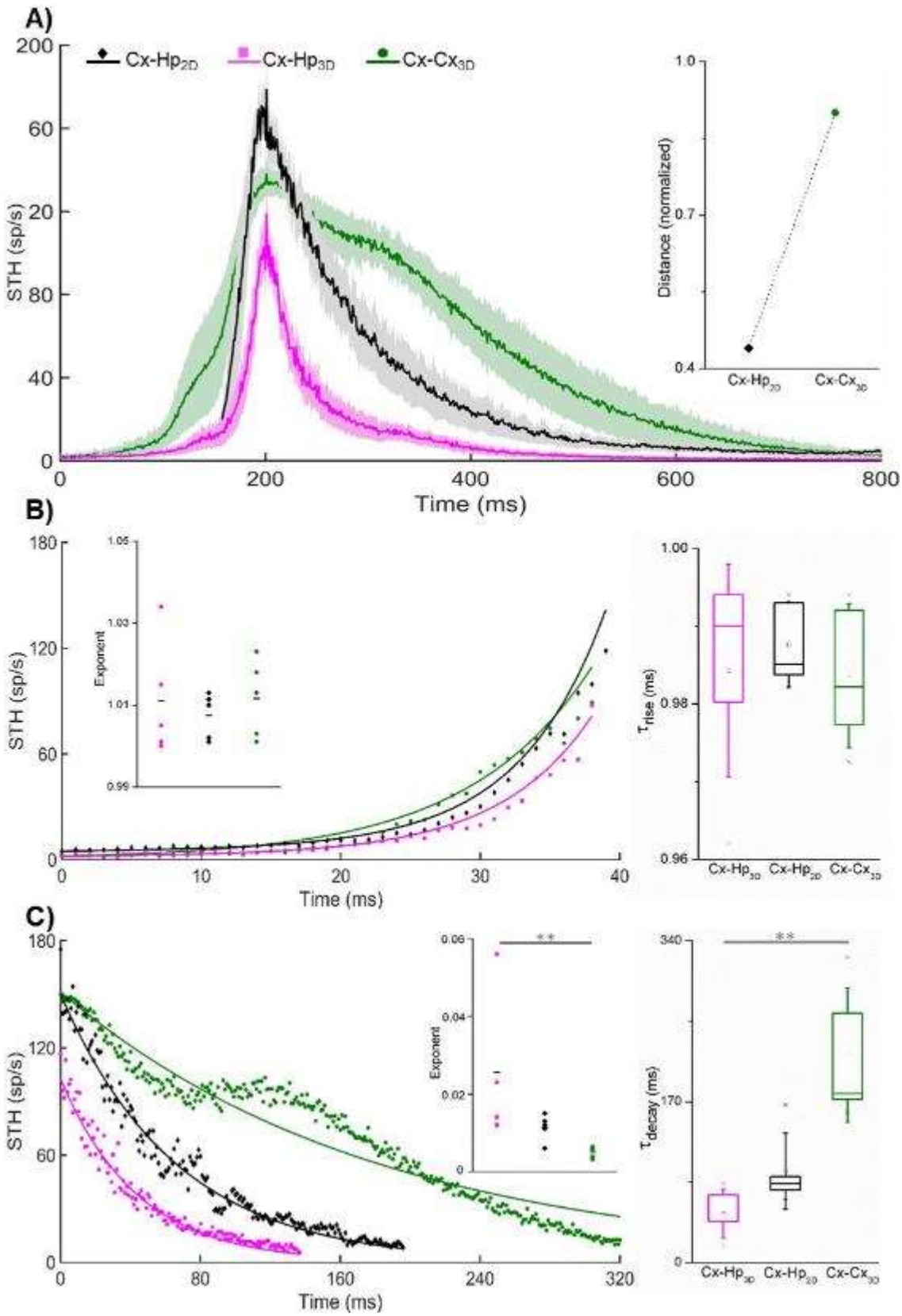

Figure 5.7: *Network bursting activity dynamics of 3D heterogeneous (Cx-Hp3D , purple—square) compared with 2D heterogeneous (Cx-Hp2D black—diamond) and 3D homogeneous cortical (Cx-Cx3D , green—dots) cultures.* **(A)** *Average Spike Times Histogram (STH). Inset: NBs normalized distances between Cx-Hp3D (reference) and Cx-Hp2D (black diamond) and Cx-Cx3D (green dot).* **(B)** *STH rise phase of three representative experiments (one per each configuration) and relative fitting (solid line), left. The inset shows the exponents of the best-fit rising phase (five values per each dataset). Right, time constants of the rise phase (Cx-Hp3D vs. Cx-Cx3D , p = 0.67, Cx-Hp3D vs. Cx-Hp2D , p = 1).* **(C)** *STH decay phase of three representative experiments (one per each configuration) and relative fitting (solid line), left. The inset shows the exponent of the best-fit decaying phase (five values per each dataset). Right, time constant of decay dynamics (Cx-Hp3D vs. Cx-Cx3D , p = 0.008, Cx-Hp3D vs. Cx-Hp2D , p = 0.05).*

5.4 Conclusions

In this work, I demonstrated the feasibility of an *in vitro* experimental model where the three main topological features of the actual brain structures (i.e., modularity, heterogeneity, and three-dimensionality) are preserved. Three-dimensional networks were developed by using glass microbeads as a biocompatible scaffold. Such networks are composed of two separate cortical and hippocampal populations that are physically connected by thin polymeric microchannels that allow the passage of neurites bundles only. Such a structure has been successfully coupled to substrate embedded micro-electrodes, capable to extracellularly record the emerging patterns of electrophysiological activity.

These experimental choices were driven by a previous works: in 2012, a dual-compartment PDMS-based mask was developed; it allowed to demonstrate the possibility to cultivate, over the active area of 60-channels MEAs, a bi-dimensional cortical-thalamic network (Kanagasabapathi et al., 2012). In 2014, the experimental protocol devised in (Pautot et al., 2008) was optimized and tailored to investigate the functional properties of 3D hippocampal networks, using 40 μm diameter glass microbeads as a scaffold to be integrated with planar MEAs (Tedesco et al., 2015). Since they had already observed that the electrophysiological activity obtained by 3D cultures grown over glass microbeads (Frega et al., 2014) is equivalent to that obtained using chitosan-based scaffolds (Tedesco et al., 2018), in this work, I used a more "controllable" material, i.e. glass microbeads, to facilitate the segregation of the different populations.

By exploiting a fully controllable *in vitro* system based on the MEA set-up, I first untangled how the single components (synaptic input and network organization) shapes the cortical dynamics. Finally, an actual realistic structure of interconnected brain regions on-a-chip was created, where two different neuronal populations are cultivated over the active area of MEAs in a 3D fashion and connected by means of bundles of neurites. In particular, I investigated the emerging spontaneous electrophysiological activity of 3D cortical-hippocampal cultures (Cx-Hp_{3D}) by comparing the results with the dynamics originated by homogeneous 3D (i.e., Cx-Cx_{3D}) and heterogeneous 2D (Cx-Hp_{2D}) control cultures. The results demonstrate how the stereotyped and rhythmic patterns of electrophysiological activity found in conventional planar *in vitro* cortical ensembles (Marom and Eytan, 2005; Rolston et al., 2007; Van Pelt et al., 2004; Wagenaar, et al., 2006) can be altered either i) by the introduction of a larger amount of synaptic inputs (i.e., 3D structure) or ii) by triggering the network with external biological stimuli having a different intrinsic firing pattern (i.e., coupled heterogeneous networks such as cortical and hippocampal ones, as highlighted in Figures 5.2 and 5.3). Considering the enhanced dendritic arborization in the 3D architecture, one can speculate that the resulting network presents longer spatial interactions among the neurons, which contribute to modulate the shape of the bursts and temporally differentiate the network activity (Figure 5.4E). While the 3D configuration acts on the bursting dynamics, the heterogeneity induces a global increase in the activity rate. From the analysis of the STH fitting curves (Figure 5.7), one can assume that the simultaneous presence of 3D structure and hippocampal neurons modulate only the decay of the population events. The

neuronal recruitment is fast and completely independent from the network composition and the resulting architecture is essentially mediated by the choral activation of the excitatory population (Eytan and Marom, 2006; Van De Vijver et al., 2019). The strong differences emerge during the decay phase, which is mediated by the activation of the inhibitory circuits (Eytan and Marom, 2006): when mere cortical neurons are arranged in a 3D structure, a long and slow tail (τ = 219.1 ± 71 ms) can be appreciated (Figure 5.7A, green line), suggesting a weak contribution of the inhibitory neurons. This hypothesis is supported by the experimental results found by (Eytan and Marom, 2006), who obtained longer network bursts with the introduction of bicuculline to block the fast inhibitory contribution. Based on this evidence, one can speculate how the hippocampal neurons provide a strong inhibitory contribution to the cortical ensemble or induce greater local inhibitory development, by significantly reducing the duration of the network burst (Figure 5.6B, $Cx\text{-}Cx_{2D}$ = 804.58 ± 268 ms, $Cx\text{-}Hp_{2D}$ = 359.56 ± 105 ms, $Cx\text{-}Cx_{3D}$ = 911.2 ± 236 ms, $Cx\text{-}Hp_{3D}$ = 400.4 ± 208 ms) as well as its decay dynamics (τ = 51.91 ± 26 ms). Such a behavior, although not statistically significant, appears more pronounced in the 3D configuration than in the 2D one. Eventually, significant differences with respect to homogeneous 2D cortical networks were observed, both in terms of spiking and bursting activity: the simultaneous presence of a 3D organization and the synaptic input from another brain region, allowed a wider dynamics repertory, similarly to what can be found in the *in vivo* counterpart (Klausberger T. et al., 2003; Leinekugel et al., 2002).

It is important to consider that the obtained results are related to the choices that I made in the development of the experimental framework. This model strongly promotes the intra-compartment connectivity in all the possible directions since no constraints were added. This condition leads to extremely dense networks within the same compartment (Figure 5.1C), where cells may extend their processes to establish synaptic connections within the same or among different layers (Figure 5.1E). Regarding the inter-compartment links, the PDMS array of 25 microchannels strongly limits the connectivity between the two populations (Figure 5.1D); on the other hand, its relatively short length of 150 µm allows a communication mediated by both axons and dendrites (Taylor et al., 2005). Nonetheless, the choice to limit the inter-compartment connectivity has its own natural counterpart in the actual *in vivo* systems, where the modular organization of the neuronal assemblies, recognized as the best candidate to describe the topological organization of the brain, is sustained by such an unbalanced distribution of connectivity (Bertolero et al., 2015; Sporns and Betzel, 2016).

There are two principal limitations of the experimental paradigm presented: the first one is the existence of only one array of inter-compartment connections located in the plane of the substrate-integrated electrodes. The current configuration forces the connections between the 3D populations to be planar, since non-pathways exist at different depth of the structure. The second limitation is the impossibility to record the electrophysiological activity of the network at different heights of the structure. Nowadays, there are few technological options to measure the electrophysiological activity from many locations simultaneously throughout a 3D *in vitro*

neuronal network. In the current experimental configuration, the electrophysiological activity can be recorded only from the layer of neurons directly coupled to the active area of the MEA: the effect of the upper layers are “read” by quantifying the differences in the patterns of electrophysiological activity from a subset of “read-out” neurons. This evidence restricts the characterization of the emerging dynamics in terms of spatial and propagation analysis: inferring the topological properties of the functional connectivity of such a 3D network cannot be performed due to the absence of recording sites which can make possible to map the effective functional propagation of the signals among layers. Possible solutions to overcome such a problem have been presented only very recently: (Soscia et al., 2020) developed a thin-film, 3D flexible 256-channels MEA that extracellularly probes 3D cultures of human iPSC-derived neurons and astrocytes entrapped in a collagen hydrogel scaffold.

With this study, I demonstrated the possibility to develop a valid *in vitro* experimental model where different neuronal populations are interconnected in a 3D fashion to define a prototype of *brain-on-a-chip*. Albeit this model is far from fully reproducing the brain *in vivo* conditions, this is an important step toward the increase of the represented complexity, with respect to the current *in vitro* conditions. In perspective, the so developed experimental model could help to understand how brain cells connect and interact and how neurological disorders impair this connection or destroy small/medium neuronal assemblies. The chance to have an *in vitro* test-bed where a different number of neuronal populations are functionally connected would allow to predict how cells are responsive to pharmaceutical drugs and to determine if certain kinds of neuronal families are more reactive to such drugs delivery. As an example, this experimental protocol could be found a valid application to cultivate cortical and thalamic 3D networks whose connectivity impairment is involved in many pathological conditions such as Parkinson’s (Dorsey et al., 2007), epilepsy (Bertram, 2013) and schizophrenia (Lewis and Sweet, 2009). Although *in vivo* electrophysiological recordings allow, in principle, to study such pathways, low spatial resolution of the recording electrodes and the influence of other regions of the brain not strictly involved in the pathology are often a hindrance in understanding the sole interaction between two or more brain regions.

References

Bardy, C., Van Den Hurk, M., Eames, T., Marchand, C., Hernandez, R. V., Kellogg, M., Gorris, M., Galet, B., Palomares, V., Brown, J., Bang, A. G., Mertens, J., Böhnke, L., Boyer, L., Simon, S., & Gage, F. H. (2015). Neuronal medium that supports basic synaptic functions and activity of human neurons in vitro. *Proceedings of the National Academy of Sciences of the United States of America*, *112*(20), E2725–E2734. https://doi.org/10.1073/pnas.1504393112

Bertolero, M. A., Thomas Yeo, B. T., & D'Esposito, M. (2015). The modular and integrative functional architecture of the human brain. *Proceedings of the National Academy of Sciences of the United States of America*, *112*(49), E6798–E6807. https://doi.org/10.1073/pnas.1510619112

Bertram, E. H. (2013). Neuronal circuits in epilepsy: Do they matter? In *Experimental Neurology* (Vol. 244, pp. 67–74). NIH Public Access. https://doi.org/10.1016/j.expneurol.2012.01.028

Chiappalone, M., Novellino, A., Vajda, I., Vato, A., Martinoia, S., & van Pelt, J. (2005). Burst detection algorithms for the analysis of spatio-temporal patterns in cortical networks of neurons. *Neurocomputing*, *65–66*(SPEC. ISS.), 653–662. https://doi.org/10.1016/j.neucom.2004.10.094

Dauth, S., Maoz, B. M., Sheehy, S. P., Hemphill, M. A., Murty, T., Macedonia, M. K., Greer, A. M., Budnik, B., & Parker, K. K. (2017). Neurons derived from different brain regions are inherently different in vitro: A novel multiregional brain-on-a-chip. *Journal of Neurophysiology*, *117*(3), 1320–1341. https://doi.org/10.1152/jn.00575.2016

Dorsey, E. R., Constantinescu, R., Thompson, J. P., Biglan, K. M., Holloway, R. G., Kieburtz, K., Marshall, F. J., Ravina, B. M., Schifitto, G., Siderowf, A., & Tanner, C. M. (2007). Projected number of people with Parkinson disease in the most populous nations, 2005 through 2030. *Neurology*, *68*(5), 384–386. https://doi.org/10.1212/01.wnl.0000247740.47667.03

Eytan, D., & Marom, S. (2006). Dynamics and effective topology underlying synchronization in networks of cortical neurons. *Journal of Neuroscience*, *26*(33), 8465–8476. https://doi.org/10.1523/JNEUROSCI.1627-06.2006

Frega, M., Tedesco, M., Massobrio, P., Pesce, M., & Martinoia, S. (2014). Network dynamics of 3D engineered neuronal cultures: A new experimental model for in-vitro electrophysiology. *Scientific Reports*, *4*(May). https://doi.org/10.1038/srep05489

Kanagasabapathi, T. T., Massobrio, P., Barone, R. A., Tedesco, M., Martinoia, S., Wadman, W. J., & Decré, M. M. J. (2012). Functional connectivity and dynamics of cortical-thalamic networks co-cultured in a dual compartment device. *Journal of Neural Engineering*, *9*(3). https://doi.org/10.1088/1741-2560/9/3/036010

Klausberger T., Magill PJ, Marton LF, Roberts JDB, Cobden PM, Buzsáki G, & P., S. (2003). Brain-state- and cell-type-specific firing of hippocampal interneurons in vivo. *Nature*, *421*(6925), 844–848.

Leinekugel, X., Khazipov, R., Cannon, R., Hirase, H., Ben-Ari, Y., & Buzsáki, G. (2002). Correlated bursts of activity in the neonatal hippocampus in vivo. *Science*, *296*(5575), 2049–2052. https://doi.org/10.1126/science.1071111

Lewis, D. A., & Sweet, R. A. (2009). Schizophrenia from a neural circuitry perspective: Advancing toward rational pharmacological therapies. In *Journal of Clinical Investigation* (Vol. 119, Issue 4, pp. 706–716). American Society for Clinical Investigation. https://doi.org/10.1172/JCI37335

Maccione, A., Gandolfo, M., Massobrio, P., Novellino, A., Martinoia, S., & Chiappalone, M. (2009). A novel algorithm for precise identification of spikes in extracellularly recorded neuronal signals. *Journal of Neuroscience Methods*, *177*(1), 241–249. https://doi.org/10.1016/j.jneumeth.2008.09.026

Mao, S., Xiong, G., Zhang, L., Dong, H., Liu, B., Cohen, N. A., & Cohen, A. S. (2016). Verification of the cross immunoreactivity of A60, a mouse monoclonal antibody against neuronal nuclear protein. *Frontiers in Neuroanatomy*, *10*(MAY). https://doi.org/10.3389/fnana.2016.00054

Marom, S., & Eytan, D. (2005). Learning in ex-vivo developing networks of cortical neurons. In *Progress in Brain Research* (Vol. 147, Issue SPEC. ISS., pp. 189–199). Elsevier B.V. https://doi.org/10.1016/S0079-6123(04)47014-9

Marom, S., & Shahaf, G. (2002). Development, learning and memory in large random networks of cortical neurons: Lessons beyond anatomy. In *Quarterly Reviews of Biophysics* (Vol. 35, Issue 1, pp. 63–87). Cambridge University Press. https://doi.org/10.1017/S0033583501003742

Pasquale, V., Martinoia, S., & Chiappalone, M. (2010). A self-adapting approach for the detection of bursts and network bursts in neuronal cultures. *Journal of Computational Neuroscience*, *29*(1–2), 213–229. https://doi.org/10.1007/s10827-009-0175-1

Pautot, S., Wyart, C., & Isacoff, E. Y. (2008). Colloid-guided assembly of oriented 3D neuronal networks. *Nature Methods*, *5*(8), 735–740. https://doi.org/10.1038/nmeth.1236

Rolston, J. D., Wagenaar, D. A., & Potter, S. M. (2007). Precisely timed spatiotemporal patterns of neural activity in dissociated cortical cultures. *Neuroscience*, *148*(1), 294–303. https://doi.org/10.1016/j.neuroscience.2007.05.025

Schindelin, J., Arganda-Carreras, I., Frise, E., Kaynig, V., Longair, M., Pietzsch, T., Preibisch, S., Rueden, C., Saalfeld, S., Schmid, B., Tinevez, J. Y., White, D. J., Hartenstein, V., Eliceiri, K., Tomancak, P., & Cardona, A. (2012). Fiji: An open-source platform for biological-image analysis. In *Nature Methods* (Vol. 9, Issue 7, pp. 676–682). Nature Publishing Group. https://doi.org/10.1038/nmeth.2019

Schüz, A., & Palm, G. (1989). Density of neurons and synapses in the cerebral cortex of the mouse. *The Journal of Comparative Neurology*, *286(4)*, 442–445. https://doi.org/10.1002/cne.902860404.

Soscia, D. A., Lam, D., Tooker, A. C., Enright, H. A., Triplett, M., Karande, P., Peters, S. K. G., Sales, A. P., Wheeler, E. K., & Fischer, N. O. (2020). A flexible 3-dimensional microelectrode array for: In vitro brain models. *Lab on a Chip*, *20*(5), 901–911. https://doi.org/10.1039/c9lc01148j

Soscia, D., Belle, A., Fischer, N., Enright, H., Sales, A., Osburn, J., Benett, W., Mukerjee, E., Kulp, K., Pannu, S., & Wheeler, E. (2017). Controlled placement of multiple CNS cell populations to create complex neuronal cultures. *PLOS ONE*, *12*(11), e0188146. https://doi.org/10.1371/journal.pone.0188146

Sporns, O., & Betzel, R. F. (2016). Modular Brain Networks. *Annual Review of Psychology*, *67*(1), 613–640. https://doi.org/10.1146/annurev-psych-122414-033634

Stegenga, J., Le Feber, J., & Rutten, W. L. C. (2008). *Changes within bursts during learning in dissociated neural networks*.

Taylor, A. M., Blurton-Jones, M., Rhee, S. W., Cribbs, D. H., Cotman, C. W., & Jeon, N. L. (2005). A microfluidic culture platform for CNS axonal injury, regeneration and transport. *Nature Methods*, *2*(8), 599–605. https://doi.org/10.1038/nmeth777

Tedesco, M., Frega, M., Martinoia, S., Pesce, M., & Massobrio, P. (2015). Interfacing 3D engineered neuronal cultures to micro-electrode arrays: An innovative in vitro experimental model. *Journal of Visualized Experiments*, *2015*(104). https://doi.org/10.3791/53080

Tedesco, M. T., Di Lisa, D., Massobrio, P., Colistra, N., Pesce, M., Catelani, T., Dellacasa, E., Raiteri, R., Martinoia, S., & Pastorino, L. (2018). Soft chitosan microbeads scaffold for 3D functional neuronal networks. *Biomaterials*, *156*, 159–171. https://doi.org/10.1016/j.biomaterials.2017.11.043

Van De Vijver, S., Missault, S., Van Soom, J., Van Der Veken, P., Augustyns, K., Joossens, J., Dedeurwaerdere, S., & Giugliano, M. (2019). The effect of pharmacological inhibition of serine proteases on neuronal networks in vitro. *PeerJ*, *2019*(4), 1–23. https://doi.org/10.7717/peerj.6796

Van Pelt, J., Wolters, P. S., Corner, M. A., Rutten, W. L. C., & Ramakers, G. J. A. (2004). Long-Term Characterization of Firing Dynamics of Spontaneous Bursts in Cultured Neural Networks. *IEEE TRANSACTIONS ON BIOMEDICAL ENGINEERING*, *51*(11). https://doi.org/10.1109/TBME.2004.827936

Wagenaar, D. A., Pine, J., & Potter, S. M. (2006). An extremely rich repertoire of bursting patterns during the development of cortical cultures. *BMC Neuroscience*, *7*, 1–18. https://doi.org/10.1186/1471-2202-7-11

Wang, B., Zhao, Y., Lin, H., Chen, B., Zhang, J., Zhang, J., Wang, X., Zhao, W., & Dai, J. (2006). Phenotypical analysis of adult rat olfactory ensheathing cells on 3-D collagen scaffolds. *Neuroscience Letters*, *401*(1–2), 65–70. https://doi.org/10.1016/j.neulet.2006.02.085

Conclusions

The aim of my project was to investigate a non-invasive ultrasound (US) based neuromodulation technique, which would represent an alternative to classical electrical stimulation to interact with the brain. Even though US are collecting an increasing interest in the scientific community for their several advantages (high spatial resolution, low cost, and non-invasiveness), the mechanisms through which sound waves interact with cells are still unclear. Under this perspective, I considered a few possible strategies to induce a specific electrophysiological response of neuronal assemblies *in vitro* to US pulses. First of all, I applied US on neuronal cells treated with piezoelectric barium titanate nanoparticles (BTNPs) (Cf., Chapter 2), in order to exploit their piezoelectric effect to transduce the mechanical stimulus into an electrical one. As an alternative approach, I also applied US on immortalized human embryonic kidney cells (HEK-293) which had been genetically modified to overexpress mechanosensitive (namely, Piezo1) channels (Cf., Chapter 3). Moreover, I used US stimulation to establish an experimental protocol to release a model drug, Doxorubicin, stored in polyelectrolyte microcapsules, fabricated with the layer-by-layer technique (C.f., Chapter 4). In the end, to make all the experimental models closer to the *in vivo* scenario, I also designed a more realistic experimental set-up to investigate the above strategy on heterogeneous (i.e., neurons coming from different brain areas) and three-dimensional (3D) neuronal networks (C.f., Chapter 5). As it is known, cells in the body (i.e., brain) are characterized by a 3D-structure and multi-cellular links, so 3D structures are more powerful model than 2D ones in order to emulate the *in vivo* effects. It is important to emphasize that the three aforementioned projects are strongly interrelated. Achieving an *in vitro* model closer to the *in vivo* situation helped me either to research and characterize neuromodulation techniques (US stimulation) or to set up a US-mediated drug screening method.

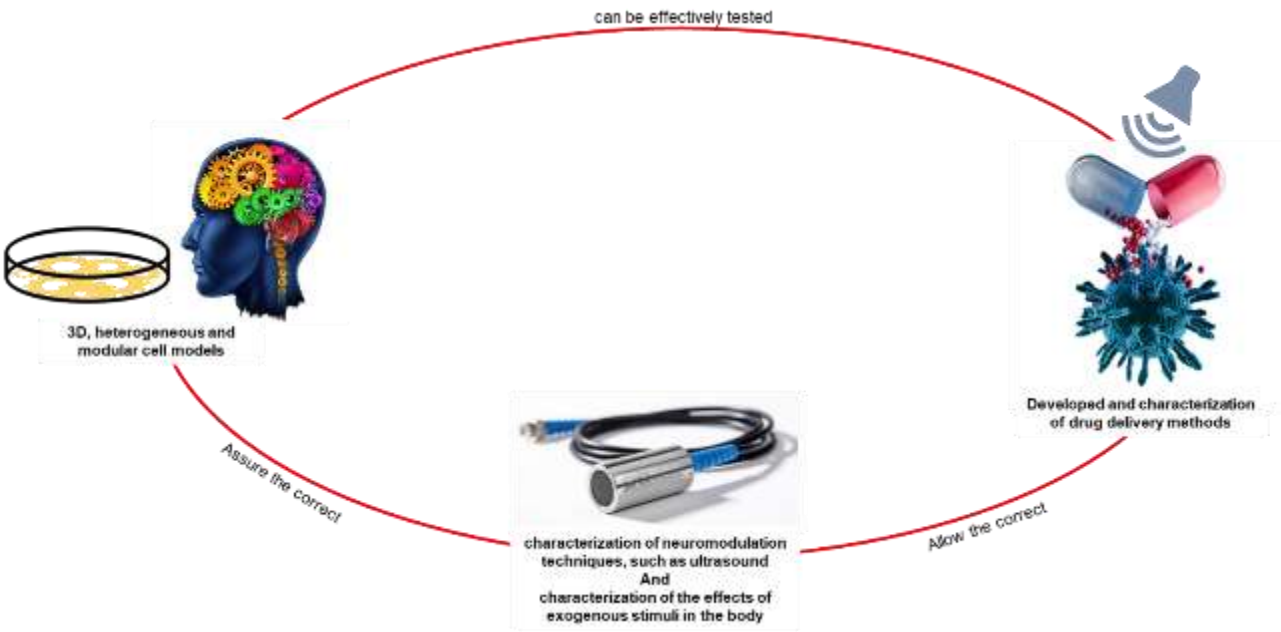

The effect induced by the US on HEK293 cells leads to consider this technique as an excellent candidate for neuromodulation. Thus, the next step will be to switch to primary cultures of neurons that will be transfected using viral vectors to overexpress Piezo type channels, to induce, in a selective way, an electrical response. With the development of 3D models that take into account different cell populations, one might test the effects of US stimulation on these models, resulting in effects that should be closer to in vivo ones. Furthermore, using scaffolds with various morphological properties to define 3D models, it could be possible to reach a more accurate investigation of the different cellular sensitivity related to the different plating substrates, as observed in the calcium imaging studies.

In the case of the US-controlled drug release model (Cf. Chapter 4), the same protocol could be used for different types of drug nanocarriers, and also in this case, characterization in an in vitro model that is not purely 2D but mimics the in vivo environment should be done before going on to in vivo experiments.

Appendix A

Analysis

Electrophysiological Analysis

All the algorithms were developed in Matlab (The Mathworks, Natik, US).

Spike and Burst Detection

Raw data were spike-detected using the Precise Timing Spike Detection (PTSD) algorithm (Maccione et al., 2009). The algorithm required the setting of three parameters: (I) a differential threshold value which was set independently for each channel and calculated as 8 times the standard deviation of the signal's biological and thermal noise; (II) a peak lifetime period related to the duration of a spike (set at 2 ms); (III) a refractory period associated to the minimum interval between two consecutive events (set at 1 ms). Raw data were not spike sorted, since spike sorting did not significantly increase the spatial reconstruction of the network, when we sampled the activity of a few thousand neurons with only 60 microelectrodes. Once spike trains had been created, the bursts identification was performed by means of the string method devised in (Chiappalone et al., 2005). Two parameters were set: (I) the minimum number of spikes needed to be recognized as a burst (set at 5); (II) the maximum inter-spike interval that divides adjacent spikes into a burst (set at 100 ms). After spike and burst trains had been created, the following quantitative measurements were extracted to characterize the electrophysiological activity: mean firing (MFR) and bursting rate (MBR), i.e., the mean number of spikes/bursts per second/minute averaged over the active channels; burst duration (BD), i.e., the temporal length of the burst; inter burst interval (IBI), i.e., temporal distance between two consecutive burst events; percentage of random spikes, i.e., the ratio between the spikes inside and outside the burst; spikes per burst, i.e. the number of spikes in each burst. A channel was considered active if it recorded at least one spike in 10 seconds (MFR > 0.1 sp/s) and four bursts in a minute (MBR > 4 bursts/min).

Network burst detection and Analysis

The identification of the network bursts was performed according to the self-adapting algorithm described in (Pasquale et al.,2010). A network burst was identified as a sequence of events having an IBI smaller than a reference value (set at 100 ms) and involving at least 20% active electrodes. From the network burst train, I extracted the mean network bursting

rate (MNBR), i.e., the mean number of network bursts per minute, and the network burst duration (NDB), i.e., the temporal extension these events. The dynamics of the network bursts allowed deriving recruitment mechanisms of the neurons of the network and speculating about the functional connectivity properties (Eytan & Marom, 2006).

To get more information about the dynamics originating the network bursts, and how the different network configurations modulate their shape, the average Spike Time Histogram (STH) was calculated from the profile of the instantaneous firing rate (IFR). Briefly, all IFRs relative to each network burst were temporally aligned. Considering as reference a randomly chosen IFR trace, the delay that produces the maximum absolute value of cross-correlation between it and the remaining network bursts was evaluated. Such a delay was used to align each IFR by temporally shifting the data. In order to ensure proper alignment, the method accuracy was tested in terms of the correlation coefficient: the average STH was accepted when the correlation coefficient was higher than 0.4. The temporal evolution of the STH was analyzed focusing on the slope of the rising and decaying phases. The rising phase of the STH has been fitted by a double exponential function $r(t)$:

$$r(t) = a_0 e^{(b_0-1)t} + a_1 e^{(b_1-1)t} + d \quad (1)$$

where the smaller of the two exponents b_0 or b_1 define the neuron recruitment rate (Van De Vijver et al., 2019). In Eq. (1), a_0, a_1, and d are the coefficients of the fitting equation. Instead, to fit the decay phase, a simple first-degree exponential function $d(t)$ was used (Marom & Shahaf, 2002):

$$d(t) = c_0 e^{\gamma t} + c_1 \quad (2)$$

where the value of the exponent γ describes the network modulation during the network burst events, and c_o and c_1 are the fitting coefficients.

To quantify the effects of the network structure and the role of the hippocampal input, the shape changes of STH were evaluated by means of the normalized distance (Dj) between the j-th STH profile and the reference STH_{ref} (Stegenga et al., 2008):

$$D_j = \frac{RMS(STH_j - STH_{ref})}{RMS(STH_{ref})} \quad (3)$$

In Eq. (3) RMS indicates the root-mean square error

Ultrasound and Electrical stimulation algorithms

When the neuronal cultures were subjected to US stimulation, the digital signal, that indicates the on and off phases of the stimulation, was recorded. After the spike train detection, a Matlab script uses the registered digital signal, which was only a zero (ultrasound off) and a one (ultrasound on) signal, to synchronize the electrode signals with the generation of US, removing any possible glitches in the raw data caused by the US transducer switching on (US_{on}) and off (US_{off}). Such a procedure was implemented with the following steps: i) identification of the time stamps at which the US turned on or off on the raw data, using the digital signal; ii) artifact removal, deleting an average of 10 samples (1 ms) just after the transition. Once the artifacts were removed from the spike train, bursting activities was identified as described above.

With the US stimulation, the percentage of active channels (%Ch) for each cell culture was determined during the three phases of the experimental protocol: pre-stimulus, stimulus and post-stimulus. Considering that each MEA may have a different number of active channels already in the basal phase, these values were normalized to the pre-stimulation period to ensure a comparison between the different experiments.

During the stimulation phase, I calculated the probability that the channels were active ($P(Ch_{active})$) taking into account separately the US_{on} and US_{off} periods. Using the acquired digital signal, the two-time phases of the ultrasound were identified on the peak trains and for each on (or off) phase the channels with a least one occurrence were counted. Finally, this value was averaged over the number of active channels. Moreover, the ($P(Ch_{active})$) was studied by splitting the 45 pulses into groups of three to determine the network weakness level during the three minutes of stimulation. The cumulative ($P(Ch_{active})$) of all cultures stimulated with the same amplitude was determined for each stimulation group, and compared for each on and off phases.

Finally, the Post Stimulus Time Histogram (PSTH) of the channel activation was determined to compare US stimulation with the electrical one. Using the digital signal (present for both stimulations), the probability was evaluated in a time window of 500 ms following the stimulation with bin of 5ms. Since obtaining the PSTH of each stimulation, the areas underlying the PSTH curves were calculated.

Calcium Imaging Analysis

ImageJ was used to examine the stacks produced during the microscope acquisition. It was possible to select individual cells using the *Roi Manager* to obtain the pattern of their fluorescence intensity as a function of time. In order to detect a true activation of the Piezo1 channels due to the US rather than a calcium transient effect due to cellular proximity to activation sites, non-adjacent cells were chosen for cell selection. The intensity curves were then obtained with Matlab and analyzed with Ana Software, an open source software created by Michael Pusch. It's worth noting that the details about US activation has been registered and stored in a separate file for each stack of images (*USreport*). It was possible to suit the curves with four-component (third-degree) polynomials using Ana Software. The occurrence of an inflection in the curve in the stimulation region (obtained through the *USreport* file) was discovered after the fitting was completed. An infection on the curve indicated the end of the photobleaching trend, which is a descendent trend. The second derivative was measured using the open source program SigmaPlot to detect the inflection. Finally, a Matlab script was created to enable the US stimulation period to be superimposed on the temporal intensity trend.

References

Chiappalone, M., Novellino, A., Vajda, I., Vato, A., Martinoia, S., & van Pelt, J. (2005). Burst detection algorithms for the analysis of spatio-temporal patterns in cortical networks of neurons. *Neurocomputing*, *65–66*(SPEC. ISS.), 653–662. https://doi.org/10.1016/j.neucom.2004.10.094

Eytan, D., & Marom, S. (2006). Dynamics and effective topology underlying synchronization in networks of cortical neurons. *Journal of Neuroscience*, *26*(33), 8465–8476. https://doi.org/10.1523/JNEUROSCI.1627-06.2006

Maccione, A., Gandolfo, M., Massobrio, P., Novellino, A., Martinoia, S., & Chiappalone, M. (2009). A novel algorithm for precise identification of spikes in extracellularly recorded neuronal signals. *Journal of Neuroscience Methods*, *177*(1), 241–249. https://doi.org/10.1016/j.jneumeth.2008.09.026

Marom, S., & Shahaf, G. (2002). Development, learning and memory in large random networks of cortical neurons: Lessons beyond anatomy. In *Quarterly Reviews of Biophysics* (Vol. 35, Issue 1, pp. 63–87). Cambridge University Press. https://doi.org/10.1017/S0033583501003742

Pasquale, V., Martinoia, S., & Chiappalone, M. (2010). A self-adapting approach for the detection of bursts and network bursts in neuronal cultures. *Journal of Computational Neuroscience*, *29*(1–2), 213–229. https://doi.org/10.1007/s10827-009-0175-1

Stegenga, J., Le Feber, J., & Rutten, W. L. C. (2008). *Changes within bursts during learning in dissociated neural networks*.

Van De Vijver, S., Missault, S., Van Soom, J., Van Der Veken, P., Augustyns, K., Joossens, J., Dedeurwaerdere, S., & Giugliano, M. (2019). The effect of pharmacological inhibition of serine proteases on neuronal networks in vitro. *PeerJ*, *2019*(4), 1–23. https://doi.org/10.7717/peerj.6796